GROWTH AND CHARACTERIZATION OF GeSn AND SiGeSn ALLOYS FOR OPTICAL INTERCONNECTS

A DISSERTATION
SUBMITTED TO THE DEPARTMENT OF
MATERIALS SCIENCE AND ENGINEERING
AND THE COMMITTEE ON GRADUATE STUDIES
OF STANFORD UNIVERSITY
IN PARTIAL FULFILLMENT OF THE REQUIREMENTS
FOR THE DEGREE OF
DOCTOR OF PHILOSOPHY

Hai Lin

May 2012

I certify that I have read this dissertation and that, in my opinion, it is fully adequate in scope and quality as a dissertation for the degree of Doctor of Philosophy.

James Harris, Primary Adviser

I certify that I have read this dissertation and that, in my opinion, it is fully adequate in scope and quality as a dissertation for the degree of Doctor of Philosophy.

Paul McIntyre, Co-Adviser

I certify that I have read this dissertation and that, in my opinion, it is fully adequate in scope and quality as a dissertation for the degree of Doctor of Philosophy.

William Nix

I certify that I have read this dissertation and that, in my opinion, it is fully adequate in scope and quality as a dissertation for the degree of Doctor of Philosophy.

Krishna Saraswat

Approved for the Stanford University Committee on Graduate Studies.

Patricia J. Gumport, Vice Provost Graduate Education

This signature page was generated electronically upon submission of this dissertation in electronic format. An original signed hard copy of the signature page is on file in University Archives.

Abstract

Over the past few decades, the microelectronics industry has achieved previously unimagined success. Following Moore's law, the number of transistors in a chip has approximately doubled every 18 months and the size of a transistor has reduced down to 32nm. However, as the device size scales down, one of the major limitations in today's silicon integrated circuits comes from the electrical interconnects. In order to increase the interconnect density and decrease the interconnect energy, optical interconnects between chips or even on-chip have been proposed and widely investigated. The big challenge of integrating optics onto a Si chip is the compatibility, so group IV materials are considered. Optoelectronic devices for optical interconnects, such as modulators and detectors, have been demonstrated using both Si and Ge. A major issue now is the lack of a Si compatible light source. Because Si itself has very poor light emitting efficiency, current research focuses on Ge based semiconductors. There are two promising approaches to modify the band structure of Ge and make it a direct band gap material. This dissertation focuses on both of these approaches: applying biaxial tensile strain and alloying with Tin (Sn). In addition, combining these two methods is expected to achieve the goal with a more stable materials system. Therefore the ability to decouple these two effects and investigate the material properties independently is critical in our research.

$Ge_{1-x}Sn_x$ alloys were grown by molecular beam epitaxy (MBE) machines at low growth temperatures (150-200°C) on InGaAs buffer layers on GaAs substrates. $Ge_{1-x}Sn_x$ alloys with up to 10.5% Sn have been demonstrated with high crystal quality in this dissertation. Crystal quality of $Ge_{1-x}Sn_x$ layers was characterized by atomic force microscopy (AFM) and transmission electron microscopy (TEM). Composition and strain were studied by X-ray diffraction (XRD), secondary ion mass spectroscopy (SIMS) and X-ray photoelectron spectroscopy (XPS). The optical properties of $Ge_{1-x}Sn_x$ alloys were determined by photoreflectance (PR) and photoluminescence (PL).

The advantage of using InGaAs buffer layers is the separate control of the strain and composition effects on the material properties of $Ge_{1-x}Sn_x$ alloys. In this dissertation, $Ge_{1-x}Sn_x$ alloys with different Sn compositions and various levels of strain were grown. Room temperature PR measurements were used in this work to determine the direct bandgap from the maxima of the light- and heavy-hole bands to the bottom of Γ valley. The energy bowing parameter (b^{GeSn}) was calculated from the bandgap of unstrained $Ge_{1-x}Sn_x$ alloys to describe the composition effect. The indirect to direct band gap transition for unstrained $Ge_{1-x}Sn_x$ alloys was estimated to be around 6~7% Sn composition from low-temperature PL studies. The effect of biaxial strain on the direct band gap, described by two deformation potentials (a and b), was investigated for the first time as well. These basic parameters are very useful for the design of optoelectronic devices based on strained $Ge_{1-x}Sn_x$ alloys. Additionally, the strain and composition contributions to Raman shift of Ge-Ge LO peak in $Ge_{1-x}Sn_x$ alloys were quantified separately as well.

Moreover, $Ge_{1-x}Sn_x$/ $Si_xGe_{1-x-y}Sn_y$ quantum well (QW) structures are of great interest for photonic devices. Due to the large direct band gap of Si, $Si_xGe_{1-x-y}Sn_y$ alloys have larger bandgap energies than $Ge_{1-x}Sn_x$ alloys by design, so as barrier layers they can confine injected carriers inside the active $Ge_{1-x}Sn_x$ well. Good crystal quality of $Si_xGe_{1-x-y}Sn_y$ alloys were grown by MBE at low temperatures and annealed by RTA at 500°C in a forming gas ambient. The decoupling of the direct band gap and lattice constant of $Si_xGe_{1-x-y}Sn_y$ alloys were demonstrated. This feature simplifies the strain engineering in QW designs.

Finally, PL from $Si_xGe_{1-x-y}Sn_y$/$Ge_{1-x}Sn_x$/ $Si_xGe_{1-x-y}Sn_y$ double heterostructure was demonstrated experimentally for the first time. The measured PL peak energy matches the calculated value at room temperature, indicating that the basic materials properties determined in this dissertation are accurate. The observation of PL proves that these group IV alloys are promising candidates to make a Si-compatible laser for on chip optical interconnects.

Acknowledgements

I am very lucky to have had many great persons around me, encouraging, inspiring and supporting me all the time. My Ph.D work would not have been finished without their help. First and foremost, I would like to thank my advisor Professor James Harris, A.K.A. the Coach, for introducing me into this exciting area of optoelectronics. He not only gave me the guidance in research, but also conveyed an enthusiasm for science to me. I would also like to thank Professors William Nix, Krishna Saraswat and Paul McIntyre for taking time out of their busy schedules to attend my Ph.D oral exam and serve as my dissertation readers. Professor Walter Harrison was gracious enough to chair my oral.

I would like to thank my fellow MBE growers. It has been my pleasure to work with a group of brilliant people. Special thanks to Tomas Sarmiento, Angie Lin, Yijie Huo and Robert Chen for sharing with me all the details related to MBE growth and constant help to maintain the machines. Special thanks to Weisheng Lu for helping me set up the photoreflectance measurement. They are my dearest friends. I would like to thank other group members for their help in different areas and all the relaxing lunch gatherings. Special thanks are also due our administrative staff Gail Chun-Creech for her tireless work and dedication to keep the Harris Group running.

I would also like to thank staff in SNL for helping me run the experiments. Dr. Arturas Vailionis has helped me to do XRD measurements at SLAC. Dr. Chuck Hitzman has spent so much time to run SIMS measurements with me. Dr. Ann Marshalls has taught me how to run a complicated TEM system. I heartily appreciate their timely and generous helps In addition, I would like to thank Marika Gungim for help with the STEM and EDX and Linyou Cao for the Raman measurement.

I would like to thank all my friends for their companion and friendship. Finally, and certainly not least, I would like to thank Mom and Dad, and my boyfriend, for everything over the years.

Table of Contents

List of Tables

List of Figures

CHAPTER 1 Introduction

1.1 Motivation

Over the past few decades, the microelectronics industry has achieved truly great success. Electronic devices have become smaller and faster every year. Moore's law has been used as the benchmark for chip advancement in the microelectronics industry, which states that the number of transistors incorporated in a chip will approximately double every 18-24 months. In order to maintain this rate of advancement of high-speed electronics, the size of a transistor has decreased dramatically. New device structures and new dielectrics have been widely investigated. Intel has introduced the first 3-D transistor at 22nm for high-volume manufacturing. However, as the devices scale down, there are several issues related to fundamental materials and processing aspects that must be addressed. One important example is the limitation of operating speed of microelectronic devices due to electrical interconnect delay and power.

The scaling of electrical interconnections is limited by the physical properties of electrical wires. If a wire of length ℓ has a capacitance per unit length C_ℓ and a resistance per unit length R_ℓ, the total RC time constant of the wire is $R_\ell C_\ell \ell^2$. This RC time constant stays constant even the whole system shrinks.[1] The transistors on a chip in general get faster as the technology dimension shrinks, so the wires are not able to keep up with the transistors. Due to this delay, the density of information that can be sent is limited in order to have good signal to noise ratio. The ITRS roadmap shows that the RC delay is expected to become significant, especially for global interconnects (long ℓ). Another problem of electrical wires is power consumption. The electrical line has to be charged to at least the signaling voltage to transport signals. Currently the energy required for charging and discharging the lines can easily exceed that used for switching a logic gate. To overcome these limitations, copper wires and low-k dielectrics are used on chips to reduce resistance and capacitance, and improve

interconnect speed. Signaling on wires could also be significantly improved through the use of equalization techniques. One technique that is used routinely is to break the line into smaller segments and introduce repeater amplifiers. Unfortunately they consume significant power and require vias through multiple metal levels to connect from the signal lines down to the amplifier circuits and back. There are other possible physical approaches to improve electrical interconnects, including cooling the chips and three-dimensional structures with vertical connections. But the underlying scaling issues and other physical problems still remain.

There is another quite different approach to this challenge—changing the physical means of interconnection from electrical to optical interconnections.

1.1.1 Optical interconnects

Nowadays, optical interconnects via optical fibers and III-V laser sources have already taken over the task of long distance communications from electrical cables. Substantial recent efforts have focused on using optics at ever shorter distances and, board to board optical interconnects are now standard in large server banks. In order to move to an even much smaller dimension, considerable research is now being carried out on Si photonics to make on-chip optical interconnects available.

The differences in physics of optic and electronic lead to three specific major possible advantages for optical interconnects. [1-3]

(1) Interconnect density. The physics of loss and signal distortion for optical interconnections is completely different than electrical wires. There is essentially no distance-dependent optical loss or distortion over the scale of a machine with optical interconnects. Therefore it avoids the limit to the density of information that can be sent over relatively long distances, and it is particularly attractive for relatively long lines with high data rates and limited cross-sections.

(2) Interconnect energy. Optics may be able to save energy in interconnections because it is not necessary to charge the line to the operating voltage of the link. But it also requires energy to drive the optical devices. Professor Miller at Stanford University has calculated the energy requirement for optical interconnects to replace electrical interconnects.[3-4]

(3) Clock and signal timing.[5-6] Optics may be able to deliver and retain very precise timing in clocks and signals. Optical signals do not spread substantially in propagating over the size scale of an information processing machine. Optics could be useful for reducing the number of levels in the clock distribution tree, thereby reducing clock power dissipation and improving jitter.

Despite the advantages, implementing optical interconnects to electrical chips still faces many technical challenges. The requirements of dense optical interconnects at the chip level are substantially different than those of long-distance communications, such as much lower power dissipation, small latency, small physical size, vastly greater numbers and the ability to integrate with mainstream silicon electronic devices. There are several optoelectronic devices required for optical interconnects: laser, modulator, waveguide and detector. Nowadays, all the basic components for Si based optoelectronics have already been demonstrated,[7-10] except for a laser. So far, lasers on Si still rely on III-V materials, either grown on or bonded to Si. However, considering a high-volume application, neither of these approaches will be able to supply the necessary technology for on-chip single-wavelength or wavelength-division multiplexing laser sources. Epitaxial III-V lasers on Si still suffer limited lifetime and they involve elaborate growth of thick III-V buffer layers with serious contamination issues, while III-V wafer bonding on Si cannot be achieved at the wafer level for industrial applications

1.1.2 Si-compatible laser

Currently, the major bottle neck in the full integration of optoelectronics and microelectronics is the lack of a Si-compatible laser. The physical reason is the band structure difference between indirect and direct bandgap materials. Optical transitions must obey the laws of conservation of energy and momentum, but these conditions are not satisfied simultaneously in Si.[11-12]

As shown in Figure 1.1, in direct bandgap materials, such as GaAs and InP, radiative recombination occurs rapidly and efficiently via a simple two-particle process. Direct bandgap materials have a structure in which the lowest energy points of both the conduction and valence bands line up vertically in the wave vector axis; that is, they have the same crystal momentum. However, Si is an indirect bandgap material, so free electrons tend to reside in the X valley of the conduction band, which is not aligned with free holes in the valence band. Although phonons can provide the necessary momentum and help electrons radiatively recombine with holes, it is a second-order process. This three-particle interaction is very inefficient compared with the radiative transition in direct bandgap semiconductors. In the meantime, carries will recombine through non-radiative processes, like Auger recombination and free carrier absorption. These non-radiative processes have much shorter lifetime than those of radiative process in Si, resulting in an extremely poor internal quantum efficiency of light emission.

Therefore, another group IV element, germanium (Ge), is considered a far more attractive candidate. Although Ge is also an indirect bandgap material with the lowest band in the <111> direction of the Brillouin zone (L valley), it has a local minimum in the center (Γ valley), as shown in Figure 1.2. The energy difference between these two valleys is only 0.13eV. If electrons can overcome this small energy barrier and occupy the Γ valley, then the light emitting efficiency will be greatly increased, because the radiative recombination rate for direct band-to-band is five orders of magnitude higher than that of the indirect transition. This small energy difference also suggests the

possibility to make Ge a direct bandgap material through bandgap engineering. With a direct band structure, Ge can produce a Si compatible laser for on-chip optical interconnects.

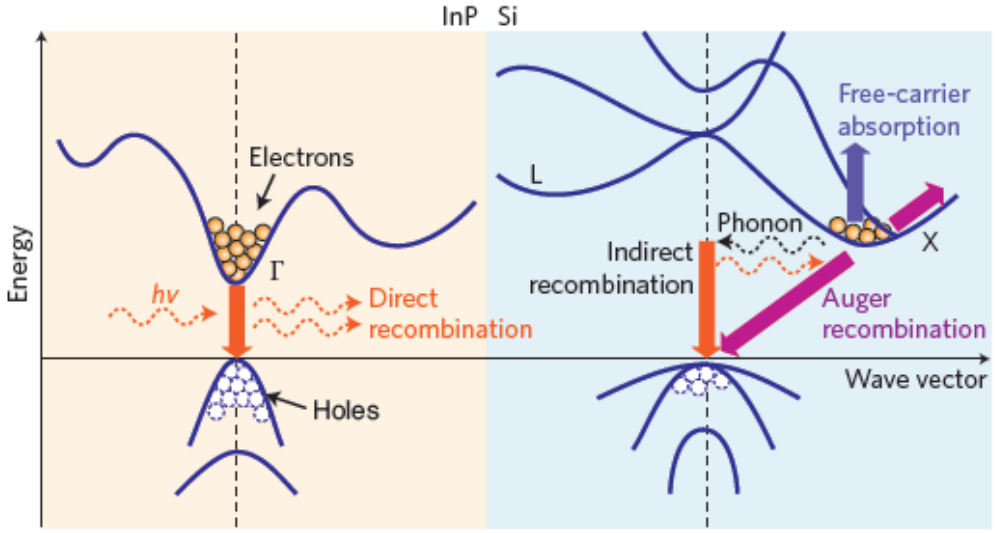

Figure 1.1 Schematic energy band diagrams and major carrier transition processes in InP (direct bandgap) and silicon (indirect bandgap) single crystal materials.

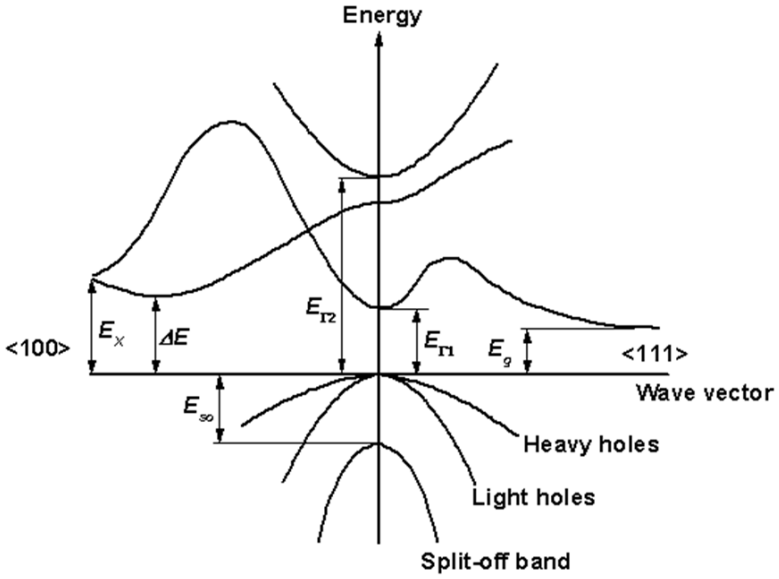

Figure 1.2 Energy band diagram of germanium (Ge).

1.2 Band structure engineering of Ge

The small energy difference of 0.13eV between the direct and indirect band gaps of Ge implies the possibility of either filling the indirect valley to a sufficient level that some electrons can occupy the direct band or by changing Ge into a direct band gap material where the electrons naturally occupy to lowest energy level. In general, there are three main approaches to produce sufficient electrons into the direct conduction band to achieve lasing, as illustrated in Figure 1.3:

i. Heavy n-type doping
ii. Biaxial tensile strain
iii. $Ge_{1-x}Sn_x$ alloys

These three mechanisms can be used separately or combined. We discuss each of these three mechanisms in this section.

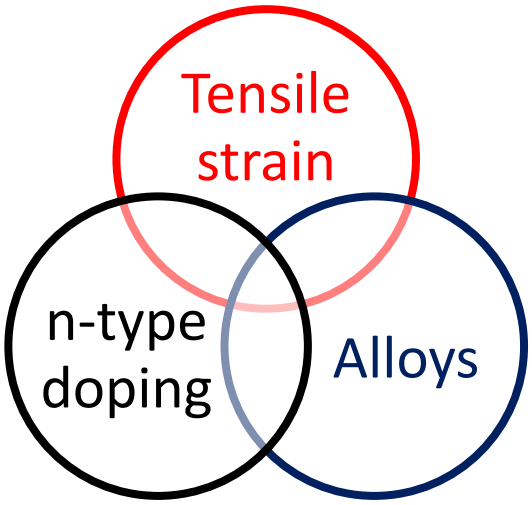

Figure 1.3 Three different mechanisms to improve the light emitting efficiency of Ge.

1.2.1 Heavy n-type doping

Heavy n-type doping preserves the original band structure and does not change Ge into a direct band gap material, but it can greatly increases the light emitting efficiency. As illustrated in Figure 1.4, with heavy n-type doping, the Fermi energy of Ge will be above the indirect conduction band (L valley) edge and there is then some probability that electrons occupy the direct band (Γ valley) due to Fermi-Dirac distribution. The higher the doping concentration, the greater the filling of the direct band. This band filling effect can thus enhance the light emitting efficiency of Ge by raising the possibility of direct transitions. El Kurdi et. al. demonstrated enhanced photoluminescence of heavily n-doped Ge by gas immersion laser doping process.[13]

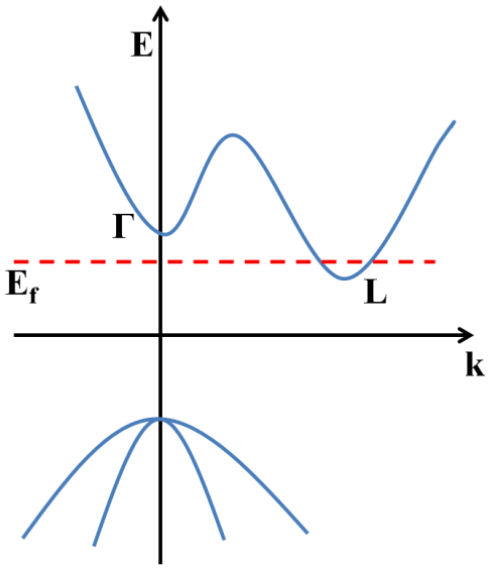

Figure 1.4 Schematic band diagram of Ge with heavy n-type doping

However, for unstrained Ge, a n-doping concentration of typically 10^{20} cm^{-3} is required to move the Fermi energy close to the direct band edge at room temperature. Such a high doping density is hard to achieve, so tensile strain has been included in most efforts to reduce the energy difference between L and Γ valleys, thus lower the required doping concentration. From calculations, the required doping concentration is

7.6×10^{19} cm^{-3} for Ge with 0.25% tensile strain to produce a sufficiently electron concentration for lasing in the direct band.[14] In-situ doped Ge layers were grown on Si with slight tensile-strain induced by thermal mismatch. Combining these two mechanisms, researchers at MIT and Stanford University demonstrated direct band gap photoluminescence (PL) and electroluminescence (EL) in Ge with an emitting wavelength around 1.6μm at room temperature.[15-17]

Because n-doping does not modify the band structure, the intensity of PL from the direct transition increases with temperature.[16, 18] Electron density in the Γ valley, which contributes to the light emission, is highly dependent on the Fermi-Dirac distribution. At lower temperatures, the Fermi-Dirac distribution resembles a step function and the probability that electrons occupy the Γ valley decreases. Conversely, at higher temperatures, the distribution smears out and more electrons are thermally excited from the lower energy indirect L valley to the higher energy direct Γ valley.

Cavity structures have been fabricated with n-doped Ge to make a laser. Disk structures were fabricated by Cheng et. al. at Stanford.[19-20] Liu et. al. at MIT made a waveguide structure by selectively growing Ge on Si with a SiO_2 mask. The Ge material was in situ doped to 1×10^{19} cm^{-3} with 0.24% thermally induced tensile strain. Optical gain from the direct gap transition was observed,[21] and eventually an optically pumped laser was demonstrated from this waveguide structure.[22] An electrically pumped Ge laser with heavy n-doping has recently been demonstrated, with the threshold current density of 290kA/cm^2 that is much higher than conventional III-V laers.[23] While this heavy doping approach did produce a laser, in theory the free-carrier absorption is proportional to $n^{3/2}$, which greatly increases the threshold for laser operation. Therefore, a laser of smaller threshold is expected to be with lower doping concentrations.

1.2.2 Biaxial tensile strain

Strain has significant effects on the band structure and optoelectronic properties of semiconductors. Different types of strain along different crystallographic directions will change the band structure in different ways. Biaxial tensile strain in (001) plane is of great interest in this work, because it is symmetric about the (111) minima in Ge and in theory it can change Ge into a direct band gap material. As illustrated in Figure 1.5, by applying biaxial tensile strain, both the direct and indirect band gaps shrink, but the direct gap shrinks faster than indirect band gap, so the difference between these two valleys decreases. Therefore, with a sufficient amount of strain, Ge will transform into a direct band gap material. Depending on the parameters used in the calculation, the transition tensile strain has been predicted to be from 1.6% to 1.9%.[24-25] In addition, biaxial tensile strain breaks the degeneracy of light hole (LH) and heavy hole (HH) valence bands, and lifts the LH band above the HH band.

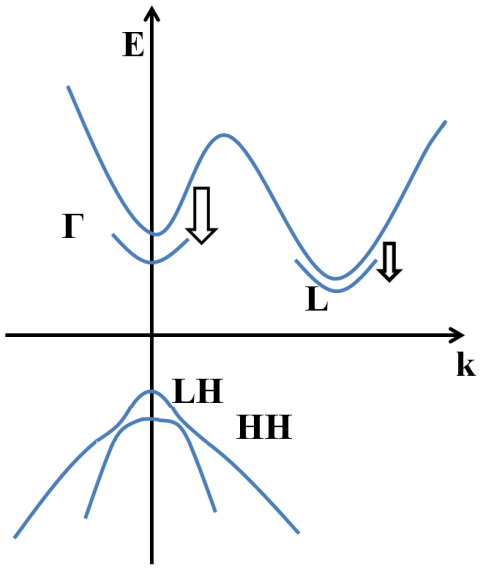

Figure 1.5 Schematic band structure of Ge with biaxial tensile strain.

It is important to understand the definition of biaxial strain. In this study, all the materials studied (Ge, GeSn, SiGeSn) have a cubic (diamond or zinc-blende) crystal structure. Biaxial tensile strain in (001) plane means that the lattice in the (001) plane

is stretched equally in both the [100] and [010] directions, and the in-plane lattice constant of the stained layer $a_{L||}$ is larger than the natural lattice constant a_L. Consistent with the Poisson's ratio, the lattice will shrink in the [001] direction, so the out-of-plane lattice constant $a_{L\perp}$ is smaller than a_L. Therefore we define the in-plane strain $\varepsilon_{||}$ and out-of-plane strain $\varepsilon_{\perp}$ of the strained layer as:

$$\varepsilon_{\parallel} = \frac{a_{L||} - a_L}{a_L} \quad \text{Eq.1-1}$$

$$\varepsilon_{\perp} = \frac{a_{L\perp} - a_L}{a_L} = -\frac{2C_{12}}{C_{11}}\varepsilon_{||} \quad \text{Eq.1-2}$$

where C_{11} and C_{12} are elastic stiffness constants of the strained layer. Biaxial compressive strain is defined in the same way, except that $a_{L||}<a_L$.

Biaxial tensile strain can be achieved by three different methods: (1) Thermal mismatch. This method relies on the fact that the linear thermal expansion coefficient for Si (2.6×10^{-6} °C^{-1}) is half of the coefficient for Ge (5.9×10^{-6} °C^{-1}). When a thick layer of Ge (>1μm) is grown on a Si substrate at high temperatures (>600 °C), the Ge layer is fully relaxed at the growth temperature. Upon cooling to room temperature, Ge layer shrinks faster than Si, so tensile strain is accumulated in the Ge layer. In general, the thermally induced tensile strain in Ge layer is around 0.2%. Additional strain can be added by light bending of the film toward the backside by depositing Ti, which enhances the strain by ~0.05%. Due to experimental limitations, the highest strain can be achieved using this method is around 0.25%, thus it is usually combined with heavy n-doping to improve occupancy of the direct energy band.[14, 16-17, 21, 26-27]

(2) Mechanical stress. External stress can be applied to designed Ge MEMS structures. 4 times larger strain can be achieved using this method, compared to the maximum strain using the first method, but it often creates non-uniform strain in the layer.[28-31] Band gap shrinkage and enhanced photoluminescence from the direct transition were demonstrated using pure external mechanical stress.[29-30]

(3) Lattice mismatch. Ge layer can be grown epitaxially on virtual substrates with lattice constants (a_s) larger than that of bulk Ge. The in-plane lattice constant of the Ge layer will be the same as a_s if its thickness is below the critical thickness, as demonstrated in Figure 1.6. Therefore the Ge layer is under biaxial tensile strain, and the strain level depends on the value of a_s. In order to control the strain, lattice controllable materials are used as virtual substrates. Up to 2.3% biaxial tensile strain has been achieved using InGaAs buffer layers on GaAs substrates,[32-34] and up to 0.71% strain using GeSn buffer layers on Si substrates.[35-38]

In comparison, only the third method can provide greater than 1.6% uniform strain to make Ge a direct band gap material. Unfortunately Ge with such a high degree of strain is relatively fragile. With increasing strain, the critical thickness for the Ge layer decreases dramatically. When the layer thickness is larger than the critical thickness, the epitaxial layer will relax through forming dislocations, which will greatly increase nonradiative recombination and reduce light emitting efficiency. Most likely, the Ge layer will be partially relaxed, so the value of in-plane lattice constant $a_{L||}$ is between a_s and a_L. The relaxation is defined as

$$R = \frac{a_{L||} - a_s}{a_L - a_s} \times 100\% \qquad \text{Eq.1-3}$$

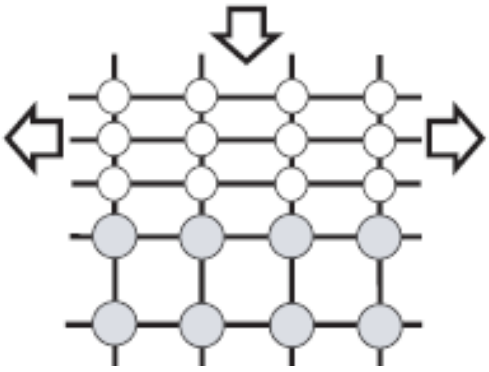

Figure 1.6 Schematic diagram of an epitaxial layer under biaxial tensile strain.

The theory for the critical thickness had been studied by Matthews and Blakslee[39] and other researchers.[40] But due to the different assumptions in dislocation type and

distribution, the critical thicknesses calculated by different models vary over a large range. For example, the lowest and highest predictions of critical thickness for 1% strain are 3nm and 30nm, respectively.[41] Therefore, rather than depending on theoretical calculations, we need to find a direct way to measure the strain and relaxation of epitaxial layers, such as Raman and X-ray diffraction. The measurements will be discussed in detail in Chapter 2.

1.2.2.1 Enhanced photoluminescence of tensile-strained Ge using InGaAs buffer layers

In our group, we demonstrated enhanced photoluminescence (PL) of tensile-strained Ge layers, with strain induced by designed composition InGaAs buffer layers.[34, 42-43]

Very thin layers of Ge (8-10nm) were grown on $In_xGa_{1-x}As$ buffer layers at 400°C by MBE. Different In compositions were chosen to provide different amounts of tensile strain to the Ge layer. The highest In composition is x=0.40 corresponding to 2.33% tensile strain for the Ge layer. The strain levels were determined by Raman spectroscopy and X-ray diffraction. Figure 1.7 shows cross-section TEM images of the 2.33% tensile-strained Ge on $In_{0.40}Ga_{0.60}As$. A thin layer of $In_{0.40}Ga_{0.60}As$ was grown on top to prevent Ge oxidation and eliminate associated surface states. Planar growth of the Ge layer is confirmed by the smooth interfaces between the buffer layers and the 10 nm Ge layer. The high resolution TEM image shows perfect atomic stacking of Ge, which further confirms good crystal quality of the strained Ge layer.[34]

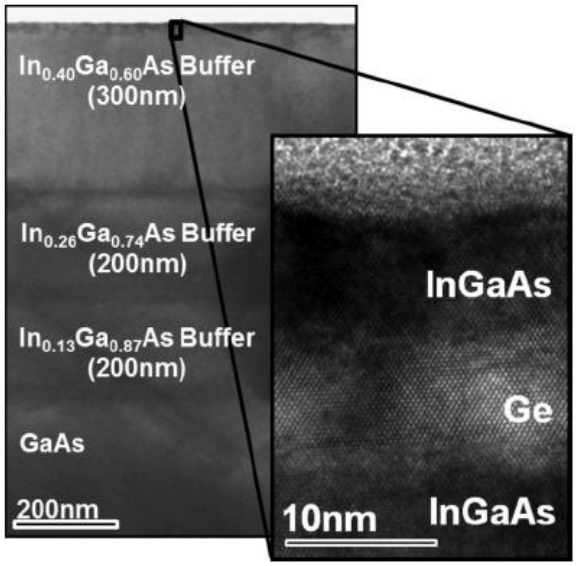

Figure 1.7 TEM images of 2.33% tensile-strained Ge on InGaAs buffer layers. The high-resolution image on the right shows fault-free stacking of Ge atoms.

Low-temperature PL measurements were performed using a standard lock-in amplifier setup to see if a strain-dependent PL peak could be observed. Figure 1.8 shows the normalized PL spectra at 5K from Ge on InGaAs buffer layers with different amounts of tensile strain of 0.34%, 0.92%, 1.81% and 2.33%. The spectra show a peak onset around 1500nm to 1550nm for samples with strain of 1.81% and 2.33%, and the peak intensity of the 2.33% strained sample is around 2.5 times greater than that of the 1.81% strained sample and hundreds times larger than 10nm unstrained Ge layer. The drop-off around 1600nm is due to limitations of the detector used in this PL setup. Compared with the PL spectra of samples with only InGaAs buffer layers, we conclude that the PL peaks are from the strained Ge layers, and tensile strain significantly enhances the PL intensity.[42]

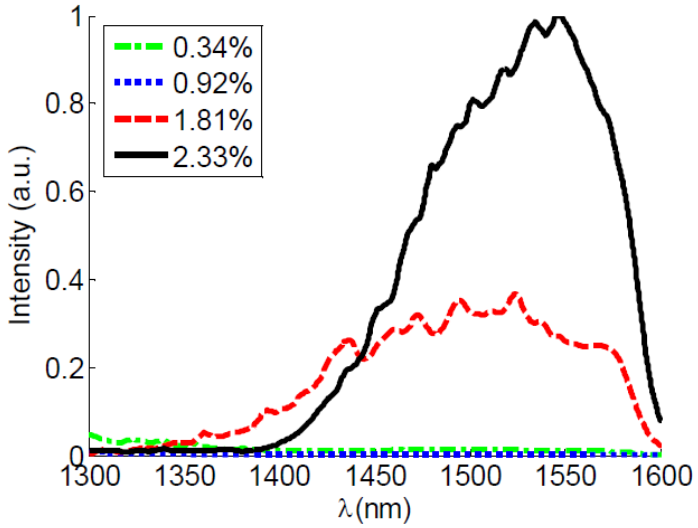

Figure 1.8 Normalized low-temperature PL for different biaxial tensile-strained Ge layers: 0.34% (green dash-dotted curve), 0.92% (blue dotted curve), 1.81% (red dashed curve), 2.33% (black curve).

1.2.3 $Ge_{1-x}Sn_x$ alloys

$Ge_{1-x}Sn_x$ alloys have attracted great interest in recent years due to their potential to become the first group IV direct band gap alloys. Diamond cubic Sn (or α-Sn) is a semimetal with a conduction band minimum at the Γ point sitting 0.41eV below the valence band. By alloying Sn and Ge, the conduction band extrema at both L and Γ valleys are predicted to decrease in energy with increasing Sn composition, but the Γ valley is predicted to decrease more rapidly than the L valley. Tight-binding[44] and pseudopotential[45] electronic structure calculations in virtual crystal approximation predict that $Ge_{1-x}Sn_x$ alloys would undergo an indirect to direct transition with a continuously tunable direct energy bandgap from 0.55eV to 0eV for Sn composition of x=0.2 to 0.6.

However, to obtain a high Sn composition in $Ge_{1-x}Sn_x$ alloys has been proven to be very challenging, due to the limited equilibrium solid solubility for both Sn in Ge and

Ge in Sn, less than 0.01. Figure 1.9 shows the equilibrium phase diagram. Sn will precipitate from $Ge_{1-x}Sn_x$ alloys in high compositions.[35, 37, 46] Also there is a tendency for Sn surface segregation during growth due to the lower surface free energy of Sn versus Ge.[47] These factors limit the thermal budget for crystal growth. Therefore a non-equilibrium growth technique, such as MBE, has to be employed to grow $Ge_{1-x}Sn_x$ alloys at low growth temperatures of $T \leq 200°C$.

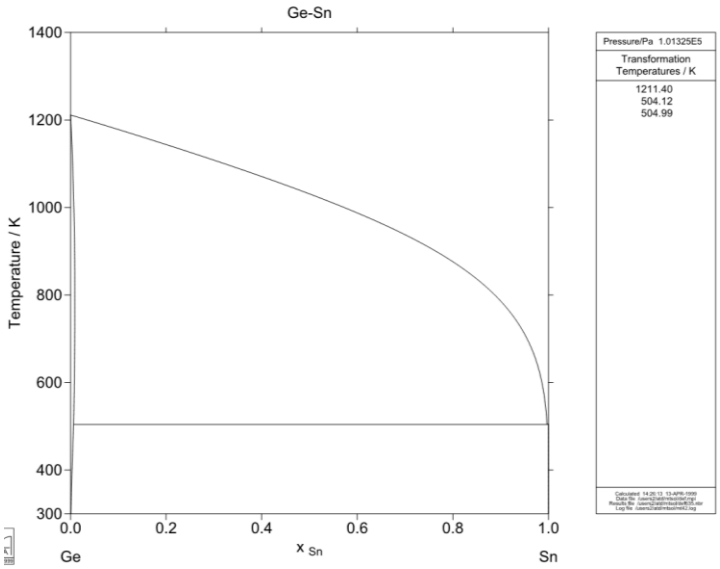

Figure 1.9 Binary phase diagram of Ge-Sn.

Due to the great difficulties associated with the growth, the actual measurement of energy bandgap in $Ge_{1-x}Sn_x$ alloys as a function of Sn composition was not published until 1997, in which the indirect to direct energy bandgap transition was estimated to occur near x=0.1[48] for relaxed $Ge_{1-x}Sn_x$ alloys on Si (001), much lower than the calculated prediction of x=0.2. Recently, the transition is predicted to happen at even lower Sn composition, around x=0.06.[49-51] The discrepancy between the band structure calculations and the experimental results has been attributed to the bowing of the bandgap produced by local distortions in the bond lengths and bond angles of the crystal. With the bowing effect, the composition dependent bandgap energy of alloys can be expressed as

$$E_g(Ge_{1-x}Sn_x) = xE_g(Sn) + (1-x)E_g(Ge) - bx(1-x) \quad \text{Eq.1-4}$$

where E_g(Ge) and E_g(Sn) represent bandgap energies of bulk Ge and Sn, and b is the bowing parameter. For the Γ valley, E_g(Ge)=0.8eV and E_g(Sn)= -0.41 eV. He et. al. had calculated b=2.8eV. The band bowing effect is illustrated in Figure 1.10. Recent results also confirmed the large band bowing effect and the bowing parameters were calculated to range from 1.8[50] to 2.4[52].

In the past decade, researchers have achieved great progress in growing $Ge_{1-x}Sn_x$ alloys. Researchers at Arizona State University have grown $Ge_{1-x}Sn_x$ alloys on Si substrate with up to x=0.2 by chemical vapor deposition (CVD) using a deuterium-stabilized Sn hydride source. Spectroscopic ellipsometry was used to explore the interband transitions.[49, 53-54] However, they only published results of photoluminescence and electroluminescence from samples with less than 3% Sn composition.[50, 55] Our group has demonstrated good crystal quality $Ge_{1-x}Sn_x$ layers with up to x=0.08 epitaxially grown by MBE. InGaAs buffer layers were used for strain control. We detected strong PL signals from all samples, and the PL peaks shift to lower energy range as a function of Sn composition as predicted. In addition, the intensity of PL peaks increases exponentially with increasing Sn composition. [56-57] $Ge_{1-x}Sn_x$ quantum dots have also been grown on Si (111) substrates covered with ultrathin SiO_2 films. Scanning tunneling spectroscopy was used to measure the increase of the $Ge_{1-x}Sn_x$ bandgap energy due to quantum confinement.[58-60]

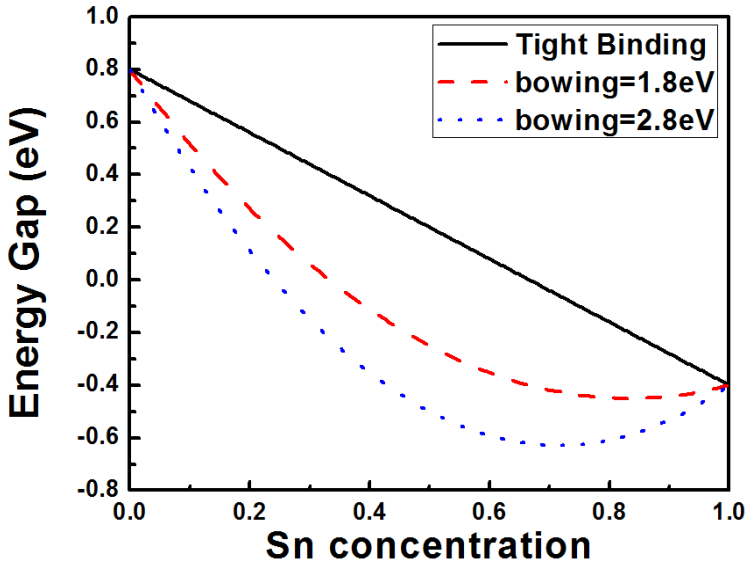

Figure 1.10 Direct bandgap energy variation with Sn composition: tight-binding calculation (solid black line), calculations with b=1.8eV (red dashed line) and b=2.8eV (blue dotted line).

Devices based on $Ge_{1-x}Sn_x$ alloys have been demonstrated. Light-emitting p-i-n diodes were grown on Si substrates with up to 2.2% Sn composition. Direct bandgap electroluminescence from these diodes was demonstrated at room temperature. The peak wavelength red shifts with respect to Ge as expected.[55, 61] $Ge_{1-x}Sn_x$ p-i-n photodetectors with up to x=0.03 grown on Si by MBE were fabricated as well. Compared to Ge photodetectors, the optical responsivity curve shifts to higher wavelengths and the responsivity increases.[62-64]

Besides optoelectronic devices, $Ge_{1-x}Sn_x$ alloys have many other applications as well. For example, they can be used as buffer layers for tensile-strained Ge. Researchers at Nagoya University have grown highly strain-relaxed $Ge_{1-x}Sn_x$ alloys on Ge and Si substrates using compositionally step-graded method. The highest Sn composition is 7.1% in their structures after anneal which can provide 0.71% tensile strain for Ge.[35-37, 46, 65] In addition, $Ge_{1-x}Sn_x$ can be used as a source/drain stressor material for advanced Ge pMOSFET technology.[66] A $Ge_{1-x}Sn_x$-channel pMOSFET has been demonstrated to have higher hole mobility than corresponding unstrained Ge-

channel devices.[67-68] Both p and n type doping in $Ge_{1-x}Sn_x$ alloys have been studied as well.[69-71]

1.2.4 $Si_xGe_{1-x-y}Sn_y$ alloys

In addition to $Ge_{1-x}Sn_x$ alloys, $Si_xGe_{1-x-y}Sn_y$ alloys are of great interest as well. Due to their greater chemical compatibility with Si substrates, $Si_xGe_{1-x-y}Sn_y$ alloys can act as compliant templates and buffer layers to control strain of subsequent grown layers on Si substrates. Another special feature of $Si_xGe_{1-x-y}Sn_y$ ternary alloys is independent lattice constant and band structure manipulation. In other words, $Si_xGe_{1-x-y}Sn_y$ alloys have tunable bandgap energy at a fixed lattice constant. D'Costa et. al. have grown $Si_xGe_{1-x-y}Sn_y$ alloys by CVD, and they fixed the ratio of Si:Sn at 4:1 so that the $Si_xGe_{1-x-y}Sn_y$ alloys were lattice-matched to Ge. Using variable-angle spectroscopic ellipsometer, they observed an increased direct bandgap with increasing Si composition. Other optical transitions were studied in the same way.[72-75]

Based on these benefits, $Si_xGe_{1-x-y}Sn_y$ alloys are chosen to be the barrier layer for Ge and $Ge_{1-x}Sn_x$ quantum wells to make pure group IV lasers. By cleverly choosing the composition, the $Si_xGe_{1-x-y}Sn_y$ barrier layer has a desired lattice constant to strain or match the following Ge or $Ge_{1-x}Sn_x$ quantum well layer, while keeping larger bandgap energy to confine carriers inside the active Ge or $Ge_{1-x}Sn_x$ layer. For example, Chang et al. proposed a tensile-strained Ge quantum well laser based on a heavily n-doped $Ge/Si_{0.2}Ge_{0.7}Sn_{0.1}$ MQW structure.[76] Strain-free $Ge_{0.94}Sn_{0.06}/Si_{0.15}Ge_{0.75}Sn_{0.1}$ double heterostructures[77] and strain-balanced $Ge_{0.84}Sn_{0.16}/Si_{0.09}Ge_{0.8}Sn_{0.11}$ MQW lasers[78] were proposed and simulated for optical gain as well. Type-I band offset alignment was assumed in the simulations. The simulations show very promising results, but due to limited experimental results, the material properties, such as bandgap energy and effective mass, used in the calculation are mostly based on theoretical prediction, which are subject to correction.

1.3 Outline of dissertation

The goal of this dissertation is to provide a foundation of materials technologies to enable realization of a Si-compatible laser for optical interconnects. The fundamentals of $Ge_{1-x}Sn_x$ semiconductor alloys have been explained in this introductory chapter. This dissertation focuses on band structure engineering of Ge using $Ge_{1-x}Sn_x$ and strain. Knowledge of the bandgap energy of $Ge_{1-x}Sn_x$ alloys with different amounts of strain is very useful for the design of future optoelectronic devices based on these alloys. $Si_xGe_{1-x-y}Sn_y$ alloys are also investigated, to form $Ge_{1-x}Sn_x$/ $Si_xGe_{1-x-y}Sn_y$ heterostructures.

This remainder of dissertation is divided into five chapters. In Chapter 2, the basics of the MBE growth process and characterization methods are discussed. Chapter 3 describes the growth and characterization of $Ge_{1-x}Sn_x$ alloys. Special attention is paid to the materials properties determined by decoupling Sn composition and strain effects. Chapter 4 describes the growth and characterization of $Si_xGe_{1-x-y}Sn_y$ alloys and demonstrates the decoupling of bandgap and lattice constant. Chapter 5 shows photoluminescence from the $Ge_{1-x}Sn_x$/ $Si_xGe_{1-x-y}Sn_y$ heterostructure, which validate the aforementioned growth technique and the determined material properties. Chapter 6 ties these topics together with suggestions for future work.

CHAPTER 2 MBE Growth and Characterization

2.1 Introduction to Molecular beam epitaxy

Molecular beam epitaxy (MBE) is a technique for epitaxial growth of high-purity materials under ultra-high vacuum (10^{-10} torr) at a relatively slow growth rate. MBE can produce high-quality layers with very abrupt interfaces and good control of thickness, doping, and composition. It is a valuable tool in the development of sophisticated electronic and optoelectronic devices.

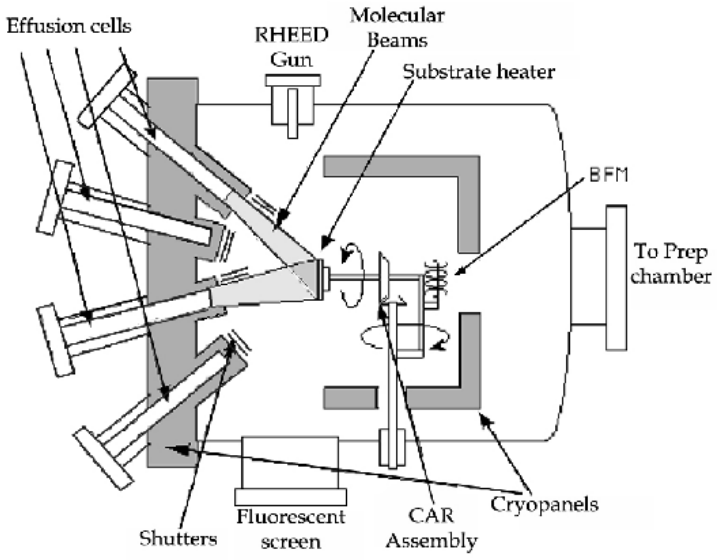

Figure 2.1 Schematic diagram of a typical MBE growth chamber.

Figure 2.1 shows a schematic diagram a typical MBE growth chamber. Ultra-high vacuum is essential to MBE systems; therefore in addition to vacuum pumps (turbo pump or cryo pump), a liquid nitrogen cooled cryoshroud is located between the chamber walls and the substrate heater and acts as an effective pump for residual gasses in the chamber that have not hit the substrate. High purity source materials are loaded into effusion cells, which are pointed toward the substrate heater. Effusion cells

are independently heated to evaporate the source materials, and due to the long mean free path of particles under high vacuum, the fluxes of source material in the form of "molecular beams" are deposited on the substrate directly without scattering or any chemical reaction before reaching the substrate surface. Computer controlled shutters are positioned in front of each effusion cell to shutter the flux reaching the sample within a fraction of a second, thus enabling precise control the growth thickness. A chilled panel separates the effusion cells to prevent thermal crosstalk between different sources. Samples are mounted on a substrate block which is then loaded onto the substrate heater that rotates on two axes—one for loading wafers and the second for growth uniformity. Before growth, the ion gauge on the opposite side of the heater is facing the sources to measure beam equivalent pressure (BEP), which is used to determine the growth rate. Then, the heater is flipped to face the sources, and rotates to obtain good uniformity during growth by continual azimuthal rotation (CAR). Reflection high-energy electron diffraction (RHEED) is usually used in MBE to in-situ monitor the growth. It can be used to calibrate growth rates, observe removal of oxides from the surface, calibrate the substrate temperature, monitor the arrangement of surface atoms, determine the proper arsenic overpressure, and provide feedback in real-time on surface morphology and growth kinetics.

In this work, Varian Gen II MBE systems were used. In addition to the growth chamber discussed above, there are two more vacuum chambers: a transfer tube, and a loading chamber. The loading chamber is used to bring samples in and out of the vacuum environment while maintaining the vacuum integrity of the other chambers. The transfer tube connects two different growth chambers under high vacuum (10^{-9} torr). One of the growth chambers is used to grow group IV materials, and the second one is used for III-V semiconductors. The base pressures for both growth chambers are under 3×10^{-10} torr.

2.1.1 Growth rate calibration

Growth rate calibration is essential for proper tuning of the composition of semiconductor alloys. One way to measure the growth rate is to use the BEP gauge that is on the backside of the substrate holder in the MBE system. The effusion cells used in MBE systems exploit the evaporation process of condensed materials and equilibrium can be established between the gas and condensed phases. The pressure P_{eq} (measured by the BEP gauge) is an exponential function of the cell temperature T. For a given system and material, the BEP reading is proportional to the flux at the sample surface and hence the growth rate. It is not a direct measure of the growth rate, so some other ex-situ technique must still be used to relate the BEP or cell temperature to a growth rate. For example, cross-section SEM images are used to measure the thicknesses of epitaxial layers grown at different cell temperatures, and for each temperature the growth rate is determined by the measured layer thickness divided by the growth time.[79] After calibration, we can control the growth rate of each element by changing the effusion cell temperature. Also MBE growth is a non-equilibrium physical process, so the substrate temperature does not generally affect the growth rate as much as in MOCVD, especially in low temperature range. Thus the calibrated growth rates in MBE are valid over a wide range of substrate temperatures.

The composition of alloys or compound semiconductors can be controlled by the growth rate of each component in the materials. For example, the composition of $Ge_{1-x}Sn_x$ alloys can be expressed as

$$x = \frac{Gr(Sn)/a(Sn)^3}{Gr(Ge)/a(Ge)^3 + Gr(Sn)/a(Sn)^3} \qquad \text{Eq.2-1}$$

where Gr(Sn) and Gr(Ge) are the growth rates, and a(Sn) and a(Ge) are the lattice constants for Sn and Ge. This equation is an approximation, but it gives us a guide to tune each cell's temperature for samples of different composition. With careful calibration, the error of the composition is less than 0.5%. This is very important from an experimental perspective. But to obtain exact composition of the epitaxial layer, ex-

situ measurements, such as XRD or XPS, must be performed afterwards. The details in composition determination will be discussed in section 2.3.

2.1.2 RHEED

RHEED is a very useful tool for in-situ monitoring of the growth. The RHEED gun emits ~10KeV electrons which strike the surface at a shallow angle, making it a sensitive probe of the surface. Electrons reflect from the surface and strike a phosphor screen forming a pattern consisting of a specular reflection and a diffraction pattern. The appearance of the RHEED diffraction pattern can be used to provide qualitative feedback on surface morphology.[80] If the crystal surface is smooth, then the RHEED diffraction patterns appear streaky. The pattern usually depends on crystal direction. For example, due to two different As surface reconstructions, the RHEED diffraction from GaAs (001) substrate is different along the [011] and [01$\bar{1}$] directions, or (2×4) pattern. If the surface is rough, then the horizontal streaks are more 'spotty' and the diffraction pattern is not as clear, as shown in Figure 2.2 (a).

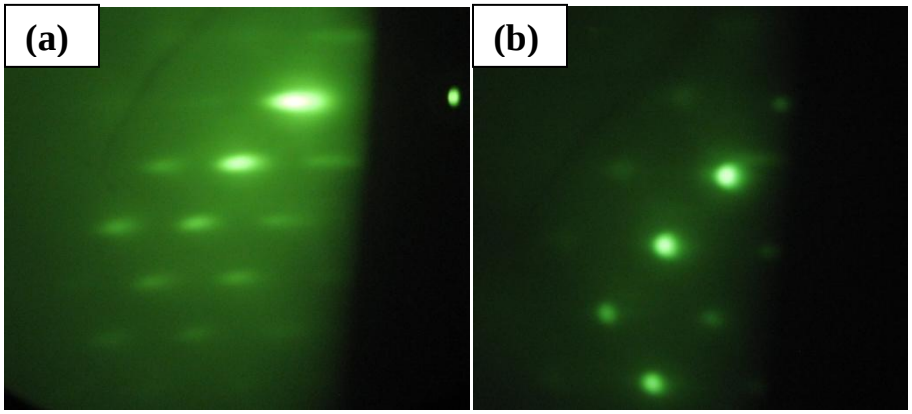

Figure 2.2 (a) RHEED pattern of a rough surface of strained $Ge_{1-x}Sn_x$ alloy. (b) RHEED pattern of Ge quantum dots.

If the growth mode changes to three-dimensional (SK) growth mode, quantum dots (QD) form on the surface. Many electrons will be transmitted through surface

asperities and scattered in different directions, resulting in a RHEED pattern constituted by many spotty features. Figure 2.2 (b) shows the RHEED pattern taken during the growth of Ge QD. If the surface consists of amorphous materials, such as an oxide layer, RHEED shows a haze background without any pattern. This is important for evaluating oxide desorption when a new substrate is initially heated up prior to growth in the MBE chamber. The transition from haze to clear diffraction pattern indicates the exposure of the underlying crystalline semiconductor surface.

2.2 Experimental details

2.2.1 Structure growth

All samples in this work were grown on GaAs (100) substrates by MBE. The wafers were first baked in the loading chamber at 350°C for an hour to remove the water vapor. After the wafers were transferred into MBE growth chamber, the substrate heater ramped up to 680 ℃ to thermally remove the native oxide. The transition from haze to clear RHEED pattern was observed in this process. Then a 100nm GaAs buffer layer was grown to cover the defects due to oxide desorption and a clear (2×4) RHEED pattern was observed.

First of all, step-graded InGaAs buffer layers were grown to control the strain of the following $Ge_{1-x}Sn_x$ or $Si_xGe_{1-x-y}Sn_y$ layers. Up to three sequential InGaAs buffer layers were used to achieve the required In composition at the top layer. The nominal In content was increased by about 10-15% in each successive layer by varying the In:(In+Ga) growth rate ratio. Each buffer layer was grown at 380 ℃ with a 20 minutes in-situ annealing at 540 ℃ after growth, and then an InGaAs cap layer with the same In content as the last buffer layer was grown at 380 ℃ without annealing. Each buffer layer was 200nm or 250nm thick.

The samples were then transferred through the transfer tube under high vacuum to the connected group IV chamber. High purity (>99.999%) solid sources of Si, Ge and Sn were used with Kundsen diffusion cell for elements evaporation. $Ge_{1-x}Sn_x$ and $Si_xGe_{1-x-y}Sn_y$ layers were grown at substrate temperatures of 150-200 ℃ thermocouple reading at a growth rate of 1nm per minute. The growth temperature was lower for samples with higher Sn compositions. The thickness varied from 20nm to 100nm. RHEED was used prior to the growth to verify the surface quality of the buffer layers. RHEED was also used during the $Ge_{1-x}Sn_x$ and $Si_xGe_{1-x-y}Sn_y$ growth to monitor the surface roughness.

2.2.2 Structure design—decouple strain and composition

The main reason to grow $Ge_{1-x}Sn_x$ and $Si_xGe_{1-x-y}Sn_y$ layers on InGaAs buffer layers, instead of Si substrates, is to decouple strain and composition. By this way, it provides the freedom to design the structure to study the material properties in terms of these two effects separately.

Otherwise, if a $Ge_{1-x}Sn_x$ layer is grown directly on a Si substrate, then the lattice mismatch will be larger than 4%, so the $Ge_{1-x}Sn_x$ layer can easily relax with dislocations. The relaxation depends on the thickness of the $Ge_{1-x}Sn_x$ layer and the Sn composition in the layer. The higher the Sn composition or the thicker the layer, the more the layer relaxes. In this case, there is no control of strain, and strain is coupled with Sn composition.

This problem can be solved by using InGaAs buffer layers. The buffer layers are designed to be relaxed, and the relaxation is around 85% using the growth recipe described above. Therefore the lattice constant depends mainly on In composition. In this case, with $Ge_{1-x}Sn_x$ layer coherently growing on top, the in-plane lattice constant of the $Ge_{1-x}Sn_x$ layer also depends on In composition in the buffer layer, but not Sn composition. Using this method, different amount of strain can be applied to the $Ge_{1-x}Sn_x$ layer with different Sn compositions. As shown in Table 2.1, for a given

composition x=0.06, we can design the type and amount of strain we want to apply to the $Ge_{0.94}Sn_{0.06}$ layer using different In compositions.

Table 2.1 The strain calculations of a $Ge_{0.94}Sn_{0.06}$ layer on InGaAs buffer layers with different In compositions.

In %	**In-plane lattice constant (buffer and $Ge_{1-x}Sn_x$ layers)**	**Lattice constant of relaxed $Ge_{1-x}Sn_x$ layer**	**Strain of $Ge_{1-x}Sn_x$ layer**
11%	5.681 Å	5.707 Å	-0.39%
17.5%	5.707 Å	5.707 Å	0%
22%	5.725 Å	5.707 Å	0.32%

Of course, using III-V materials is not our final goal. Eventually the whole materials system must be transferred to Si substrates for a fully integrated photonic interconnects.

2.3 Characterization methods

After growth, the samples were characterized by various methods. Atomic force microscopy (AFM), X-ray diffraction reciprocal space mapping (XRD-RSM), transmission electron microscopy (TEM) and Raman spectroscopy were used to study the structural properties. XRD, X-ray photoelectron spectroscopy (XPS) and secondary ion mass spectroscopy (SIMS) were used to determine the composition. Photoreflectance spectroscopy (PR) and photoluminescence spectroscopy (PL) were used to study the optical properties. These characterization techniques will be discussed in detail in subsequent subsections.

2.3.1 Atomic force microscopy

Atomic force microscopy (AFM) is a very high-resolution type of scanning probe microscopy for surfaces, with demonstrated resolution on the order of fractions of a nanometer. It consists of a probe in the shape of a cantilever with a sharp tip at its end, a laser, a four-quadrant photodiode, and a scanner unit constructed from piezoelectric elements. The laser beam is focused onto the back of the free end of the cantilever and reflected to the four-quadrant photodiode. The bending of the cantilever is detected with high precision.[81]

A Park system XE-70 AFM with Nanosensors PPP-NCHR tips was used in this work, and non-contact mode was used to characterize the sample morphology. In non-contact mode, the cantilever is mechanically oscillated at or close to its resonance frequency at a small distance from the surface. While scanning the tip across a sample surface, the tip-sample interaction changes the vibration amplitude or frequency, which serves as a feedback to adjusting the average tip-to-sample distance.[81] Measuring the tip-to-sample distance at each data point allows the scanning software to construct a topographic image of the sample surface.

Figure 2.3 shows a $20\times20\mu m^2$ AFM image of a $Si_xGe_{1-x-y}Sn_y$ sample on InGaAs buffer layers. This AFM image represents the typical morphology of all samples. The cross hatch pattern is inherited from the relaxed InGaAs buffer layers. The color bar on left represents the height of features on the surface, and the smoothness of the surface is described by the RMS roughness.

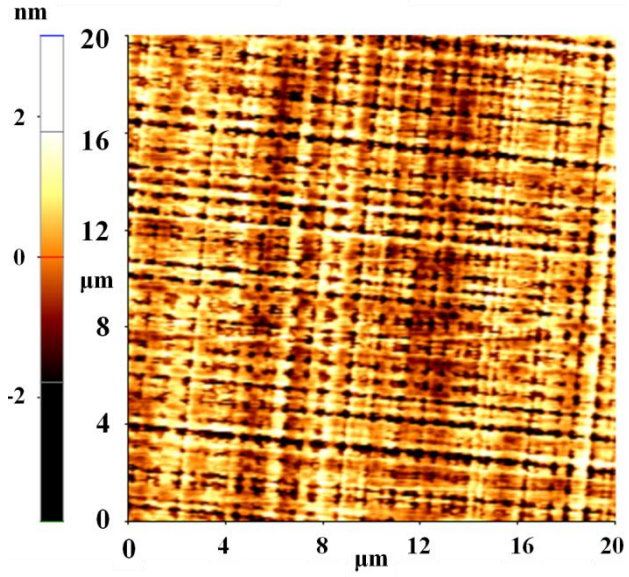

Figure 2.3 20×20µm^2 AFM image of a $Si_xGe_{1-x-y}Sn_y$ sample on InGaAs buffer layers grown at 150°C with RMS roughness of 0.9nm.

2.3.2 Transmission electron microscopy

Transmission electron microscopy (TEM) is a microscopy technique whereby a beam of high energy electrons is transmitted through an ultra thin specimen, interacting with the specimen as it passes through. An image is formed from the interaction of the electrons transmitted through the specimen; the image is magnified and focused onto an imaging device. The de Broglie wavelength of the high energy electrons is in the picometer range, so the TEM is capable of imaging at a significantly higher resolution than light microscopes. In addition to its imaging capability, TEM can generate diffraction patterns and perform elemental analysis as well. In this work, a Philips CM20 FEG-TEM operating at 200 kV was used.

2.3.2.1 TEM operations

The simplified representation of the ray path in TEM is illustrated in Figure 2.4. Electrons coming from the condenser system of the TEM, are scattered by the sample,

which is in the object plane of the objective lens. Electrons scattered in the same direction are focused in the back focal plane, where the diffraction pattern is formed. Electrons coming from the same point of the object are focused in the image plane to form the image. More lenses afterwards are used for magnification. [82]

In the image mode, the image plane is projected onto the viewing screen. Mass-thickness and diffraction contribute to image contrast. Mass-thickness contrast arises from incoherent elastic scattering of electrons. High-mass regions of a specimen tend to scatter more electrons than low-mass regions of the same thickness, so it appears darker in the image formed by transmitted electrons. Similarly thickness of the specimen will add contrast to the image. In addition, diffraction contrast is introduced by selecting specific electrons or excluding them using an aperture in the back focal plane. For example, in the bright field (BF) mode, an aperture blocks the diffracted beams and allows only the direct transmitted beam to pass. Defects in crystalline materials will diffract the direct beam to other direction, so they will be darker in a BF image than non-dislocated regions. Therefore, TEM is a very good tool to study defects and crystalline quality.

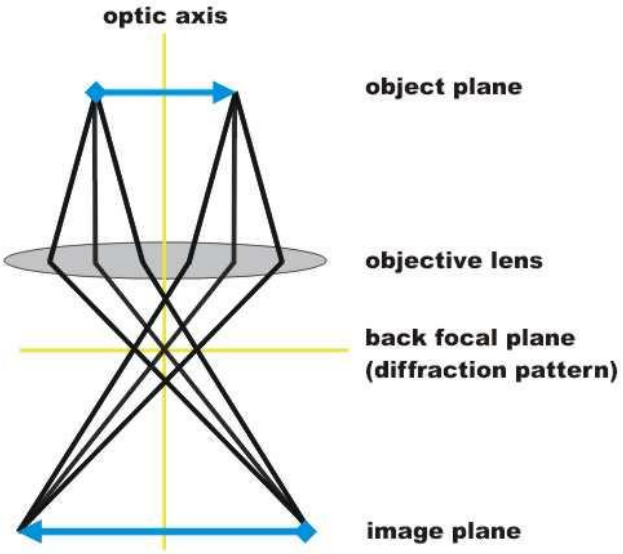

Figure 2.4 A simplified representation of the ray path in TEM.

High-resolution TEM (HRTEM) is used to obtain lattice images. The image is formed by the interference of the diffracted beams with the direct beam (phase contrast). To get higher resolution, a large objective aperture has to be selected that allows many beams including the direct beam to pass. Columns of atoms can be seen from a crystalline sample oriented along a zone axis. HRTEM is very useful to study the atomic structure of materials.

In diffraction mode, the back focal plane of the objective lens is projected onto the viewing screen. The diffraction pattern contains information of the crystallographic characteristics, phase, and sample orientation.

TEMs are almost exclusively equipped with energy-dispersive spectrometers (energy-dispersive X-ray spectroscopy EDXS). When the electron beam strikes a TEM sample, it also generates characteristic X-rays. Each element has characteristic peak positions corresponding to the possible transitions in its electron shell. The positions and intensities of X-ray peaks are used for qualitative and quantitative element analysis.

2.3.2.2 TEM sample preparation

TEM samples in this work were prepared mechanically. To prepare specimens for cross-section images, we first glued two pieces of samples face to face with epoxy and then polished it from both sides until the thickness is around 30μm. Then the thin piece was stuck to a copper grid and further ion milled with a Gatan PIPS system until a hole appeared in the middle. Therefore, thin areas on sample surface were obtained that can be viewed in TEM.

2.3.3 X-ray diffraction and reciprocal space mapping

X-ray diffraction (XRD) is a nondestructive technique that reveals detailed information about the crystallographic structure and chemical composition of epitaxial

layers. A PANalytical X'Pert PRO system was used in this work. The incident X-ray beam passes through a hybrid monochromator to form a quasi-parallel beam with Cu Kα1 radiation (1.54056 Å). The diffracted beam is collected with an analyzer crystal placed before the detector, which narrows the acceptance angle to 12 arc sec. With such a high resolution, XRD reciprocal space mapping (XRD-RSM) can be measured.

2.3.3.1 XRD scan geometry

Symmetric and asymmetric scan geometries are plotted in Figure 2.5. The angle between the incident X-ray and the sample surface is defined as ω and the angle between the scattered and incident X-ray is defined as 2θ. 2D RSM is achieved by varying the values of ω and 2θ.

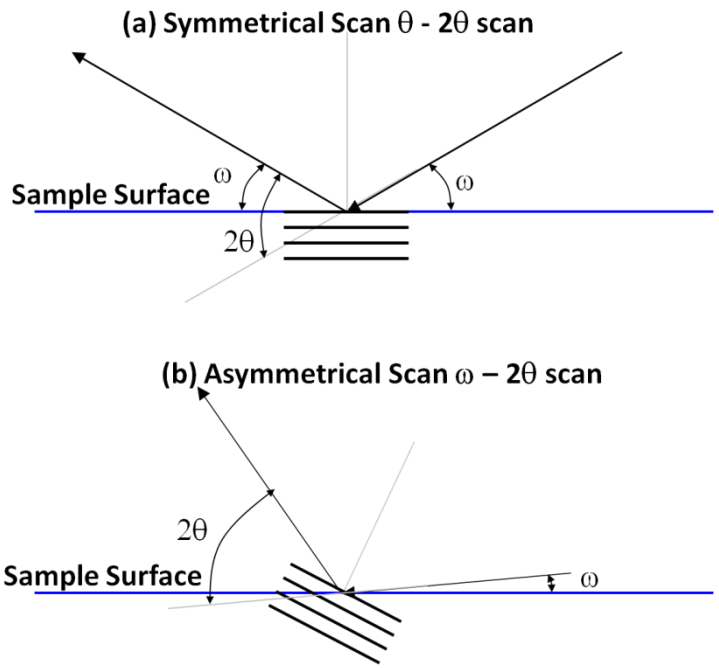

Figure 2.5 XRD scan geometries for (a) symmetrical scan and (b) asymmetrical scan.

2.3.3.2 Determination of lattice constant and strain

In this work, XRD-RSMs around symmetric (004) and asymmetric (224) diffraction points were measured. Combining these two scans, the in-plane and out-of-plane lattice constants of the epitaxial layers can be determined.[83-84] Strain can be calculated using Eq.1-1 and Eq.1-2. As illustrated in Figure 2.6, the red spots represent the diffraction peaks from the substrate, and the blue solid shapes represent epitaxial layer peaks. Out-of-plane lattice constant $a_{\perp}$ can be calculated from the symmetric (004) RSM scan. The position difference of the substrate and the layer peak in the (004) RSM scan indicates a difference in $a_{\perp}$. (224) RSM scan is asymmetric with respect to the surface, which allows for the in-plane ($a_{||}$) and out-of-plane lattice constants to be determined independently and simultaneously. If the layer peak aligns vertically with the substrate peak, the layer has the same $a_{||}$ as the substrate, or it is fully strained. If the layer peak is in the line connecting (000) and (224) diffraction spots, the layer is fully relaxed and has its bulk lattice constant. If the layer peak lies in between, it is partially relaxed. However, when the layer is tilted with respect to the substrate, this tilting effect will affect the layer positions in both (004) and (224) RSM scans. The black circles represent one fully relaxed layer peak with a tilt of α degrees with respect to the surface normal. If only the (224) RSM scan is taken, due to the tilting effect, this layer looks like it is partially relaxed, even though it is fully relaxed. Therefore, both symmetric and asymmetric scans have to be measured to remove the tilting effect and to draw the right conclusions about strain.[83]

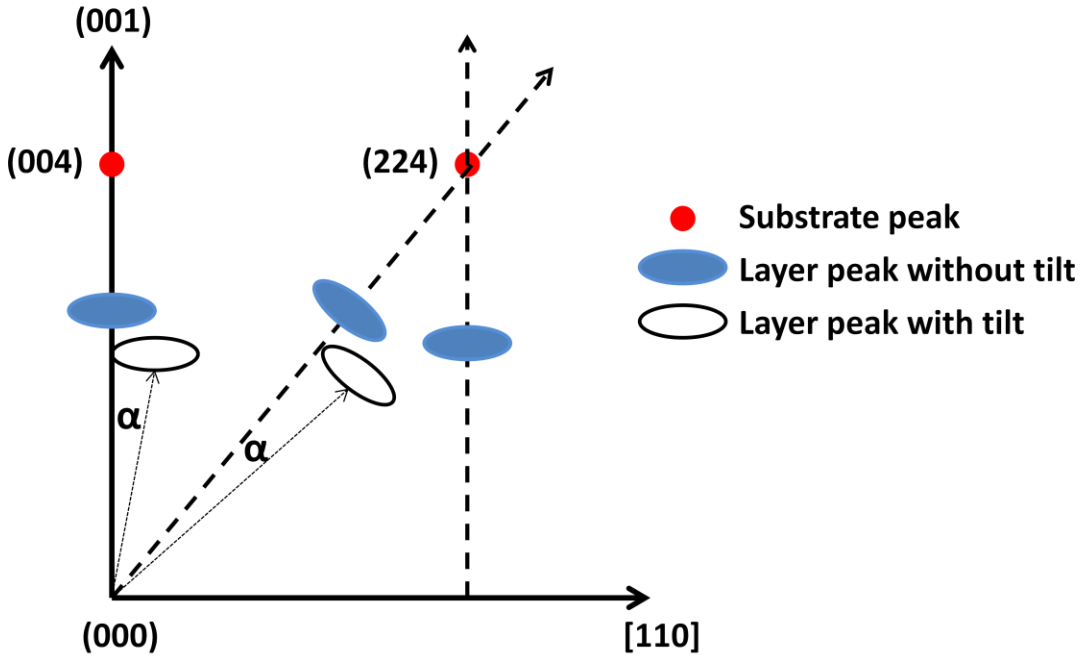

Figure 2.6 Illustration of XRD-RSM scans around symmetric (004) and asymmetric (224) diffraction points. Substrate and layer peaks under different scenarios are shown.

2.3.3.3 Determination of composition

As described above, in-plane and out-of-plane lattice constants of the layer can be determined from (004) and (224) XRD-RSM scans. Composition of binary alloys can be calculated from the lattice constants with the following two equations.

(1) The relationship between unstrained lattice constant and composition can be expressed as[85]

$$a(A_xB_{1-x}) = xa_A + (1-x)a_B + b_{AB}a_Aa_B \qquad \text{Eq.2-2}$$

where a is the unstrained lattice constant for different materials and b_{AB} is the parameter accounting for possible deviation from linear interpolation of lattice constants of two elements. For certain materials, this deviation is small enough to be neglected, i.e, $b_{SiGe} = -0.0021\text{Å}$, then Vegard's Law

or linear interpolation is valid. We assume that Vegard's Law is valid for $Ge_{1-x}Sn_x$ alloys as well in this study.

(2) The relationship between the elastic constant C_{11}, C_{12} and composition. In this work, linear interpolation is used.

$$C(A_xB_{1-x}) = xC_A + (1-x)C_B \qquad \text{Eq.2-3}$$

Combing these equations, we can run an iterative simulation to obtain the composition. With a starting composition, the unstrained lattice constant is calculated using Eq.2-2. Then strains for in-plane ($\varepsilon_{\perp}$) and out-of-plane ($\varepsilon_{||}$) are calculated using Eq.1-1and Eq.1-2 based on the calculated unstrained lattice constant and measured in-plane and out-of-plane lattice constants. From Eq.1-2, C_{12}/C_{11} can be obtained from $\varepsilon_{\perp}/\varepsilon_{||}$. If the ratio of elastic constants calculated from strain does not equal to the ratio calculated based on composition (Eq.2-3), the composition of binary alloys will be adjusted until these two results converge. However, this method can't be used for ternary alloys, because there are two degrees of freedom to adjust the lattice constant by composition. Therefore, other techniques must be explored, such as SIMS and XPS, which do not rely on lattice constant.

2.3.3.4 Determination of epitaxial layer quality

The crystallographic parameters, such as strain and tilt, are macroscopic ones that alter the position of the layer peak in reciprocal space. In contrast, mosaic structure and coherence length are microscopic properties that alter the shape of the layer peak.[86] Mosaic structure is an indication of the presence of misfit dislocations, which slightly rotate the allowable diffraction planes in their vicinity, as shown in Figure 2.7(a). It broadens the layer peak in reciprocal space along the mosaic direction (perpendicular to the scattering vector), as shown in Figure 2.8. On the other hand, the broadening horizontally (along q_x direction) is due to a limited lateral correlation length, which can be related to an average crystallite size that exhibits coherent diffraction, or in other words, the separation between crystalline defects as shown in Figure 2.7(b). For example, a high density of threading dislocations that break the

coherence within a single crystal layer reduces the lateral correlation length, corresponding to a horizontally broadened peak. These two broadening effects can be separated in an asymmetrical scan. The mosaic tilt is extracted from the full width at half maximum (FWHM) in the mosaic direction and the lateral coherence length is extracted from the FWHM in the lateral direction.

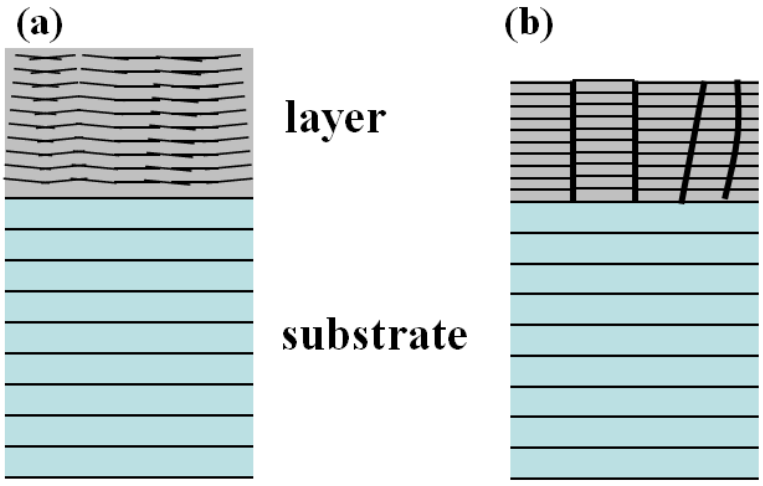

Figure 2.7 Schematic diagram of a heteroepitaxial layer (a) with mosaic structure, (b) with limited lateral coherence length.

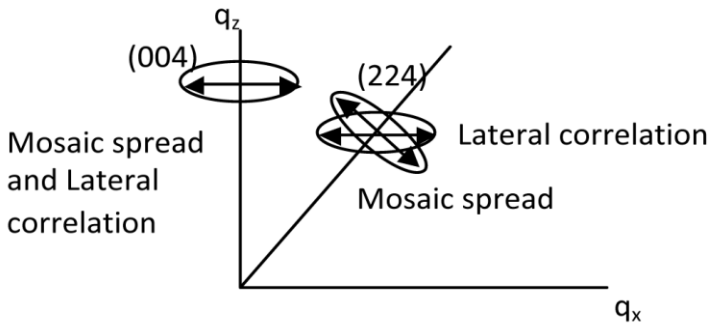

Figure 2.8 Schematic diagram of peak-broadening directions due to mosaic and lateral correlation spread.

Using these two FWHMs, we can characterize the crystalline quality of partially relaxed InGaAs buffer layers.[87] Strain relaxation is followed by the formation of defects which broadens the diffraction peaks.[88-89] However, compared to misfit dislocations which are mostly confined in the interface, threading dislocations will propagate through the buffer layer and possible keep growing in the following active layer. Therefore, a high density of threading dislocation in the buffer layer will greatly degrade the quality of the active layer, which is highly undesirable. We have grown two step-graded InGaAs buffer layers by two methods. The first sample (sample A) is one in which all layers were grown at a high temperature of 540°C, and the (224) RSM scan and a TEM cross-section image are shown in Figure 2.9. Sample B was grown at 380°C followed by 540°C annealing as described previously. Figure 2.10 shows the (224) RSM scan and a TEM cross-section image.

The positive correlation between the FWHM in lateral direction in the (224) RSM and the threading dislocation density (TDD) is confirmed by comparing the peak shapes of the second InGaAs buffer layers (the bottom peaks in RSMs) in two cases. The value of the FWHM laterally is almost 4 times larger for sample A (0.0043 rlu) compared to sample B (0.0012 rlu). Such a large value of lateral FWHM in sample A indicates a much higher TDD in the second buffer layer which reduces the coherent diffraction size significantly. This is confirmed by the TEM cross-section images.

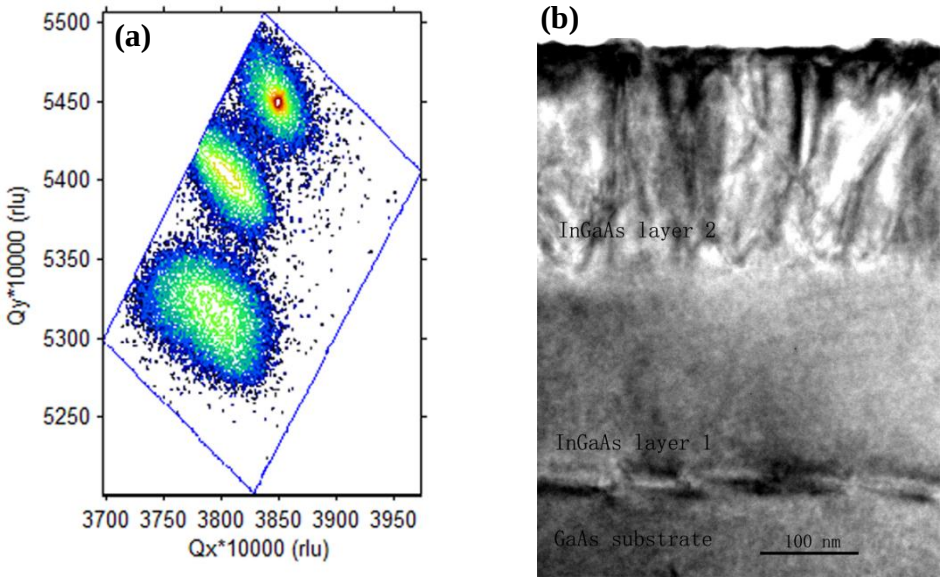

Figure 2.9 (a) (224) XRD-RSM of sample A, (b) TEM cross-section image.

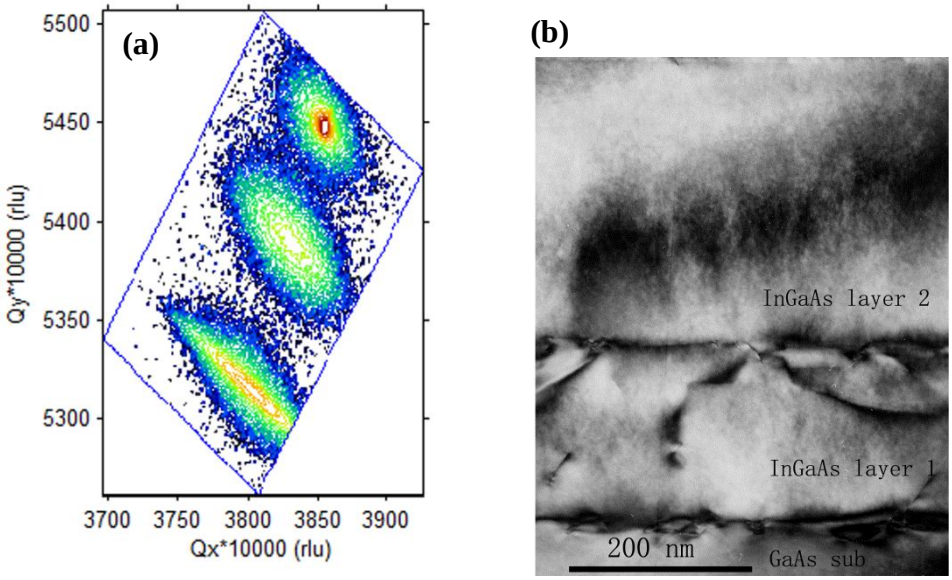

Figure 2.10 (a) (224) XRD-RSM of sample B, (b) TEM cross-section image.

The same result can be obtained by comparing the first and second buffer layers. For example, the first buffer layer peak has larger FWHM (0.0026 rlu) than the second buffer layer peak in sample B, because the TDD density is lower in the second layer as confirmed by the TEM image. Therefore, lateral FWHM of layer peaks in (224) RSM

scan is a good indicator of layer quality. In addition, good buffer layers or virtual substrates require the TDD to be as low as possible, especially for the topmost layer. Therefore, the growth method for sample B is used in this work to obtain good InGaAs buffer layers.

2.3.4 Raman spectroscopy

Raman spectroscopy relies on inelastic scattering of light. It has been widely used to study vibrational and rotational modes of molecule in chemistry. This technique can be applied to semiconductors as well. When laser light interacts with a semiconductor material, a phonon can either be created or absorbed, resulting in a scattered photon with either lower or higher energy than the incoming photon. As illustrated in Figure 2.11, when a phonon is created, the energy of the scattered light shifts downward. This process is known as Stokes scattering. When a phonon is absorbed in the process, the scattered light has a higher energy and is known as anti-Stokes scattering. Energy and momentum are conserved in both cases. The difference between the incoming and scattered photon is expressed as Raman shift in wavenumber.

$$\omega = (\frac{1}{\lambda_0} - \frac{1}{\lambda_1}) \qquad \text{Eq.2-4}$$

where ω is the Raman shift, λ_0 is the incoming light wavelength and λ_1 is the scattered light wavelength. Most commonly, the unit chosen for expressing wavenumber in Raman spectra is cm^{-1}. Raman shifts contain the information of phonon modes of the material, which are very sensitive to the structure of materials, such as strain and composition. For example, with high spatial resolution, Raman measurement is capable of mapping the strain levels in a wide variety of materials.[90]

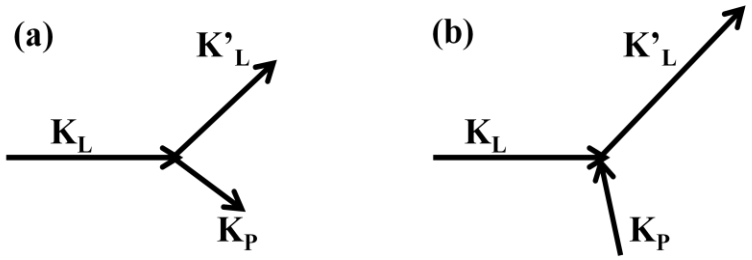

Figure 2.11 Schematic illustration of Raman scattering (a) Stokes scattering where a phonon is created (b) anti-Stokes scattering where a phonon is absorbed. L and P denote light and phonon.

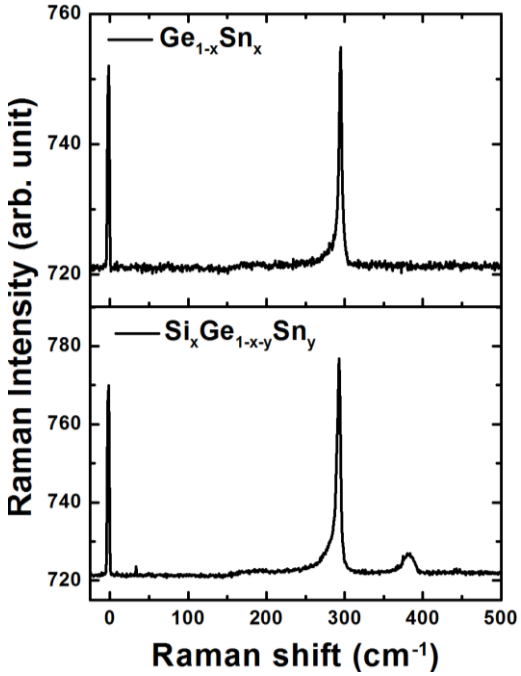

Figure 2.12 Raman spectra of $Ge_{1-x}Sn_x$ and $Si_xGe_{1-x-y}Sn_y$ alloys.

In this work, a Witec alpha500 Raman system with a 532nm laser was used to characterize all samples. Raman spectra were taken at room temperature in the (001) backscattering geometry and analyzed with a monochromator equipped with an 1800 lines/mm grating. With this geometrical configuration, and based on Raman selection rules,[91] only longitudinal optical (LO) phonon modes can be measured in either

diamond or Zinc-blende crystal structures. Figure 2.12 shows the typical Raman spectra of $Ge_{1-x}Sn_x$ and $Si_xGe_{1-x-y}Sn_y$ alloys. The peaks in $0cm^{-1}$ are the elastic scattering of the laser light. The peaks around $300cm^{-1}$ represent the Ge-Ge LO mode and the peak around $400cm^{-1}$ in $Si_xGe_{1-x-y}Sn_y$ alloys represents the Si-Ge LO mode. However, no Sn-related Raman peak was observed in the spectra. The shift of the Ge-Ge LO mode with respect to strain and composition is discussed in Chapter 3.

2.3.5 X-ray photoelectron spectroscopy

X-ray photoelectron spectroscopy (XPS) is a quantitative spectroscopic technique that measures the elemental composition, empirical formula, chemical state and electronic state of the elements. In XPS, soft x-rays illuminate a region of the sample being analyzed, and the kinetic energy and number of photoelectrons escaped from the top 1 to 10 nm of the material are analyzed. Therefore XPS measurement is very surface sensitive. Because the energy of an X-ray with a particular wavelength is known, the electron binding energy (BE) can be determined by using the equation

$$E_{binding} = E_{photon} - E_{kinetic} - \varphi \qquad \text{Eq.2-5}$$

where E_{binding} is the BE of the electron, E_{photon} is the energy of the X-ray photon being used, E_{kinetic} is the kinetic energy of the electron as measured by the instrument and φ is the work function of the spectrometer. From the binding energy, the elements and their chemical state can be determined.

The composition can be determined from the photoelectron counts N_e. N_e of a given element M is proportional to the composition of the element M, D_M.

$$N_e = AD_M \qquad \text{Eq.2-6}$$

where A is the sensitivity factor of the element, which takes into account of the properties of element M (photoelectron cross section, number of photoelectrons per atom) and experimental factors (detection efficiency of the spectrometer, analysis angle). For $Ge_{1-x}Sn_x$ alloys, the composition x can be calculated as

$$x = \frac{D_{Sn}}{D_{Sn}+D_{Ge}} = \frac{N_{Sn}}{N_{Sn} + N_{Ge}\frac{A_{Sn}}{A_{Ge}}} = \frac{N_{Sn}}{N_{Sn} + N_{Ge}R}$$ Eq.2-7

where R is the relative sensitivity factor (RSF), which is obtained from a reference sample with known composition. Rutherford backscattering spectroscopy can be used to determine the composition of the reference sample, because this measurement is unique in that it allows quantification without the use of reference standards.

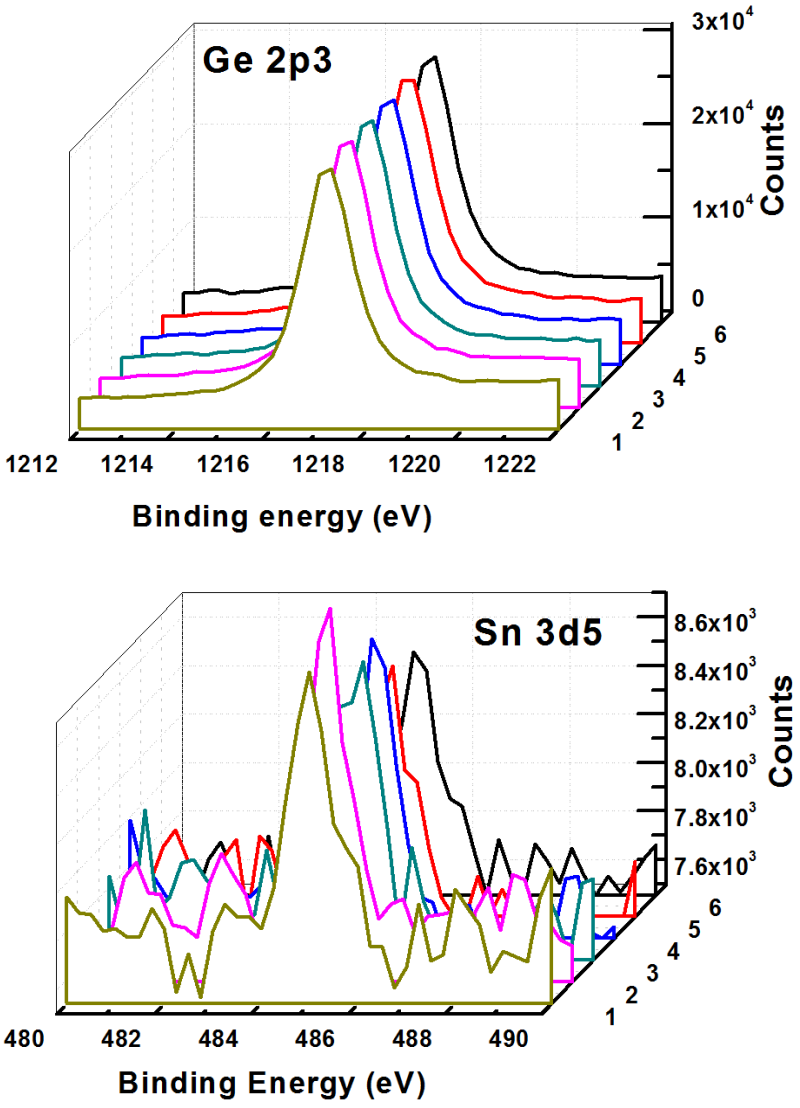

Figure 2.13 XPS depth profile data of a $Ge_{1-x}Sn_x$ sample with x=0.03.

In this work, a PHI VersaProbe Scanning XPS Microprobe with Al kα radiation (1486 eV) was used. It is also equipped with an argon ion sputter gun to clean the sample surface and to do depth profile analysis. We did a pre-sputter before data collection to remove the oxide from the surface. To determine the layer composition, we collected 6-8 series of data from Ge 2p3 and Sn 3d5 orbitals with a 30s sputtering performed between each data collection. Figure 2.13 shows the XPS depth profile data for a $Ge_{1-x}Sn_x$ sample with x=0.03. The signals from Ge 2p3 are smooth, and the integrated intensities are constant through the layer. However, due to a low composition, the signals from Sn 3d5 are noisy. Therefore, we performed curve fitting to calculate the integrated intensity and average the results from each scan to get the final Sn composition. For $Si_xGe_{1-x-y}Sn_y$ samples, Si 2p orbit was used with the RSF calibrated from a SiGe reference sample.

2.3.6 Secondary ion mass spectroscopy

Secondary ion mass spectrometry (SIMS) is a technique used in materials science to analyze composition. In SIMS, a primary ion beam bombards the sample surface, and produces secondary particles, which carry negative, positive and neutral charges with kinetic energies from zero to several hundred eV. Only the secondary ions are collected and analyzed by a mass spectrometer. Today, SIMS is widely used for analysis of trace elements in solid materials, especially in semiconductors and thin films. The detection limits for most trace elements are between $1e^{12}$ and $1e^{16}$ atoms/cc. During SIMS analysis, the sample surface is slowly sputtered away. Continuous analysis while sputtering produces a depth profile. Sputter rates in typical SIMS experiments vary between 0.5 and 5nm/s, which depend on the primary beam intensity, sample material, and sputter area (raster area). The slower the sputter rate, the finer the depth resolution. Quantitative analysis in SIMS also follows the same method used in XPS. In order to determine the composition, we need to measure the relative sensitivity factors from a reference sample as well.

In this work, a CAMECA NanoSIMS 50L system was used. A primary Cs^+ beam of about 100 nA, with an energy of 16 kV, was rastered on surface areas of 20×20 or 30×30 μm^2. Only the secondary ions from the center of the raster (one quarter of the raster size) were analyzed. Counting times were 1s for all masses. Figure 2.14 shows the SIMS depth profile of a $Ge_{1-x}Sn_x$ reference sample. Signals from Ge^{72}, Sn^{120} and As^{75} are plotted as a function of the sputtering time. The rapid intensity increase at the beginning is due to Cs+ implantation and is not related to $Ge_{1-x}Sn_x$ sample. After Cs+ implantation becomes stable, the intensity for each element is quite constant through the layer, indicating a uniform composition in the growth direction. The RSF for Ge^{72}/Sn^{120} pair was calculated and used to determine Sn compositions of other samples. For $Si_xGe_{1-x-y}Sn_y$ samples, Si^{28}, Ge^{72}, and Sn^{120} were measured, and one more SiGe reference sample was used to calibrate the RSF of Si^{28}/Sn^{120}.

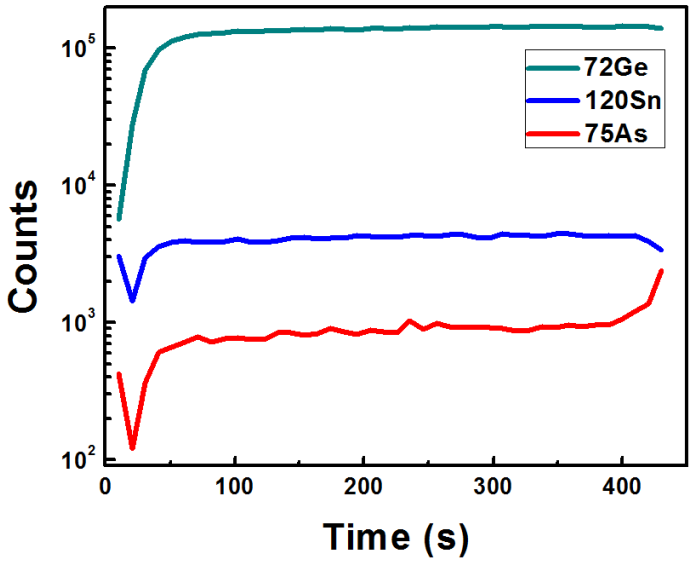

Figure 2.14 SIMS depth profile of a $Ge_{1-x}Sn_x$ sample with x=0.042.

2.3.7 Photoreflectance spectroscopy

2.3.7.1 Principle of photoreflectance spectroscopy

Photoreflectance spectroscopy (PR) is one of the modulation spectroscopes, which have proven to be powerful experimental techniques for characterizing the optical properties of semiconductors. Modulation spectroscopes deal with the measurement and interpretation of changes in the optical response of a sample which are caused by modifying the measurement conditions in some way, such as temperature and electrical field. The observed normalized changes are usually small so that the difference signals are closely related to a derivative of the absolute spectrum with respect to the modifying parameter. Therefore weak features that may be difficult to observe in the absolute reflection or absorption spectrum can be enhanced. The derivative nature of modulation spectroscopy emphasizes structure localized in the photon energy region of interband transitions in semiconductors and suppresses uninteresting background effects.[92] Therefore, it is a useful technique to study the direct band gap energy of semiconductors.

Photoreflectance spectroscopy varies the internal (build-in) electric field of the sample by photo-excited electron-hole pairs created by a pump source (usually a laser) which is chopped at some relatively low frequency. The photon energy of the pump source is generally above the band gap of the semiconductor being investigated. Figure 2.15 demonstrates the mechanism of photo-induced modulation of the built-in electric field in an n-type semiconductor.[93-94] Because the Fermi energy is pinned at the surface, there exists a space-charge layer. The occupied surface states contain electrons from the bulk, as shown in Figure 2.15 (a). When the pump source illuminates the sample, photo-excited electron-hole pairs are separated by the built-in electric field, with the minority carrier (holes for this case) being swept toward the surface. At the surface, the holes neutralize the trapped charge, reducing the built-in field, as shown in Figure 2.15 (b).

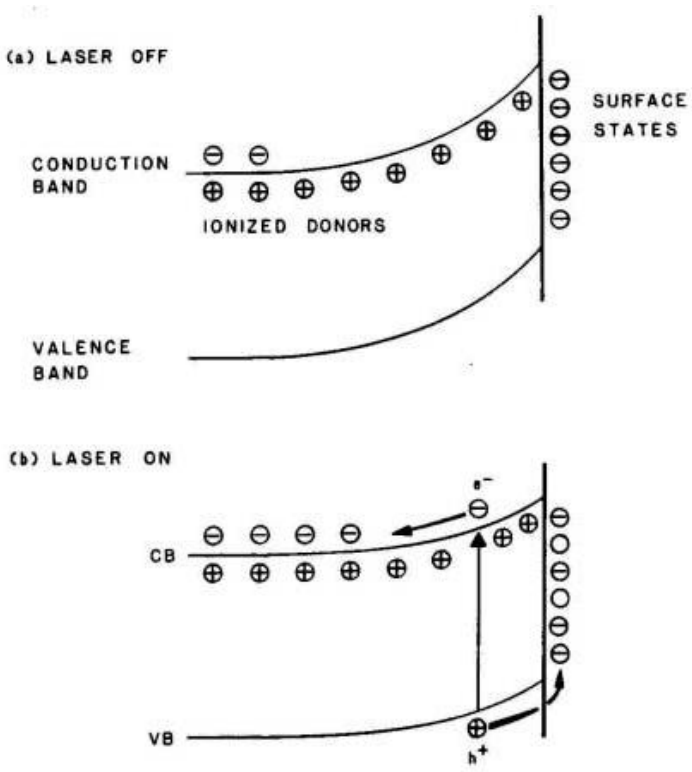

Figure 2.15 Schematic representation of the photoreflectance effect for an n-type sample. (a) Without a laser incident, Fermi-level pinning due to surface states induces a build-in electric field. (b) Carriers generated by the laser separate in the field, and change the intensity of the build-in electric field.

The surface field modulation causes modulation of the complex dielectric function ($\varepsilon = \varepsilon_1 + i\varepsilon_2$) of the sample under investigation. Changes in the dielectric function are directly connected with changes of reflectivity of the sample. Therefore, a probe light is used to measure the relative changes in reflectivity in PR. The relative change is defined as $\frac{\Delta R}{R} = \frac{R_{on} - R_{off}}{R_{off}}$, where R_{off} and R_{on} are the intensity of reflected probe light when the pump beam is off and on, respectively.

Differential changes in reflectivity can be related to the perturbation of the complex dielectric function ($\varepsilon = \varepsilon_1 + i\varepsilon_2$) and are expressed as[95-96]

$$\frac{\Delta R}{R} = a(\varepsilon_1, \varepsilon_2)\Delta\varepsilon_1 + b(\varepsilon_1, \varepsilon_2)\Delta\varepsilon_2 \quad \text{Eq.2-8}$$

where a and b are Seraphin coefficients, related to the unperturbed dielectric function, and $\Delta\varepsilon_1$ and $\Delta\varepsilon_2$ are the changes in the complex dielectric function due to the perturbation. The quantities $\Delta\varepsilon_1$ and $\Delta\varepsilon_2$ are related by a Kramers-Kronig inversion. Near the fundamental gap of bulk materials b ≈ 0. The functional form of $\Delta\varepsilon_1$ and $\Delta\varepsilon_2$ can be calculated for a given perturbation provided that the dielectric function and critical point in the Brillouin zone (BZ) are known.

PR spectrum can be classified into three categories, low-, intermediate- and high-field regime depending on the relative strengths of certain characteristic energies. In the low field region, $|\hbar\theta| \leq \Gamma$, where Γ is the broadening parameter and $\hbar\theta$ is the electro-optic energy given by $(\hbar\theta)^3 = q^2\hbar^2F^2/2\mu_{\|}$, where F is the field and $\mu_{\|}$ is the reduced interband mass in the direction of the field. In the intermediate-field case $|\hbar\theta| \geq \Gamma$ but $eFa_0 \ll E_g$, where a_0 is the lattice constant and E_g is the band gap. In this case, Franz-Keldysh oscillations (FKOs) appear in the spectra, which are caused by photo-assisted tunneling.[97-98] In the high-field regime, the electro-optic energy is again much greater than the broadening but $eFa_0 \approx E_g$ so that Stark shifts are produced.

2.3.7.2 Photoreflectance system setup

A PR measurement system was designed and built to study the optical properties in this work. A schematic diagram of this system is shown in Figure 2.16. A frequency doubled 532nm Nd: YAG laser with about 20mW power was used as the pump light. The power was adjusted by neutral density filters. This laser light was modulated by a chopper at a frequency of 320Hz and focused onto the sample. White light from a halogen lamp passed through a scanning monochromator with intensity I_0 and focused onto the laser spot on the sample surface as the probe light. The reflected probe light from the sample was collected by an extended wavelength InGaAs detector that was thermo-electrically cooled to $-30℃$. A long pass filter (1200nm or 850nm) was

placed in front of the detector to eliminate the scattered laser light and higher-order diffracted light passing through the monochromator. The light striking the detector containing the AC signal proportional to $I_0\Delta R$ was measured by a lock-in amplifier and recorded by a computer. The reflected probe light proportional to I_0R was measured separately without laser pumping. Typically $I_0\Delta R$ is 10^{-4}-10^{-6} of I_0R. In order to evaluate the quantity of interest, a normalization procedure was used to eliminate the uninteresting common feature I_0. The control and data acquisition programs were written in Labview.

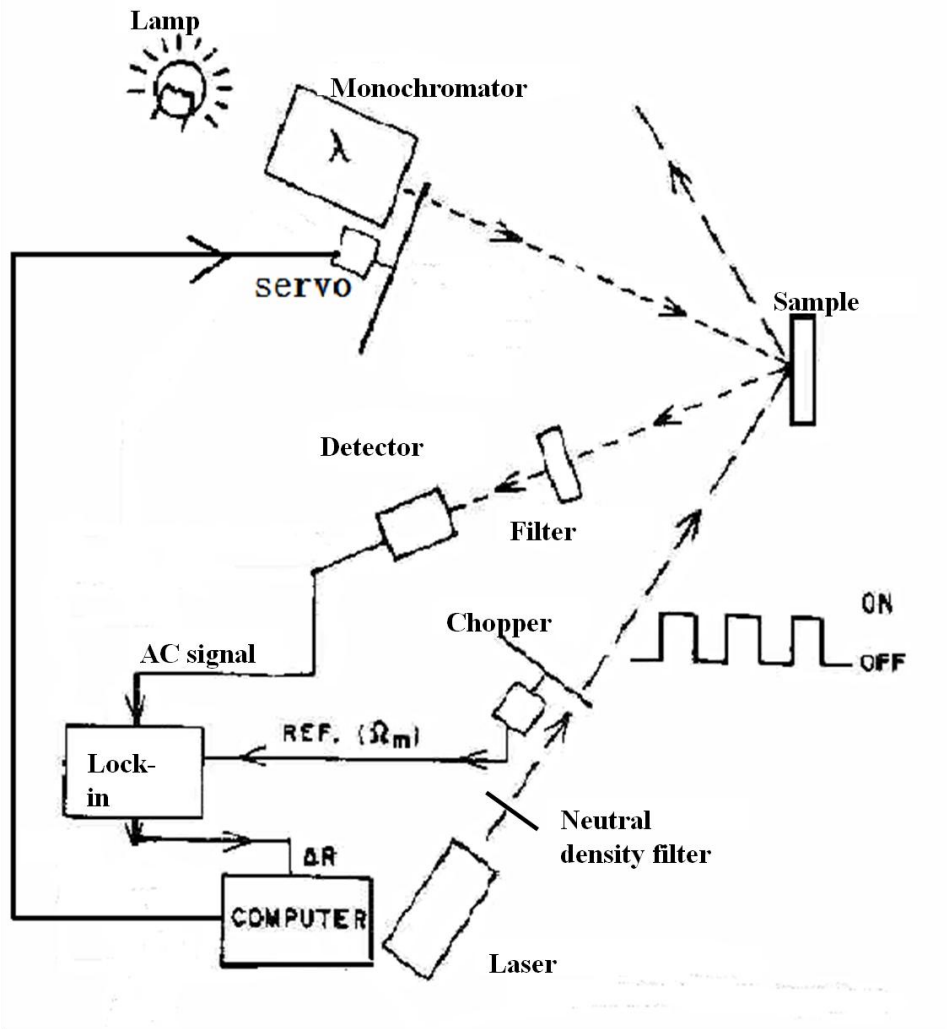

Figure 2.16 Schematic diagram of the PR measurement setup.

In the case of PR measurements, a common problem is the spurious background signal from the luminescence of the sample, especially for measurements near the fundamental band gap. Unfortunately, this signal is phase locked to the modulation source and is not constant over time due to fluctuations in laser power. If it is not treated properly, it can greatly distort the PR spectrum and lead to erroneous results. There are several ways to solve this problem: (1) add appropriate filters in front of the detector to attenuate the unwanted signal, (2) reduce the laser intensity, and (3) subtract the PL signal. The first method does not work in our case since the PL wavelength lies in the region of interest of the PR spectrum. The second method results in a poor signal to noise ratio in the PR signal as well. In this study, the third method was used. A mechanical shutter was installed in front of the monochromator to control the probe light on and off. When the shutter is open, the detector collects the AC signal containing both PL and PR signals. When the shutter is closed, the AC signal only contains the PL signal. For each wavelength, two data points were taken subsequently with and without probe light, and the pure PR signal can be obtained after subtracting the PL signal, which was assumed to be constant during the measurement time (less than 1min).

2.3.7.3 Lineshape analysis and modulus analysis

The ability to perform a lineshape fit is one of the great advantages of photoreflectance spectroscopy. For well known critical points in the Brillouin zone, it is possible to account for the lineshape to yield accurate values of energies and broadening parameters of interband transitions.

For interband transitions in bulk semiconductors in the low built-in electric field regime, the lineshape of the PR spectrum is the third derivative of the unperturbed dielectric function. If the form of the dielectric function ε is Lorentzian, Eq.2-8 takes a particularly simple form as presented below.

$$\frac{\Delta R}{R} = Re[Ce^{i\varphi}\left(E - E_g + i\Gamma\right)^{-m}] \quad \text{Eq.2-9}$$

where C is the amplitude, φ is a phase angle which accounts for Eq.2-8 and the influence of non-uniform electric fields as well as interference and electron-hole interaction effects. E_g is the transition energy, E is the photon energy, Γ is the broadening parameter. The parameter m in the lineshape factor of Eq.2-9 depends on critical point type. For a three-dimensional M_0 critical point, such as the direct gap of GaAs, m is chosen to be 2.5. For a two-dimensional critical point m=3.[92]

As discussed above, the third-derivative nature in the low-field regime is a consequence of the fact that the electric field can destroy the translational symmetry of the material and accelerate the electrons/holes in the sample. For confined systems, such as the isolated states of quantum wells, excitons, impurities, etc., the carrier and its wavefunction are localized in space. Several authors have shown that under these conditions, the change in the dielectric function induced by the modulating field is a first-derivative. On the other hand, the unperturbed dielectric function can be either a Lorentzain or Gaussian function. Therefore, more complicated expressions are required to analyze the lineshape.[92, 95-96]

In this work, only the third derivative of a Lorentzian line profile is considered since Eq.2-9 is a good description for the near band gap transitions at room temperature.

Rather than lineshape analysis discussed above, we considered Kramers-Kronig analysis to calculate the modulus for the PR spectrum as well.[99-101] We can define the complex PR function as

$$\Delta\rho(E) = \Delta\rho_R(E) + i\Delta\rho_I(E) = \frac{\Delta R}{R}(E) + i\Delta\rho_I(E) \quad \text{Eq. 2-10}$$

where the measured quantity $\Delta R/R$ is the real part of the complex photoreflectance function $\Delta\rho$, and the imaginary part of this function can be calculated from the Kramers-Kronig relations by,

$$\Delta\rho_I(E_0) = \frac{2E_0}{\pi} P \int_{E_b}^{E_a} \frac{\Delta R}{R} \frac{1}{\left({E_0}^2 + E^2\right)} \mathrm{dE} \qquad \text{Eq. 2-11}$$

where symbol P$\int$ means the principal value of the integral. E_a and E_b determine the energy range over which $\Delta R/R$ is measured. The values of these energy limits must be chosen to have $\Delta R/R(E_a)$ and $\Delta R/R(E_b)$ already equal to zero. Knowing the imaginary part of the complex PR spectrum enables us to determine the modulus of the PR transition.

$$|\Delta\rho(E)| = \sqrt{\Delta\rho_{\mathrm{R}}^2(\mathrm{E}) + \Delta\rho_{\mathrm{I}}^2(\mathrm{E})} \qquad \text{Eq. 2-12}$$

For the Lorentzian lineshape described by Eq.2-9, $\Delta\rho$ modulus can be determined as follows:

$$|\Delta\rho(E)| = \frac{C}{\left((E - E_g)^2 + \Gamma^2\right)^{m/2}} \qquad \text{Eq. 2-13}$$

The advantage of such analysis is that we do not have to consider the PR lineshape (Lorentzian or Gaussian, first or third derivate). This advantage becomes important in the analysis of the temperature dependence of the spectra, where the line shape can change from a Lorentzian-like to a Gaussian-like shape due to changes in the dominant scattering processes. As a common fitting procedure, in addition to the transition intensity, the Kramers-Kronig analysis provides the energy and broadening of the transition. Only the information concerning the phase angle is lost. A disadvantage of this method is the necessity to have well separated PR resonances to correctly determine the integration limits for a particular transition.

A comparison of the analysis of PR data using the standard fitting procedure and Kramers-Kronig analysis is shown in Figure 2.17. Figure 2.17 (a) shows the experimental data (open circle) of a Ge wafer PR spectrum measured using our PR setup at room temperature. The data are fitted by Eq.2-9 with m=2.5 (red solid line). Figure 2.17 (b) shows the modulus of the PR resonance calculated by Eq. 2-12 (black dot), and the modulus fitting using Eq. 2-13 (blue line) with m=2.5.

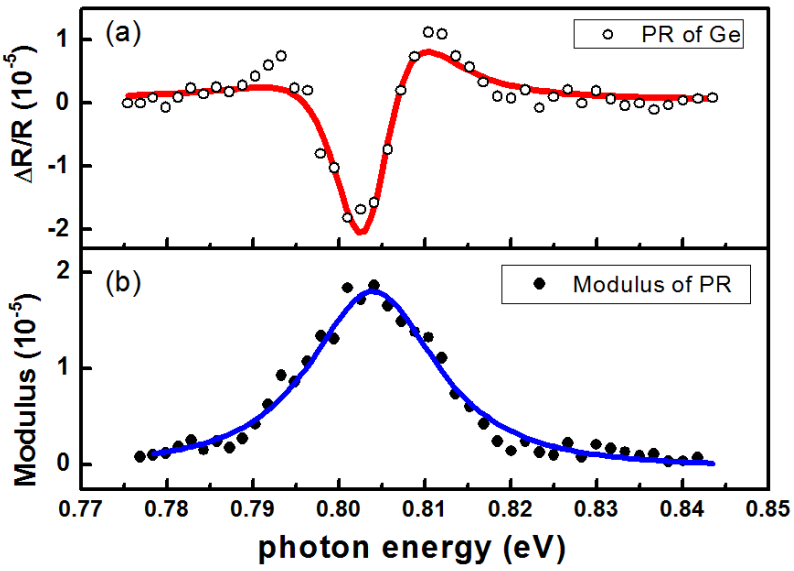

Figure 2.17 Comparison of the two PR analysis methods: (a) PR spectrum (open circle) of a Ge wafer measured at room temperature and the standard fitting (red line), and (b) the modulus of the PR spectrum calculated using Eq. 2-12 (black dot) and the Kramers-Kronig fitting (blue line)

Table 2.2 Shows the data obtained from the two different fitting methods. The results are quite close, especially for the transition energy E_g. We determine the direct band gap energy of Ge to be 0.804eV, which is very close to the value 0.8eV published in literature for bulk Ge. Therefore, we believe that our home-built PR setup is well calibrated and the PR analyses are accurate in this work.

Table 2.2 The fitted results from two PR analysis methods

	E_g (eV)	**C**	**Γ (eV)**
Standard fitting	0.804	9.89×10^{-11}	0.0073
Modulus fitting	0.804	1.98×10^{-10}	0.0103

2.3.8 Photoluminescence

Photoluminescence (PL) is a process in which a material absorbs photons and then re-emits photons characteristic of its electronic states. It is a contactless, nondestructive method of probing the electronic structure of materials, especially the band gap information for semiconductors. As shown in Figure 2.18, for a direct bandgap semiconductor, during PL, when a pump light (laser with higher energy than the bandgap of the sample) strikes the sample, electron-hole pairs (EHP) are generated. The carriers are quickly thermalized to the lowest energy of their respective bands, and eventually recombine, emitting a photon very close to the bandgap energy of the sample. The light emitted from the sample is collected and resolved in wavelength and Gaussian curve can be used to fit the PL spectra.[57] The PL peak energy is very close to the direct bandgap energy of the sample. Carriers may be lost to Shockley-Read-Hall recombination in the material with defects or impurities. For an indirect bandgap semiconductor, because the lowest energy of conduction band is not at the Brillouin zone center, a phonon is required to complete the recombination process. Therefore, the PL efficiency is much lower, and the PL peak energy is the indirect band gap energy plus or minus the energy of a phonon.

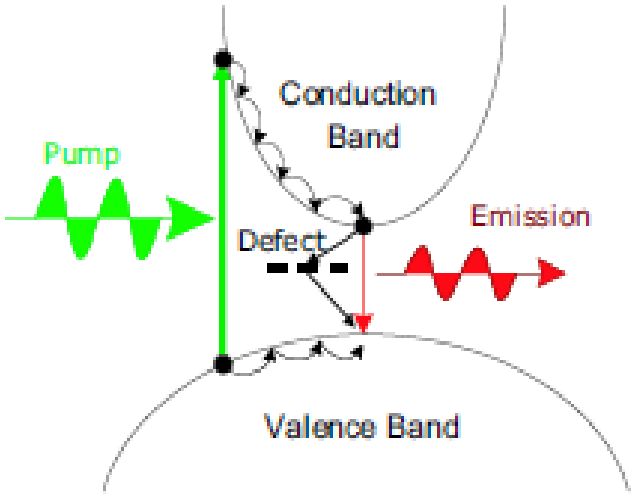

Figure 2.18 E-k description of the various processes occurring during PL.

In addition, temperature-dependent PL has been widely used to study the mechanisms of recombination. Both the position and intensity of the PL peak change with temperature. The semiconductor bandgap increases with decreasing temperature, so the PL peak position will move to a shorter wavelength range in low temperatures monotonically. The deviation at low temperatures, for example the PL peak moves to a longer wavelength with decreasing temperature, can give information about phase segregation.[102] Also the carrier distribution among direct and indirect valleys depends on temperature, so the intensity of PL peaks will change correspondingly. This feature can be used to characterize light emitting mechnisms.[16]

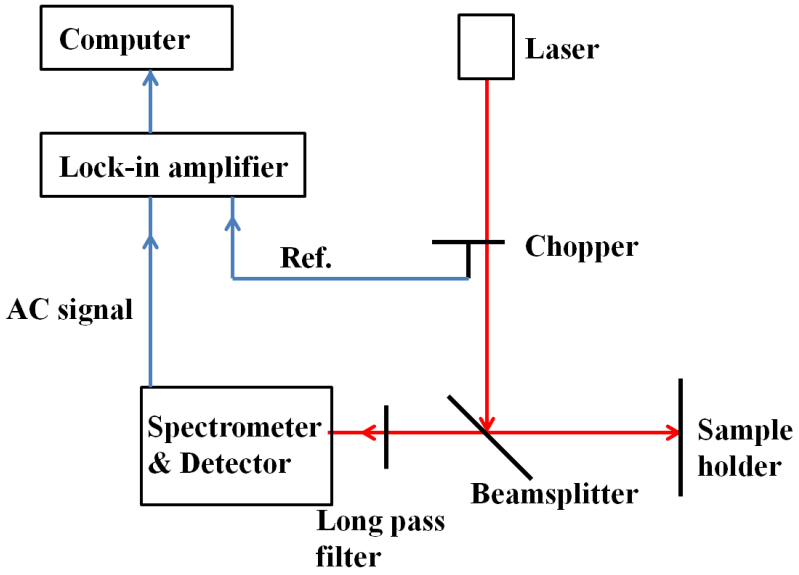

Figure 2.19 Schematic diagram of the PL measurement system

The PL system used in this work is illustrated in Figure 2.19. A frequency doubled 532nm Nd: YAG laser was used as the pump light. The maximum power of the laser is 200mW. A850nm long pass filter was placed in front of the spectrometer to remove the reflected laser light, and an OD4 1400nm long pass filter was added as well to remove contributions from the higher-order diffraction peaks from shorter wavelength. To optimize the long wavelength signal, a 300g/mm grating with blazing wavelength at 2μm was used in the spectrometer and an extended wavelength InGaAs detector that was thermo-electrically cooled to −30℃ was used. The chopper and lock-in amplifier

were used in this system to enhance the signal-to noise ratio. The sample holder can be cooled down to 20K by liquid He. Data collection and analysis were performed by a computer. It is important to remove the wavelength response of the setup from the measured data. A broadband, "white", light source was employed to measure this system response. Each measurement was then divided by the system response.

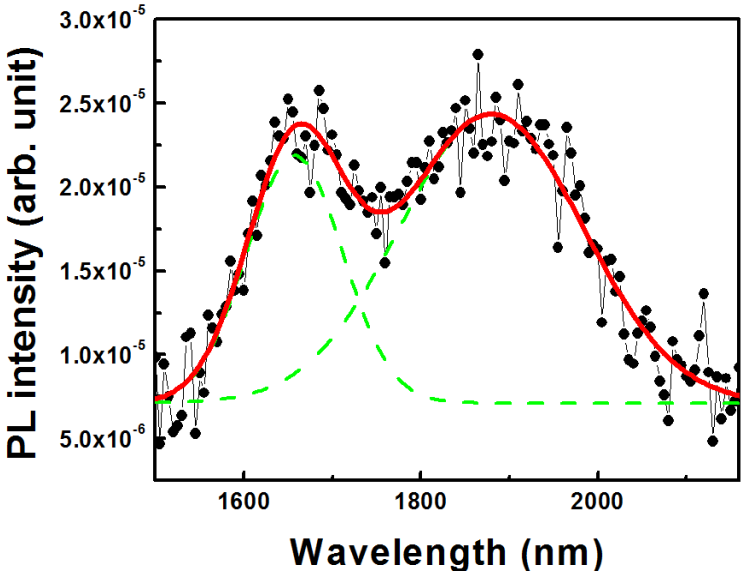

Figure 2.20 PL spectrum of a $Ge_{1-x}Sn_x$ sample with x=0.03 and 0.513% compressive strain at 240K.

Figure 2.20 shows the PL spectrum of a $Ge_{1-x}Sn_x$ sample with x=0.03 and 0.513% compressive strain at 240K. The system response has been removed. Two transition peaks corresponding to the direct and indirect band transitions can be clearly observed in the spectrum. Two Gaussian curves (green dashed lines) are used to fit the data, and the combined result is plotted as the red line. In this way, we can determine the maximum positions of these two peaks at 1657nm and 1879nm, corresponding to 0.748eV and 0.660eV, respectively. More details of the temperature-dependent PL of $Ge_{1-x}Sn_x$ alloys are discussed in Chapter 4 of this dissertation.

2.4 Conclusion

This chapter has discussed the MBE growth mechanisms and characterization methods for $Ge_{1-x}Sn_x$ and $Si_xGe_{1-x-y}Sn_y$ alloys.

All samples were grown by MBE at low temperatures and the composition could be tuned by the growth rate of each of the alloy constituent elements. The advantage of using InGaAs buffer layers is to control strain and composition independently, therefore the effects due to these two aspects on materials properties can be decoupled. Structural and optical properties of the alloys were characterized by different methods. Detail results of the characterization will be discussed in the following chapters.

CHAPTER 3 $Ge_{1-x}Sn_x$ alloys

$Ge_{1-x}Sn_x$ alloys are predicted to become direct bandgap materials with about 6-10% Sn compositions. Due to their compatibility with current CMOS technology, $Ge_{1-x}Sn_x$ alloys are promising candidates for the active region of group IV lasers. In addition, strain can be applied to further enhance the optical properties of optoelectronic devices. Therefore, it is very important to understand the properties of $Ge_{1-x}Sn_x$ alloys with different compositions and different levels of strain. In this chapter, growth and characterization of $Ge_{1-x}Sn_x$ alloys are discussed. Composition and strain effects on material properties are decoupled and determined independently.[52, 56]

3.1 Crystal growth

$Ge_{1-x}Sn_x$ alloys of different Sn compositions and different levels of strain were grown by MBE. Due to the difficulty of incorporating Sn into Ge crystal lattice at high temperatures, the thermal budget for MBE growth was studied. With the same growth rates of Ge and Sn, $Ge_{1-x}Sn_x$ layers were grown on GaAs substrates at 400°C and 200°C. The (004) XRD rocking curve measurements are plotted in Figure 3.1, in which the XRD of a Ge layer on GaAs substrate is plotted as a reference. The GaAs substrate peaks overlap perfectly for all samples. The layer peaks have lower omega angles corresponding to larger out-of-plane lattice constants than that of the GaAs substrate. Thickness fringes appear in all spectra, indicating coherent growth in all cases, because if the layer is relaxed, the dislocations formed in the interface will destroy the fringes. Therefore, the lower the omega angle, the larger the lattice constant, thus the higher the Sn composition. Although two $Ge_{1-x}Sn_x$ samples are expected to have same Sn composition from the growth rate, the sample grown at 400°C contains a lower Sn composition than the sample grown at 200°C. Apparently, at the higher temperature, not all the Sn deposited on the substrate is incorporated into

the crystal lattice. Therefore, low temperature growth is essential for $Ge_{1-x}Sn_x$ alloys. In this work, the growth temperature was chosen to be 200°C to avoid Sn surface segregation. Further characterization will be discussed in the following section.

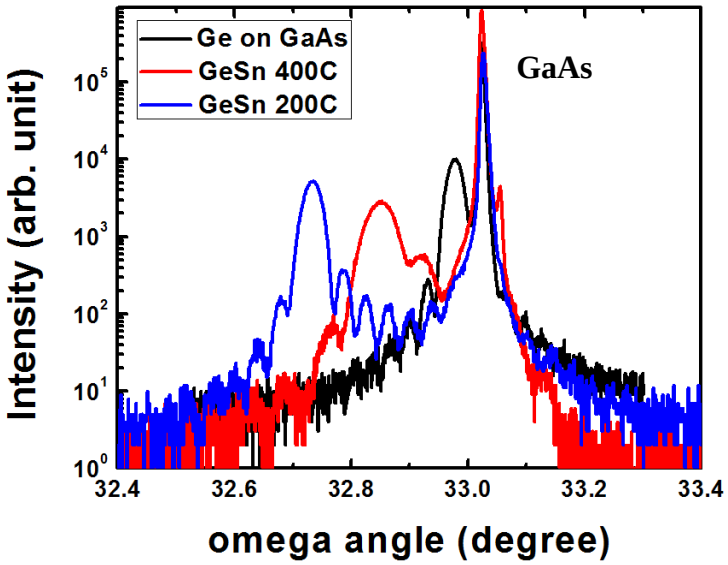

Figure 3.1 (004) XRD rocking curve measurements of a Ge layer grown on GaAs substrate (black) at 400°C, a $Ge_{1-x}Sn_x$ layer grown on GaAs substrate at 400°C (red), and a $Ge_{1-x}Sn_x$ layer grown on GaAs substrate at 200°C (blue).

3.2 Composition and strain determination

Accurate Sn composition determination in $Ge_{1-x}Sn_x$ layers is very important in the study of composition-dependent material properties. Therefore three methods were used in this work: XRD-RSM, SIMS, and XPS measurements. A $Ge_{1-x}Sn_x$ reference sample with x=0.042 calibrated by Rutherford backscattering spectrometry (RBS) was used to calculate the relative sensitivity factors (RSFs) to be used for XPS and SIMS measurements. For the XRD-RSM measurement, Vegard's law is assumed to be valid for $Ge_{1-x}Sn_x$ alloys lattice constant. The small deviation from Vegard's law is ignored

because the bowing coefficient is not well known, with inconsistent theoretical and experimental values.[103]

These three measurement methods give consistent Sn compositions. Figure 3.2 shows the correlation between the Sn composition determined by XRD-RSM and SIMS. The red line is a linear fit to the data with a slope of 0.97 ± 0.06. Figure 3.3 shows the correlation between Sn composition obtained from XPS and XRD-RSM. The slope of the linear fit line is 1.07 ± 0.05. Both linear fitting lines go through the origin and have almost unit slope, which indicates the strong one-to-one correlation of the results from all three measurement techniques. These three measurement techniques rely on different mechanisms; showing consistent results proves that the Sn compositions determined in our work are accurate. We can use any method to determine the Sn composition. For thicker $Ge_{1-x}Sn_x$ layers, XRD-RSM measurement is very easy to perform and it can also determine the strain, while XPS is ideal for thinner layers. SIMS depth profile can be used to determine the uniformity in depth. As shown in Figure 2.14, the constant intensities of Ge and Sn indicate a uniform composition in the growth direction.

In addition, consistent results from XRD-RSM and elemental analysis methods like SIMS, suggest that the assumption of Vegard's law is valid in the Sn composition range we studied. With a known Sn composition, the natural or unstrained lattice constant of $Ge_{1-x}Sn_x$ can be easily calculated. Therefore, the in-plane strain of each $Ge_{1-x}Sn_x$ layers can be calculated from the in-plane lattice constant determined from XRD. The ability to accurately determine the Sn composition and strain allows us to correlate the dependence of the material properties on these two effects.

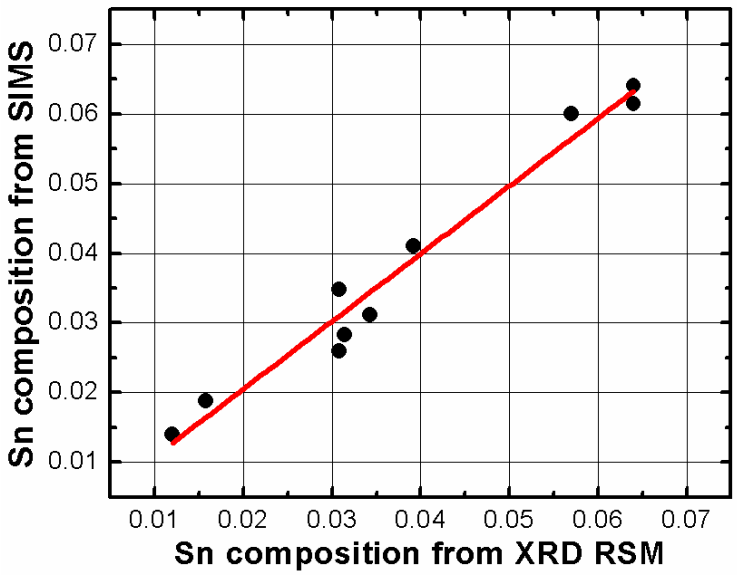

Figure 3.2 Comparison of Sn compositions determined by SIMS and XRD-RSM. The red line is a linear fit to the data. The slope of the fitting line is 0.97 ±0.06.

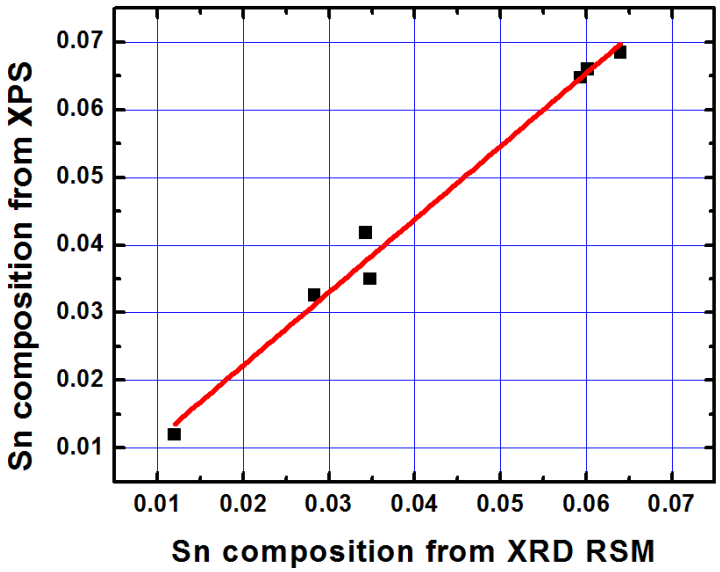

Figure 3.3 Comparison of Sn compositions determined by XPS and XRD-RSM. The red line is a linear fit to the data. The slope of the fitting line is 1.07 ±0.05.

3.3 Structural properties of $Ge_{1-x}Sn_x$ alloys

3.3.1 Characterization of unstrained $Ge_{1-x}Sn_x$ layers

As discussed in Chapter 2, using InGaAs buffer layers on GaAs substrates allows the control of strain in the $Ge_{1-x}Sn_x$ layers grown on top. In this section, unstrained $Ge_{1-x}Sn_x$ layers were characterized first. Four samples with different Sn compositions ranging from 1% to 10.5% were grown with 50nm thickness, and the In compositions in the InGaAs buffer layers were chosen to lattice match the $Ge_{1-x}Sn_x$ layers as shown in Table 3.1. The surface morphology was characterized by AFM. Figure 3.4 shows 1×1 μm^2 AFM images of the four $Ge_{1-x}Sn_x$ samples. As listed in Table 3.1, the root mean square (RMS) roughness of each sample is less than 0.6 nm. Also the surface RMS roughness does not degrade with increasing Sn composition.

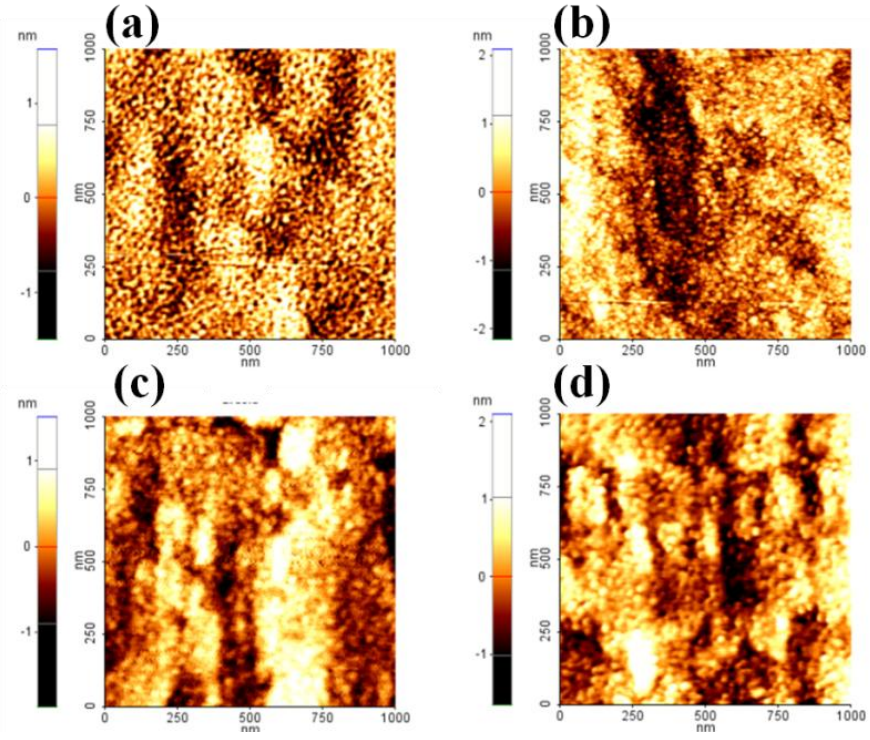

Figure 3.4 1×1 μm^2 AFM images of unstrained $Ge_{1-x}Sn_x$ layers with different Sn compositions from x=0.01 to 0.105.

Table 3.1 RMS roughness of the $Ge_{1-x}Sn_x$ samples shown in Figure 3.4.

	In composition	Sn composition	$1\times1\ \mu m^2$ RMS roughness
(a)	8%	1.03%	0.394 nm
(b)	11%	3.86%	0.577 nm
(c)	16%	6.75%	0.462 nm
(d)	26%	10.5%	0.519 nm

XRD-RSM (004) and (224) scans were measured to characterize crystal quality. Figure 3.5 shows the RSMs of the $Ge_{1-x}Sn_x$ sample (d) x=0.105 in Table 3.1. The $Ge_{0.895}Sn_{0.105}$ layer was grown on a two-step graded InGaAs buffer. The diffraction peak 1 comes from the GaAs substrate, peak 2 from the first InGaAs step buffer layer with 12% In composition, peak 3 from the second step buffer layer with 26% In, and peak 4 from the $Ge_{0.895}Sn_{0.105}$ layer. The buffer layers are tilted and partially relaxed, with the shape broadening mainly in the mosaic direction, indicating low density of threading dislocation. The coherent growth of the $Ge_{0.895}Sn_{0.105}$ layer on the InGaAs buffer layer is confirmed from the vertical alignment of peak 3 and 4, which means these two layers have the same in-plane lattice constant as designed.

TEM cross-section images were taken to further characterize the crystallinity. A (110) zone-axis bright-field image of the same $Ge_{0.895}Sn_{0.105}$ is shown in Figure 3.6(a). Clear interfaces can be seen between each layer. The interface between the $Ge_{0.895}Sn_{0.105}$ and the InGaAs buffer layers and the top $Ge_{0.895}Sn_{0.105}$ surface are sharp and smooth, which confirms a 2D growth mode. A RHEED pattern of straight lines was observed during growth as well. Misfit and threading dislocations due to relaxation are mainly confined in the InGaAs buffer layers. No visible dislocations can be found in the top $Ge_{0.895}Sn_{0.105}$ layer, indicating that the TDD is lower than $10^7\ cm^{-2}$. In addition, there is no evidence of Sn segregation with much higher Sn composition than the equilibrium solubility. A high-resolution TEM image of the top $Ge_{0.895}Sn_{0.105}$ layer is shown in Figure 3.6 (b). Clear lattice fringes indicate high crystal quality. Good crystal quality of other unstrained $Ge_{1-x}Sn_x$ samples is also confirmed by TEM.

Currently, we have only demonstrated up to 10.5% Sn composition, because this composition is already higher than the predicted indirect to direct bandgap transition point and sufficient for our study.

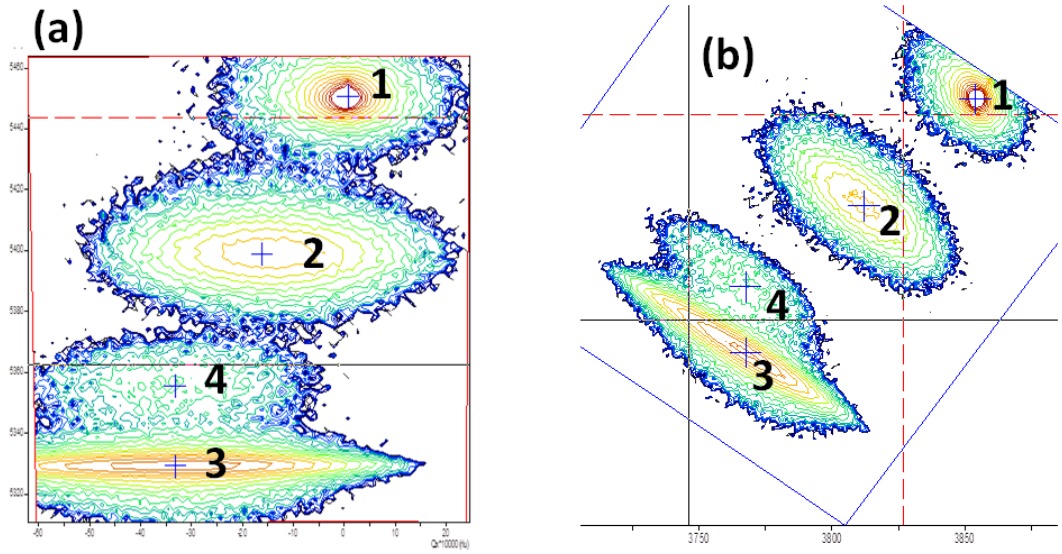

Figure 3.5 XRD-RSM of the $Ge_{1-x}Sn_x$ sample of 50nm with x=0.105 on two-step graded InGaAs buffer layers: (a) (004) symmetrical scan, (b) (224) asymmetrical scan.

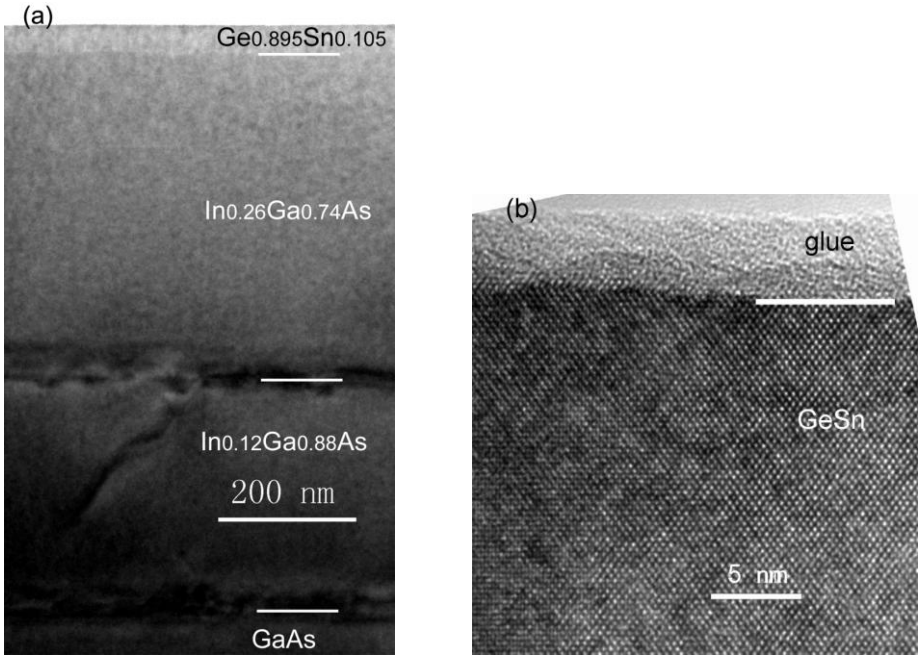

Figure 3.6 (a) TEM cross-section image of the $Ge_{1-x}Sn_x$ layer with x=0.105. (b) High resolution TEM image of the $Ge_{1-x}Sn_x$ layer.

3.3.2 Characterization of strained $Ge_{1-x}Sn_x$ layers

Compressive and tensile strained $Ge_{1-x}Sn_x$ layers were grown coherently on InGaAs buffer layers under their critical thicknesses, also by MBE. Crystal quality of the compressive-stained $Ge_{1-x}Sn_x$ layers is as good as that of unstrained layers, which is confirmed by AFM, TEM and optical measurements.

However, tensile-strained $Ge_{1-x}Sn_x$ layers have proven difficult to grow. Unlike the streaky RHEED pattern observed for unstrained and compressive-strained $Ge_{1-x}Sn_x$ layers, the RHEED pattern for the tensile-strained layers changes from streaky to broken lines after several nanometers of growth as shown in Figure 2.2(a). This dash-like RHEED pattern indicates a rough growth front, which is confirmed by AFM images. Figure 3.7(a) shows $1 \times 1\ \mu m^2$ AFM image of one 30nm thick $Ge_{1-x}Sn_x$ layer of x=0.047 with 0.68% tensile strain. The surface is quite rough with small bumps, and the RMS roughness increases to 1.572nm. The RMS roughness is greater for thicker

samples as well. There may be partial relaxation in the vicinity of the roughness on the film surface, but the bulk layer is not relaxed. From the (224) XRD-RSM scan of the sample shown in Figure 3.7(b), the diffraction peak from the $Ge_{0.953}Sn_{0.047}$ layer (peak 4) still aligns vertically with the peak from the second buffer layer (peak 3), which means the $Ge_{0.953}Sn_{0.047}$ layer is 100% strained to the InGaAs layer without relaxation. The out of plane lattice constant of the $Ge_{0.953}Sn_{0.047}$ layer shrinks accordingly.

This phenomenon does not depend on whether InGaAs or InAlAs buffer layers are used. Figure 3.8 shows the TEM cross section image of a tensile-strained $Ge_{1-x}Sn_x$ of x=0.03 on InAlAs buffer layers. The $Ge_{0.97}Sn_{0.03}$ layer is under 0.34% tensile strain, determined from XRD-RSM. The surface of the $Ge_{1-x}Sn_x$ layer is rough with small bumps as well. There are some defects in the layer beneath the intersection of bumps. Comparing samples with different strain, we found the higher the tensile strain, the rougher the surface, so one possible explanation is strain-induced surface roughening.[104] Further study is needed to explain the degraded material quality with tensile strain, and to find a new recipe to grow good quality tensile-strained layers.

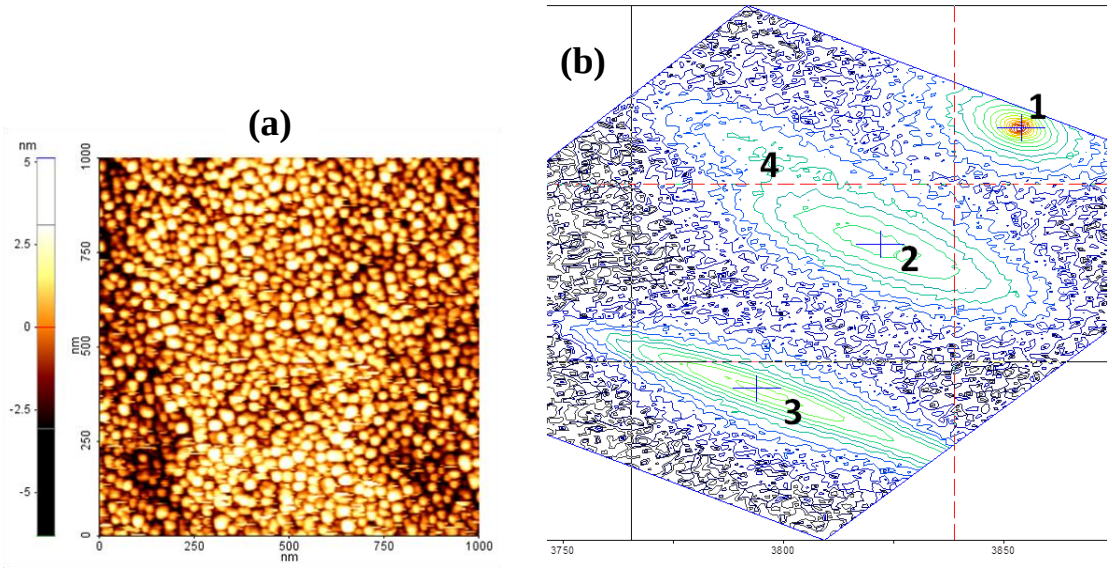

Figure 3.7 (a) 1×1 μm^2 AFM image of a $Ge_{1-x}Sn_x$ layer of x=0.047 with 0.68% tensile strain. (b) (224) XRD-RSM of the $Ge_{1-x}Sn_x$ sample.

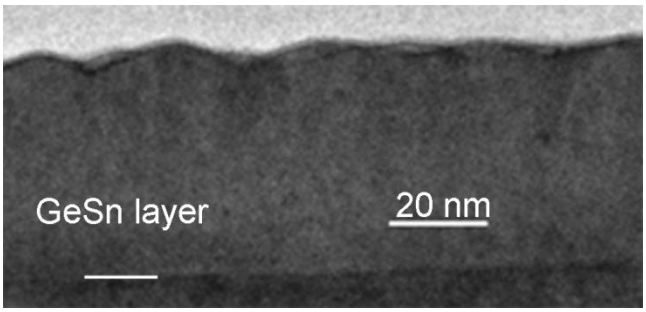

Figure 3.8 TEM cross-section image of a $Ge_{1-x}Sn_x$ layer of x=0.03 with 0.34% tensile strain.

3.4 Optical characterization

Photoreflectance (PR) and photoluminescence (PL) measurements have been employed to characterize the optical properties of $Ge_{1-x}Sn_x$ alloys. PR is very sensitive to direct band transitions, and it can distinguish the energy splitting of the heavy- and light-hole bands due to strain. In this work, PR measurements were performed at room temperature. A typical PR spectrum is shown in Figure 3.9. The sharp and intense feature in the high energy region is due to the InGaAs buffer layer, and the feature due to the $Ge_{1-x}Sn_x$ layer is in the lower energy region. These two PR transitions are well separated and do not interfere with each other, which eases the analysis. PL, on the other hand, collects spontaneous emission from all transitions, so deconvolution of peaks should be done with great care. Temperature-dependent PL spectra are used to distinguish different transition mechanisms. Heavy- and light-hole bands splitting cannot be detected by PL, because carriers will be scattered to the lowest energy band quickly due to fast thermalization process. These two methods together can give us a far more complete understanding of the optical properties of $Ge_{1-x}Sn_x$ alloys than was done in the past.

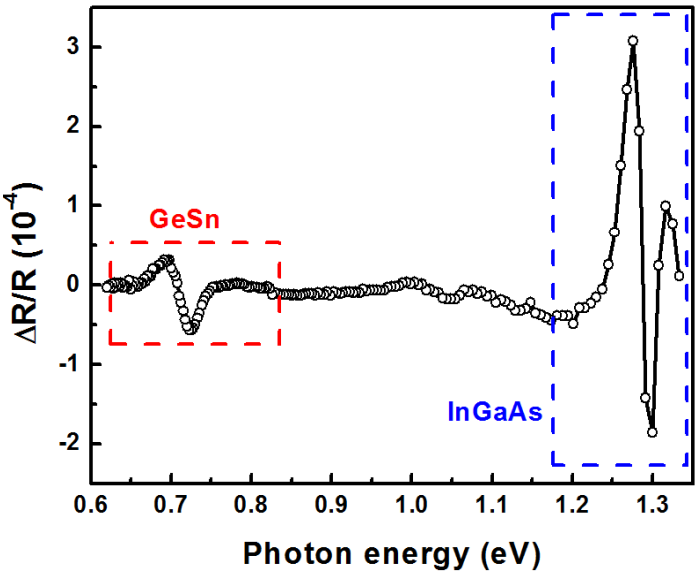

Figure 3.9 Room temperature PR spectrum of a $Ge_{1-x}Sn_x$ sample grown on an InGaAs buffer layer.

3.4.1 Composition contribution

The direct band gap of $Ge_{1-x}Sn_x$ alloys shrinks with increasing Sn composition. The relation is expressed by Eq.1-4, in which the bowing parameter b^{GeSn} describes the deviation from linear interpolation. With the band gap of Ge and Sn fixed, the bowing parameter is the only materials coefficient needed to describe the band gap change with respect to composition. In order to obtain an accurate value of the bowing parameter, 100nm unstrained $Ge_{1-x}Sn_x$ alloys were grown on InGaAs buffer layers to avoid the strain contribution. XRD-RSM and SIMS were used to determine the Sn composition and strain.

Figure 3.10 shows the PR spectra at room temperature of three $Ge_{1-x}Sn_x$ samples in the vicinity of the direct band gap E_g with Sn compositions from 3.6% to 6.4%. The strain is less than 0.05% for each sample and is thus negligible. The derivative-like features in the PR spectra shift to lower energy as the Sn composition increases. This feature represents the direct band transition from the maxima of the light- and heavy-

hole valence bands to the bottom of the conduction Γ valley. The low signal-to-noise ratio in the PR signal below 0.55eV is due to the detection limitation of the detector. Lineshape analysis and Kramers-Kronig modulus analysis were used to calculate the E_g. Since these samples are strain-free, the heavy- and light-hole bands are degenerate, therefore only one transition energy was used in the analysis. The direct bandgap energies calculated for $Ge_{1-x}Sn_x$ samples from both methods match well, and the results are listed in Table 3.2.

PL measurements at room temperature were performed for the samples as well, as shown in the red lines under the PR curve in Figure 3.10. The PL spectra are quite broad and they are deconvolved by Gaussian peaks to distinguish direct and indirect transitions. Compared with the PR spectra, the PL spectra are dominated by the direct band transition. The indirect transition is much weaker due to poor light emitting efficiency. The direct transition peaks in energies determined from the PL spectra are consistent with the direct bandgap energies obtained from the PR spectra, as shown in Table 3.2. In addition, another set of experiments demonstrated that the integrated intensity of the PL spectra increases largely with increasing Sn composition[57], which indicates an decreasing energy difference between the indirect and direct valleys.

Table 3.2 Sn composition, strain and direct bandgap energy measured by PR and PL at room temperature. The transition energies obtained from PR match those from PL.

Sn composition (%)	**In-plane strain (%)**	**E_g^Γ (eV)**	**E_g^Γ from PL (eV)**
3.59%	0%	0.674±0.002	0.663±0.005
4.83%	0%	0.630±0.002	0.625±0.005
6.42%	0%	0.577±0.003	0.576±0.005

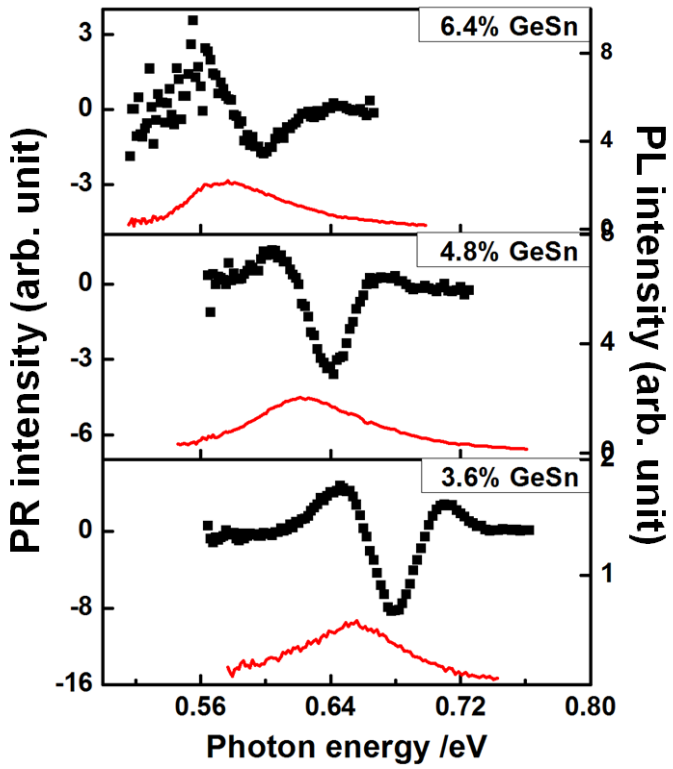

Figure 3.10 Room temperature PR spectra of unstrained $Ge_{1-x}Sn_x$ alloys with Sn compositions of 3.6%, 4.8% and 6.4% in black dots. The red lines below are the PL spectra at room temperature of each sample.

The direct bandgap energy determined from PR measurement for unstrained $Ge_{1-x}Sn_x$ is plotted as a function of Sn composition in Figure 3.11. The value 0.8eV for 0% Sn composition is from bulk Ge. The red-dashed line is a fitting of the direct bandgap energy according to Eq.1-4. From this fitting, the direct bandgap energy bowing parameter b^{GeSn} is calculated to be 2.42 ± 0.04eV. This number is very close to the value 2.1eV calculated purely from PL data[57], and other published data.[48, 50] This bowing parameter is a very important material parameter for $Ge_{1-x}Sn_x$ alloys, which describes the compositional dependent direct bandgap energy.

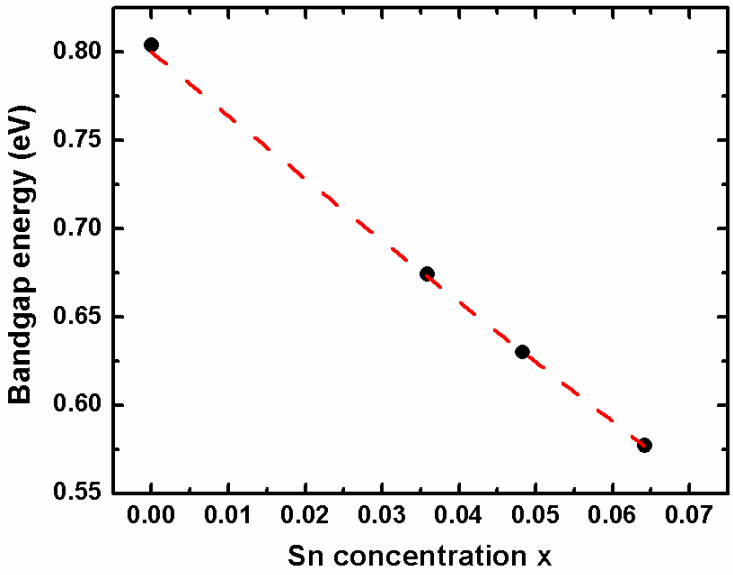

Figure 3.11 The direct bandgap energy of $Ge_{1-x}Sn_x$ alloys as a function of Sn composition. The red dashed line is a fitting of the data to Eq.1-4, and the direct band gap bowing parameter b^{GeSn} is found to be 2.42 ±0.04eV.

3.4.2 Strain contribution

In addition to Sn composition, strain will modify the band structure as well. These two effects can be combined together to enhance light emitting efficiency of $Ge_{1-x}Sn_x$ alloys. Deformation potential theory has been widely studied to describe the relationship between strain and bandgap energy.

3.4.2.1 Deformation potential theory

The application of homogeneous strain in a solid produces changes in the lattice parameter and, in some cases, in the symmetry of the material. These in turn produce significant changes in the electronic band structure.[105] All configurations of homogeneous strain can be divided into two contributions: a hydrostatic component, which gives rise to a volume change without disturbing the crystal symmetry, and an anisotropic component, which reduces the symmetry present in the strain free lattice.

The strain dependence of electronic levels can be characterized by deformation potential, that is, the energy shift per unit strain, which is typically in the range from 1 to 10eV.

In this work, $Ge_{1-x}Sn_x$ layers were grown epitaxially on (001) GaAs substrates, so biaxial (001) in-plane strain was generated. The changes of the band structure under this type of strain are illustrated in Figure 3.12. For unstrained layers (a), the light-hole (LH) and heavy-hole (HH) bands are degenerate at the Brillouin zone center Γ, and the spin-split-off band lies lower in energy. As shown in Figure 3.12(b) and (c), strain has some important consequences on the band structure.

i. The hydrostatic component of strain changes the overall separation of the valence band and conduction band. Compressive hydrostatic strain increases this average bandgap energy, while tensile strain decreases this energy.
ii. The anisotropic component of strain splits the LH and HH apart at the Γ point. This splitting is proportional to the strain applied.
iii. The anisotropic component of strain introduces an anisotropic valence band structure, which changes the effective masses of LH and HH.

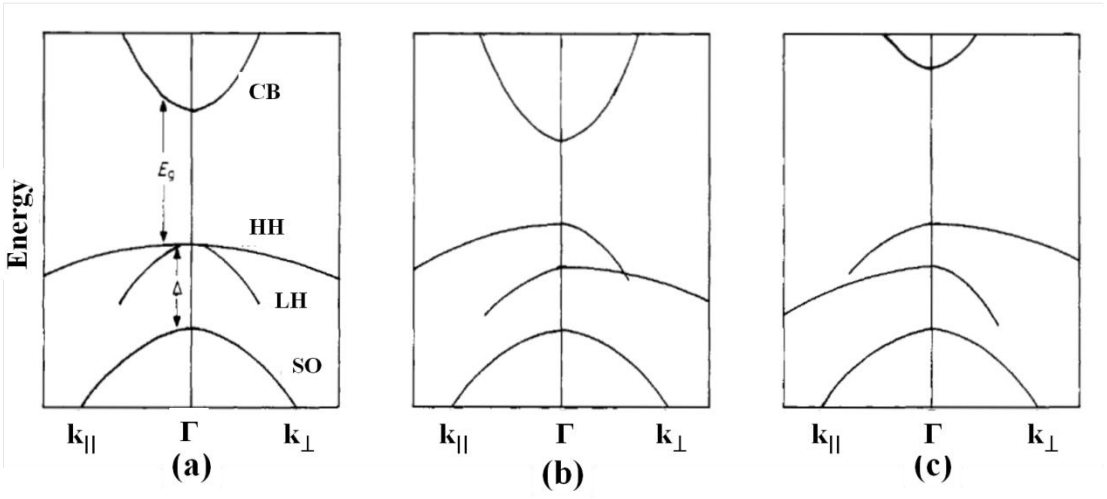

Figure 3.12 (a) Schematic representation of the band structure of an unstrained semiconductor. (b) Band structure under biaxial tension. (c) Band structure under

biaxial compression. Here $k_{//}$ is the k value in the plane of the layers, and $k_{\perp}$ is the value along the axis perpendicular to the layers. (After O'Reilly[106])

In order to explore the band structure of the conduction band and valence band near k=0 (Γ valley), the $\boldsymbol{k} \cdot \boldsymbol{p}$ perturbation approach is used. Detailed analysis can be found in Ref.105. Here we briefly summarize the results. The relationships between the direct band gaps from LH ($E_g^{\Gamma}(lh)$) and HH ($E_g^{\Gamma}(hh)$) to the bottom of conduction band in Γ valley, and the in-plane strain $\varepsilon_{\parallel}$ are given by[107-109]

$$E_g^{\Gamma}(lh) = E_g^{\Gamma}(0) + a(\varepsilon_{\perp} + 2\varepsilon_{\parallel}) - \frac{\delta E_{100}}{4} + \frac{\Delta_0}{2} - \frac{\sqrt{\Delta_0^2 + \Delta_0 \delta E_{100} + \frac{9(\delta E_{100})^2}{4}}}{2} \quad \text{Eq. 3-1}$$

$$E_g^{\Gamma}(hh) = E_g^{\Gamma}(0) + a(\varepsilon_{\perp} + 2\varepsilon_{\parallel}) + \frac{\delta E_{100}}{2} \quad \text{Eq. 3-2}$$

$$\delta E_{100} = 2b(\varepsilon_{\perp} - \varepsilon_{\parallel}) \quad \text{Eq. 3-3}$$

where $E_g^{\Gamma}(0)$ is the direct bandgap energy of an unstrained layer; $\varepsilon_{\perp}$ and $\varepsilon_{\parallel}$ are the out-of-plane and in-plane strain respectively, and Δ_0 is the split-off band transition energy of an unstrained layer. a is the dilational deformation potential constant, which describes the change in the overall separation of the valence and conduction bands; b is the shear deformation potential constant, which describes the energy splitting of LH and HH.

3.4.2.2 Determination of deformation potentials a and b for $Ge_{1-x}Sn_x$ alloys

Using deformation potential theory, the direct bandgap energies of $Ge_{1-x}Sn_x$ alloys under biaxial strain can be calculated with accurate values of deformation potentials a and b. In order to determine these two material parameters, biaxial strained $Ge_{1-x}Sn_x$ layers were grown with strain control and the LH and HH direct bandgap were measured by PR at room temperature.

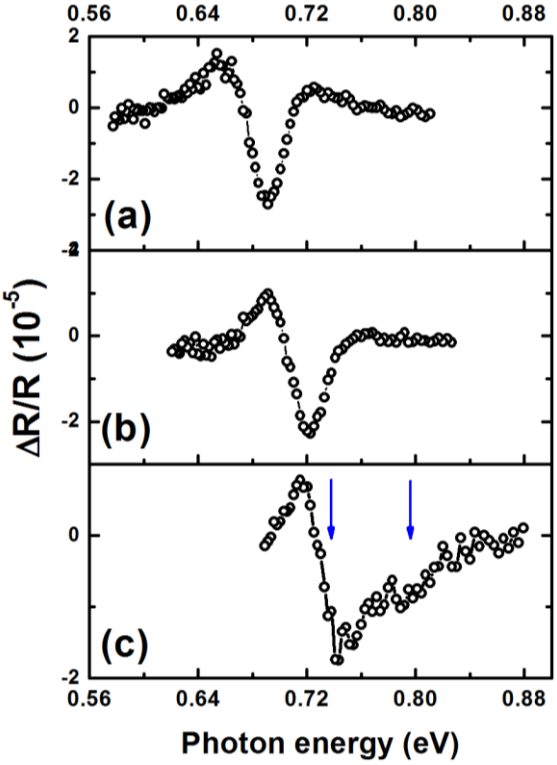

Figure 3.13 Room temperature of PR spectra of $Ge_{1-x}Sn_x$ samples (a) x=0.0265, strain=0.14%; (b) x=0.029, strain= -0.19%; (c) x=0.0306, strain= -0.513%.

Figure 3.13 shows the PR spectra of three $Ge_{1-x}Sn_x$ samples have similar Sn composition around 3%, but with different strains, from 0.5% compressive strain to 0.14% tensile strain. As the theory predicted, the overall direct band transition moves towards higher energy with increasing compressive strain. However, for small amounts of strain, the energy difference between the LH and HH transition is too small to be distinguished from the PR spectra. Another reason is the broadening of the PR features in $Ge_{1-x}Sn_x$ alloys, which limits the resolution in peak energy determination with multiple energy transitions.[49] Alloying Sn into Ge at low temperature has introduced many defects, which broadens the features and increases the broadening parameter obtained from the lineshape analysis from 7meV for Ge to around 30meV for $Ge_{1-x}Sn_x$ alloys. Due to this limiting factor, the applied strain has to be larger than 0.5% in order to distinguish the two adjacent transitions, as indicated by the arrows in Figure 3.13(c). About 0.5% compressive strain is used for this study

instead of tensile strain. The reason is that PR signals are too weak for samples with large amounts of tensile strain due to surface roughness and quality degradation.

Figure 3.14 shows the PR spectra for three $Ge_{1-x}Sn_x$ samples under biaxial compressive strain. The Sn compositions are (a) 6.32%, (b) 5.28%, and (c) 3.06%, respectively, and the strain levels are determined by XRD-RSM. Each PR spectrum consists of two transitions, which correspond to the transitions from light- and heavy-hole band to the bottom of Γ valley, because the compressive strain breaks the degeneracy, and the higher energy transition represents the LH band transition. Under a similar amount of strain, both transitions shift to lower energy with increasing Sn composition as expected. After lineshape fitting and modulus analysis, we obtained the LH and HH direct bandgap energies $E_g^{\Gamma}(lh)$ and $E_g^{\Gamma}(hh)$ respectively, as shown in Table 3.3. According to Eq. 3-1 to Eq. 3-3, the deformation potentials a and b for $Ge_{1-x}Sn_x$ alloy can be calculated. First of all, the direct bandgap energy of unstrained $Ge_{1-x}Sn_x$, $E_g^{\Gamma}(0)$, was calculated using the bowing parameter 2.42eV for each sample. Additionally, it is assumed that $Ge_{1-x}Sn_x$ alloys have the same split-off band transition energy Δ_0=0.289eV as Ge. The contribution from Δ_0 is very small because the fourth and fifth terms in Eq. 3-1 nearly cancel the effect of Δ_0. 20% change in Δ_0 only makes 1.5meV difference in the result. Finally, due to the small difference in Sn composition, we assume the deformation potentials are the same for the three $Ge_{1-x}Sn_x$ samples.

Table 3.3 Sn composition, strain and HH and LH transitions measured by PR and PL at room temperature. The lowest energy transition from PR measurement matches that from PL measurement for each sample.

	Sn (%)	**In-plane strain (%)**	**E_g^{Γ}(lh) (eV)**	**E_g^{Γ}(hh) (eV)**	**E_g^{Γ}(hh) from PL (eV)**
(a)	6.32%	-0.57%	0.683±0.005	0.618±0.002	0.614±0.005
(b)	5.28%	-0.594%	0.725±0.005	0.654±0.002	0.650±0.005
(c)	3.06%	-0.513%	0.795±0.008	0.732±0.002	0.730±0.005

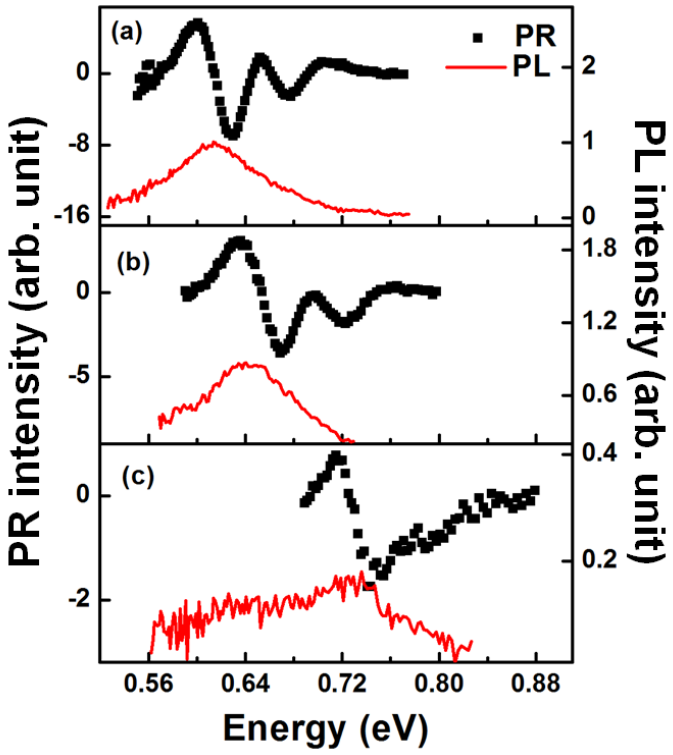

Figure 3.14 Room temperature PR spectra of compressive-strained $Ge_{1-x}Sn_x$ alloys and the red lines represent the PL spectra. (a) x=0.0632, strain = -0.57%. (b) x=0.0528, strain= -0.594%; (c) x=0.0306, strain= -0.513%;

In order to determine the average value of a and b, we used the same calculation method describe in Ref. 108. A Matlab code was written to randomly generate 2500 sets of E_g^{Γ}(lh)-E_g^{Γ}(hh) pairs within the measurement error bars for each sample to produce the values of a and b for each data set. The distributions of a and b are then plotted in Figure 3.15, and a Gaussian curve is used for fitting. The center and the FWHM of the Gaussian peak are set to be the average value and the error. Therefore, we obtain a= -11.04 ±1.41eV, and b= -4.07 ±0.91eV.

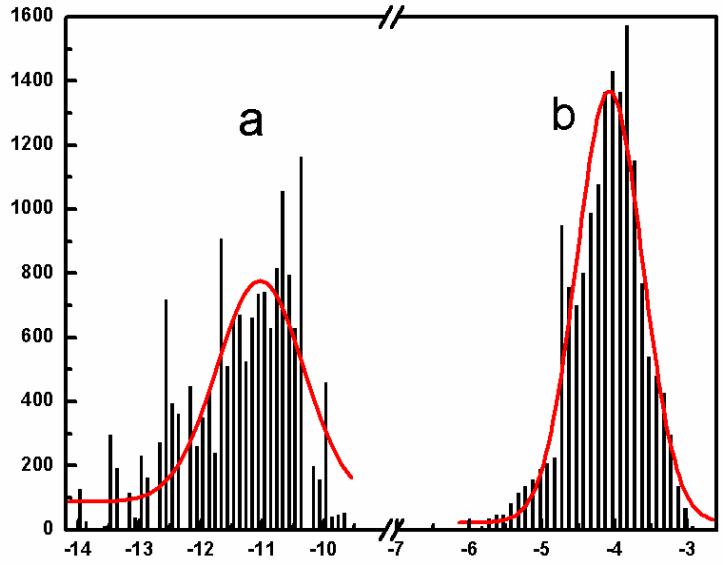

Figure 3.15 The values of a and b obtained from the data sets generated by the Matlab code.

The deformation potentials a and b are important material properties for $Ge_{1-x}Sn_x$ alloys. Since Sn compositions in the samples we studied are less than 7%, the values of a and b are compared with the values for Ge.[108] The value of a for $Ge_{1-x}Sn_x$ alloys is quite close to that of Ge, but b is 100% higher than the value -1.88eV for Ge. The shear deformation potential b primarily describes the splitting of the light- and heavy-hole band due to strain. However, in the calculation for Ge, the energy splitting is very small because the applied strain is less than 0.25%, which means the fitting of b is over a very small range. This limited range could result in such a difference.

So far, we have been able to use PR to measure the direct band transitions and determined the composition and strain dependence. In this study, 100nm thick $Ge_{1-x}Sn_x$ layers were used, thus the strain applied has to be small enough to avoid relaxation. That is why the highest strain is less than 0.6%. However, in order to calculate accurate bandgap energies, the thickness has to be 100nm or more. The reason is because the PR spectra are assumed in low-field regime for analysis, but this assumption is not valid for thinner layers. Figure 3.16 shows the PR spectrum of a 50nm $Ge_{1-x}Sn_x$ layer of x=0.0308 with strain of -0.516%. Franz-Keldysh oscillations

appear in the spectrum, indicating the sample is in an intermediate or high field regime. Higher electrical field is due to band bending over a shorter distance. In this regime, the PR data analysis is very complicated with no simplified equations.[92] Therefore, we choose thicker layers in our study.

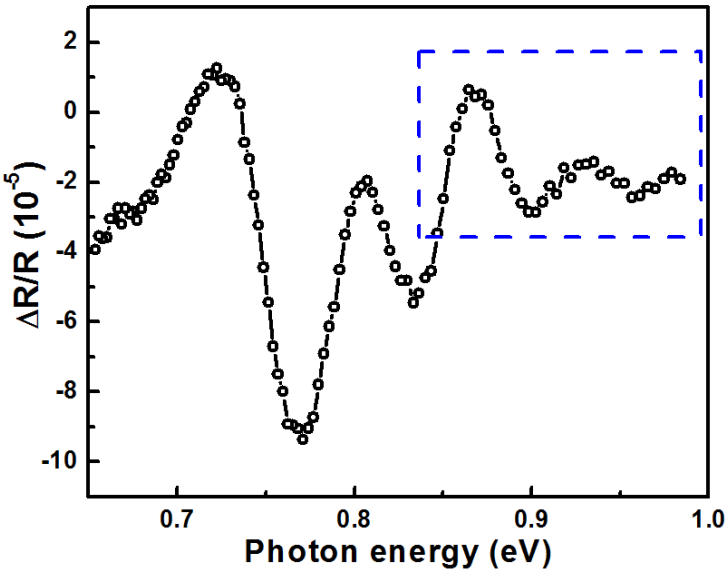

Figure 3.16 PR spectrum of 50nm $Ge_{1-x}Sn_x$ layer of x=0.0308 with strain of -0.516%, in which the Franz-Keldysh oscillations can be seen, as indicated in the blue box.

Room temperature PL measurements were performed for each strained sample as well, as shown by the red lines in Figure 3.14. Only the lowest energy direct transition can be detected by PL, because holes with higher energy will quickly scatter into the lowest energy valance band and then recombine. Unless the lowest band is filled, such as in a QW at low temperature, it is very difficult to detect higher energy transitions by PL. In addition, for samples with lower Sn compositions, the PL peak has a shoulder in the low energy region, which is contributed from the indirect band transition. Due to low emitting efficiency, the PL peak from the indirect transition is weaker than that from the direct transition, even though the indirect band is still lower in energy than the direct band. Gaussian peaks were used to deconvolve the PL spectra, and the peak energies of the direct transition were calculated. The direct bandgap energies

determined by PL, as listed in Table 3.3, match very well with the lowest energies determined by PR. More analysis of PL will be discussed in the following section.

3.4.3 Photoluminescence measurements at different temperatures

Photoluminescence was measured at different temperatures from 20K to room temperature. Figure 3.17 shows the smoothed PL spectra at different temperatures for the same $Ge_{1-x}Sn_x$ sample in Figure 3.14(c). At room temperature, the PL spectrum has a shoulder in the lower energy region of the direct transition peak, which is expected to be the indirect transition peak. As temperature decreases, this shoulder peak becomes stronger. On the other hand, the direct transition peak becomes weaker with decreasing temperature, and disappears at temperatures lower than 160K. The opposite trends of these two peaks can be explained as follows.

With only 3% Sn composition, the $Ge_{1-x}Sn_x$ alloy is still an indirect bandgap material. Due to the compressive strain, the separation between the direct and indirect bands becomes even larger. At room temperature, electrons have enough kinetic energy to be excited from the lowest energy band (the indirect band), to the direct band and then recombine. However, as temperature is reduced, fewer electrons can be excited to the direct valley, which greatly lowers the intensity of the direct peak. Finally, for temperatures lower than 160K, almost all electrons are confined in the indirect valley, which causes the disappearance of the direct peak. The enhancement of the indirect peak is due to the confinement of electrons in the indirect band and the reduced non-radiative recombination at low temperature.

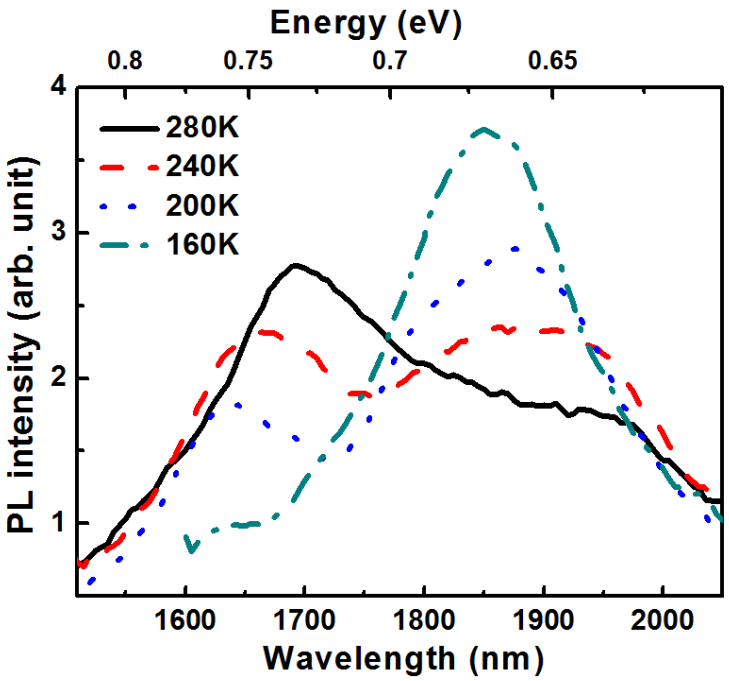

Figure 3.17 Smoothed PL spectra at different temperatures of $Ge_{1-x}Sn_x$ layer of x=0.0306 with the strain of -0.513%. Those two peaks in the PL spectra represent the direct and indirect transitions.

The PL spectra are deconvolved by two Gaussian peaks. Both peaks redshift with increasing temperature as predicted, and the peak positions in energy are plotted as a function of temperature in Figure 3.18. The Varshni model[110] can be used to describe the temperature dependence of bandgap energy, which is expressed as

$$E_g(T) = E_g(0) - \frac{\alpha T^2}{T + \beta} \qquad \text{Eq.3-4}$$

where the parameter α is the T→∞ limit of the gap entropy and β is expected to be comparable with the Debye temperature in a given material. The equation predicts a linear fit in the high temperature regime and a quadratic dependence in the low temperature regime both due to cumulative effects of lattice expansion and the electron-phonon contribution.

The direct transition dominates in the high temperature regime, so a linear line is used to fit the data. The slope of the fitting line is -3.06×10^{-4} eV/K. On the other hand, the change of the indirect transition PL peak with temperature is much slower. However the PL peak energy is not the indirect bandgap energy. Because a phonon is included in the indirect transition to conserve the momentum, the energy of a phonon has to be added or deducted. At this stage of our research, we do not have enough information of phonon energy, so we are not able to accurately calculate the correct indirect bandgap, but will be close to the measured PL peak plus or minus 35meV, the phonon energy in Ge.

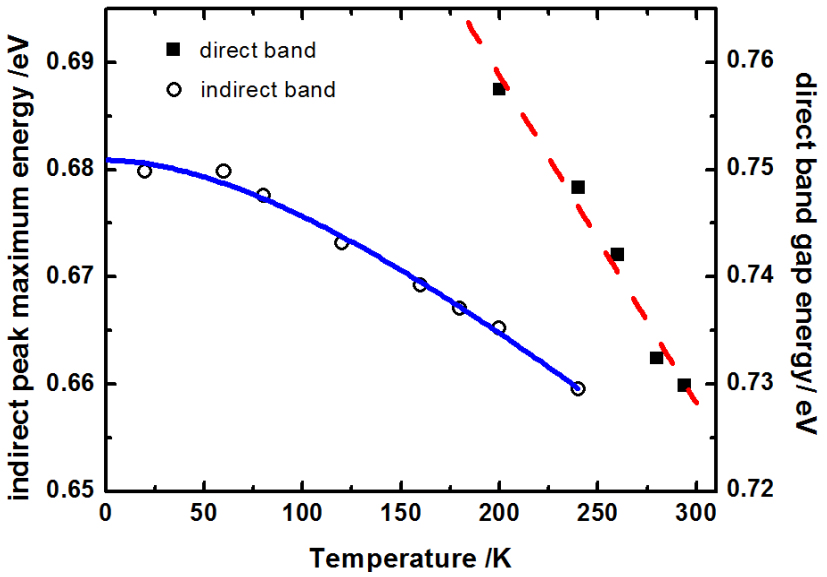

Figure 3.18 The PL peak energy change with temperature for the direct and indirect transitions.

When either compressive strain is reduced or the Sn composition is increased, the energy difference between the indirect and direct bands shrinks. Due to the Fermi distribution, more electrons will occupy the direct band, which in turn increases the intensity of the (fast) direct transition PL peak. Therefore, these two PL peaks get closer and the direct transition becomes increasingly dominant. Also, due to the smaller energy difference between the direct and indirect bands, the direct transition peak can exist at temperatures lower than 160K.

When the Sn composition is high enough, the $Ge_{1-x}Sn_x$ alloy becomes a direct bandgap material. Figure 3.19 shows the PL spectra of strain-free $Ge_{1-x}Sn_x$ with x=0.0642 at different temperatures. Only the direct transition peaks can be seen in the PL spectra, and the peak redshifts linearly with temperature at a rate of -3.07×10^{-4} eV/K, which is consistent with the rate determined in the previous lower Sn case. However, the intensity of the direct transition peak increases with decreasing temperature. This trend is opposite to the previous case, which indicates that the material is either direct band gap or very nearly direct band gap semiconductor. Because as temperature decreases, carriers are more confined in the lowest energy band, the enhancement of the direct transition PL peak shows that the direct band is the lowest energy band. Unfortunately we don't currently have a good method to determine the indirect bandgap energy accurately, so the indirect to direct transition point is estimated to be around 6-7% Sn. This experimental result is consistent with recent theoretical predictions.[49, 51, 57]

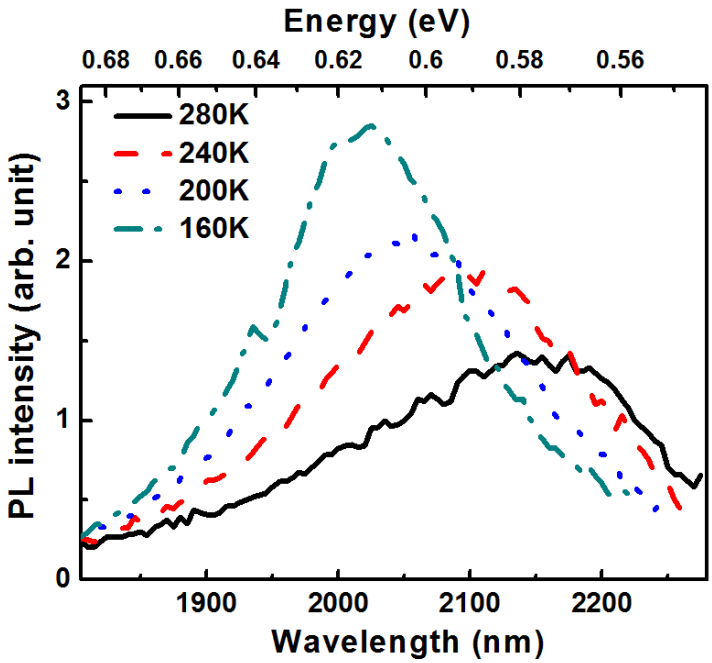

Figure 3.19 PL spectra of an unstrained $Ge_{1-x}Sn_x$ sample with x=0.0642 at different temperatures.

3.4.4 Summary of the optical properties

The optical properties of $Ge_{1-x}Sn_x$ alloys are characterized by PR and PL, and three important material parameters have been determined from samples with up to x=0.064 and -0.6% strain. They are the bowing parameter b^{GeSn} describing the composition dependence, and two deformation potentials describing the strain dependence of the direct bandgap. The deformation potentials are assumed to be the same for both compressive and tensile strain in a small range of strain. Using these three parameters, we have the ability to calculate the direct bandgap energies of $Ge_{1-x}Sn_x$ alloys with combined effect of composition and strain. Temperature dependence of the bandgap energies has been investigated as well.

For example, Figure 3.20 plots the lowest direct bandgap energy of $Ge_{1-x}Sn_x$ alloys with different Sn compositions and different amounts of tensile strain at room temperature. From previous discussion, we have learned that the indirect to direct bandgap transition for pure Ge is expected to be at 1.7% tensile strain, and for unstrained $Ge_{1-x}Sn_x$ alloys the crossover point is around 6.5% Sn. Therefore, a line can be drawn connecting these two points as the blue dashed line in Figure 3.20. To a first order approximation, this line represents the transition line for $Ge_{1-x}Sn_x$ alloys to become direct bandgap with combined effects of strain and Sn alloying. Less strain is needed for $Ge_{1-x}Sn_x$ samples with higher Sn composition, and lower Sn composition is needed for samples with higher strain.

The HH and LH energies of compressive-strained $Ge_{1-x}Sn_x$ alloys can be calculated as well. Compressive strain has been widely used in QW laser structures to reduce the threshold current density. Therefore, the ability to determine the band gap under compressive strain is very important for future device designs.

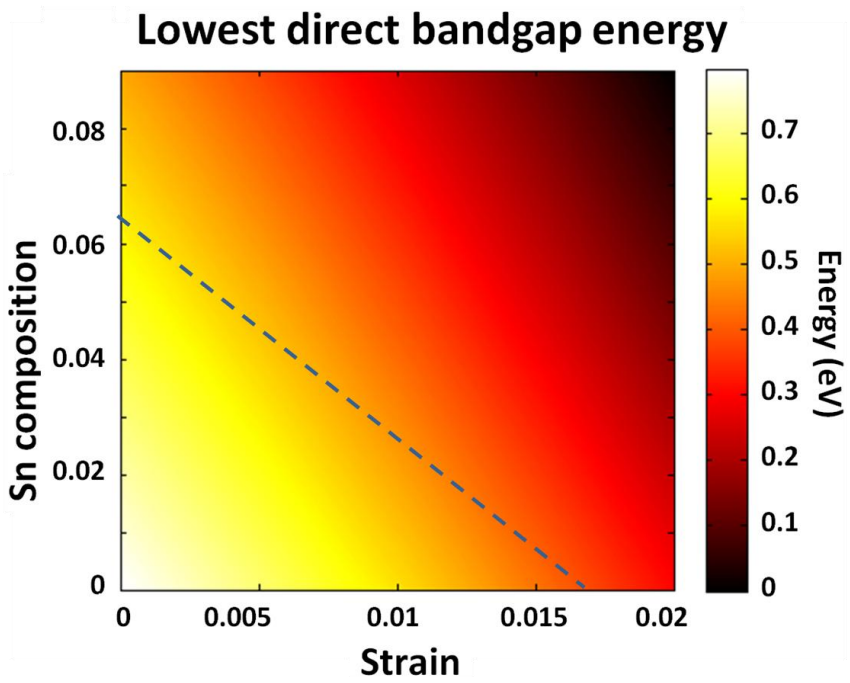

Figure 3.20 The map of the lowest direct bandgap energy of $Ge_{1-x}Sn_x$ alloys with different Sn compositions and different amounts of biaxial tensile strain. The dash line represents the transition from indirect to direct bandgap material.

3.5 Raman study

From the previous discussion, we know that the optical properties of $Ge_{1-x}Sn_x$ alloys depend on both Sn composition x and in-plane strain $\varepsilon_{\parallel}$ of the layer. Therefore, the ability to monitor the composition and strain is of crucial importance in order to engineer the optical properties of devices based on $Ge_{1-x}Sn_x$ alloys. Raman spectroscopy is a powerful technique for this purpose because the optical phonon modes of the alloys are strongly affected by x and $\varepsilon_{\parallel}$. Compared to XRD-RSM, Raman is applicable to much thinner films without appreciable loss in signal-to-noise ratio.

Raman spectroscopy has been widely used to quantify the strain in ultra-thin strained Si[111] and strained Ge[112-113]. In measuring strain, attention is given to the shift

$\Delta\omega$ of the optical phonon modes away from their values in the bulk material. The Raman frequency shift $\Delta\omega$ is related to the amount of strain, which can be modeled by phonon deformation potential theory.[109]

In Si (Ge), only Si-Si (Ge-Ge) LO mode is observed in Raman spectra. For alloys, such as SiGe, there are three Raman peaks corresponding to Si-Si, Ge-Ge, and Si-Ge LO modes. All three modes are affected by both strain and composition. [114-115] In order to study these two effects, strain and composition should be controlled separately, which is achieved by using buffer layers as virtual substrates.

Raman spectra of $Ge_{1-x}Sn_x$ alloys are similar to those of SiGe alloys. The composition dependence of the Raman frequency of $Ge_{1-x}Sn_x$ alloys was published. However without proper virtual substrates to separate the composition and strain contributions, researchers had to exclude the strain effect by an empirical equation using coefficients for Ge, or they just assumed that the $Ge_{1-x}Sn_x$ layers were fully relaxed.[116-118] Thus prior work provided little information about the Raman peak shift with strain for $Ge_{1-x}Sn_x$ alloys. In this work, using InGaAs buffer layers, we controlled the strain and composition of $Ge_{1-x}Sn_x$ alloys separately, which decouples these two contributions to Raman peak shifts.[119]

3.5.1 Strain effect

A series of $Ge_{1-x}Sn_x$ samples with 20-30nm thickness with different combinations of strain and composition were grown on InGaAs buffer layers. XRD-RSMs were measured for each sample to determine the values of strain and composition. Raman measurements were preformed for the same series of samples. In order to avoid thermal expansion which might affect the data, we close the slit in front of the laser to reduce the power to the critical point where no Raman signal can be detected with lower power.

Figure 3.21 shows the normalized Raman spectra of five $Ge_{1-x}Sn_x$ samples of x=0.047±0.004 with different levels of strain, and for reference, a bulk Ge (001) wafer. The strains measured by XRD are listed in Table 3.4. The Ge wafer Raman spectrum consists of one strong Ge-Ge longitudinal optical (LO) Raman peak at ω_{Ge}=300cm^{-1}. The Raman spectra of $Ge_{1-x}Sn_x$ also consist of only one strong peak near 300cm^{-1}, which is assigned to the Ge-Ge LO peak. A Sn-Sn peak could not be found in the spectra due to the small amount of Sn. A Ge-Sn peak cannot be detected in our spectra either because the low composition of Sn and the laser wavelength of 532nm is far from the resonance condition for this peak[117]. Although highly tensile strained samples have rougher surfaces, the bulk layers are not relaxed, so applicable for Raman study. As shown in Figure 3.22, even for the highest strained sample, the $Ge_{1-x}Sn_x$ XRD peak (peak 4) still aligns vertically on top the peak (peak 3) from the top InGaAs buffer layer.

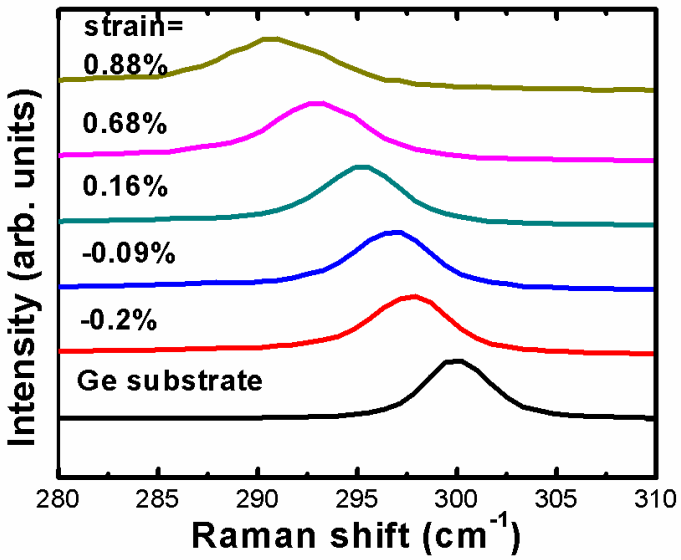

Figure 3.21 Raman spectra from a bulk Ge (001) substrate and $Ge_{1-x}Sn_x$ samples of x=0.047±0.004 with different levels of strain.

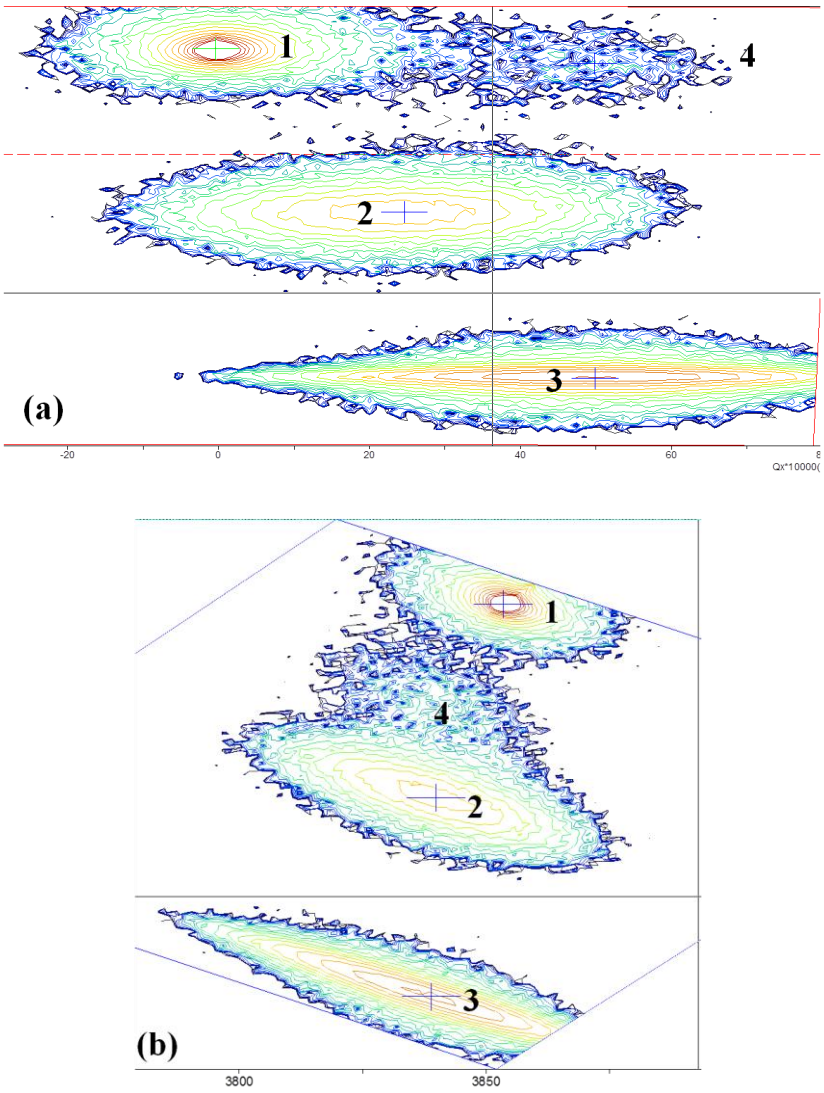

Figure 3.22 XRD-RSMs of a $Ge_{1-x}Sn_x$ sample of x=0.047±0.004 with 0.88% tensile strain. (a) (004) symmetric scan, (b) (224) asymmetric scan. The tilting angles for two InGaAs buffer layers are different, which add complexity to interpret the (224) map.

In addition, although the biaxial strain splits the triply degenerate optical phonon mode at the Brillouin zone center into a singlet and a doublet, in backscattering geometry with [001] growth direction, only the singlet can be observed, and it corresponds to the vibration in the (001) plane.[111] The Raman peaks from InGaAs buffer layers are below 291cm^{-1}, and do not overlap with those of GeSn alloys. Also since the Raman measurement is quite surface sensitive, 20nm thick GeSn layers are

thick enough to absorb most of the laser intensity and block any Raman signal from below. Therefore, we do not need to consider the InGaAs buffer contribution to the Raman peaks of $Ge_{1-x}Sn_x$ alloys.

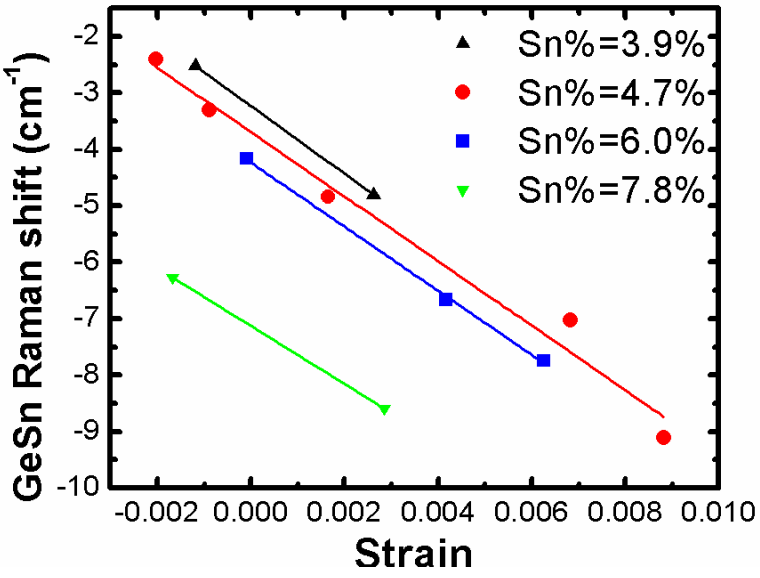

Figure 3.23 Measured Raman frequency shifts of the Ge-Ge LO mode of $Ge_{1-x}Sn_x$ samples as a function of strain for different Sn compositions. The solid lines are linear fits to the experimental data.

Table 3.4 Summary of strain and Raman data for $Ge_{1-x}Sn_x$ alloys with x=0.047±0.004.

In composition in InGaAs buffer layer	**Strain percentage of $Ge_{1-x}Sn_x$ layers**	**Raman shift with respect to Ge (cm^{-1})**	**FWHM of the Raman peak(cm^{-1})**
0.12	-0.20%	-2.34±0.03	4.92
0.15	-0.09%	-3.31±0.03	4.99
0.18	0.16%	-4.84±0.03	5.11
0.25	0.68%	-7.02±0.04	6.07
0.30	0.88%	-9.12±0.07	7.95

As shown in Figure 3.21, the Ge-Ge LO peak in $Ge_{1-x}Sn_x$ alloys progressively shifts toward lower energy and broadens with increasing strain. This Raman frequency shift Δω is defined as the difference in peak position between the $Ge_{1-x}Sn_x$ layer and the bulk Ge wafer:

$$\Delta\omega = \omega_{GeSn} - \omega_{Ge} \quad \text{Eq.3-5}$$

The values of Δω are listed in Table 3.4.The same Δω data is plotted with respect to stain as red dots in Figure 3.23. In theory, both composition and strain alter the Raman peak, so the measured shift of Ge-Ge LO peak can be expressed as

$$\Delta\omega = \Delta\omega_{alloy} + \Delta\omega_{strain} \quad \text{Eq.3-6}$$

where $\Delta\omega_{alloy}$ and $\Delta\omega_{strain}$ represent the contribution from composition and strain respectively. $\Delta\omega_{alloy}$ depends on Sn composition, so it is a constant number in this case. For biaxial strain, the magnitude of $\Delta\omega_{strain}$ depends linearly on the in-plane strain $\varepsilon_{||}$ following the relationship

$$\Delta\omega_{strain} = \frac{1}{\omega_0}\left(q - p\frac{C_{12}}{C_{11}}\right)\varepsilon_{||} = b\varepsilon_{||} \quad \text{Eq.3-7}$$

where ω_0 is the unstrained Raman frequency of a $Ge_{1-x}Sn_x$ alloy with the same Sn composition, C_{11} and C_{12} are elastic constants, and p and q are phonon deformation parameters.[116-117] The coefficient b depends on Sn composition, thus is a constant in this case as well. Therefore we can fit the data using a linear equation. The slope of the linear fit is the b value, and the unstrained Raman frequency shift can be determined by the intercept of the line to ε=0. Accordingly, we obtained the value b=-(571±45)cm^{-1} for the Sn composition x=0.047. In order to verify the value of b, XRD and Raman spectra of another three sets of strained $Ge_{1-x}Sn_x$ samples with different Sn compositions from x=0.039 to 0.078 were measured. The Raman frequency shifts Δω with respect to strain are also shown in Figure 3.23. After linear fitting, the fitted lines are almost parallel each other, and parallel to the one for x=0.047 discussed above. The average value of the slope b is equal to –(563±34)cm^{-1}. Although the value of b is dependent on the material properties of $Ge_{1-x}Sn_x$ alloys and thus the Sn composition, as shown in Eq.3-7, we don't have enough data for p, q, C_{11} and C_{12} to perform the

analysis. In addition, the difference in Sn composition is small, so we can reasonably ignore the composition dependence for materials in the range of interest for photonic devices. To further prove our assumption that constant b is valid, we compare the data in another group IV binary alloy SiGe. The phonon strain-shift coefficient b for the Si-Si and Ge-Ge LO peak is nearly constant throughout the entire composition range of SiGe alloys.[115] Therefore, we assume a similar behavior in strained $Ge_{1-x}Sn_x$ alloys, and use the average value of b for samples of all compositions.

3.5.2 Composition effect

Besides strain, Raman peaks are also affected by composition. As shown in Figure 3.24, the Raman peak of Ge-Ge LO mode in fully relaxed $Ge_{1-x}Sn_x$ alloys shifts to lower wavenumbers as Sn composition increases. We plotted the Raman frequency shifts $\Delta\omega_{alloy}$ with respect to Sn composition in Figure 3.25. The strain contribution $\Delta\omega_{strain}$ has been deducted from the total Raman shift using Eq.3-6, Eq.3-7, and the calculated b value. In addition to the samples shown in Figure 3.21 and Figure 3.24, we also did the calculation for other samples with different Sn compositions, but with only one strain-state. The highest Sn composition we achieved is around 12%. The magnitude of $\Delta\omega_{alloy}$ depends linearly on the Sn composition x following the relationship

$$\Delta\omega_{alloy} = \omega_0 - \omega_{Ge} = ax \qquad \text{Eq.3-8}$$

After a linear fitting, the value of a is determined to be -(82 ±4) cm^{-1}.This value is close to the value a= -(75.4 ±4.5)cm^{-1} obtained by V.R.D'Costa, who used almost relaxed $Ge_{1-x}Sn_x$ alloys.[117]

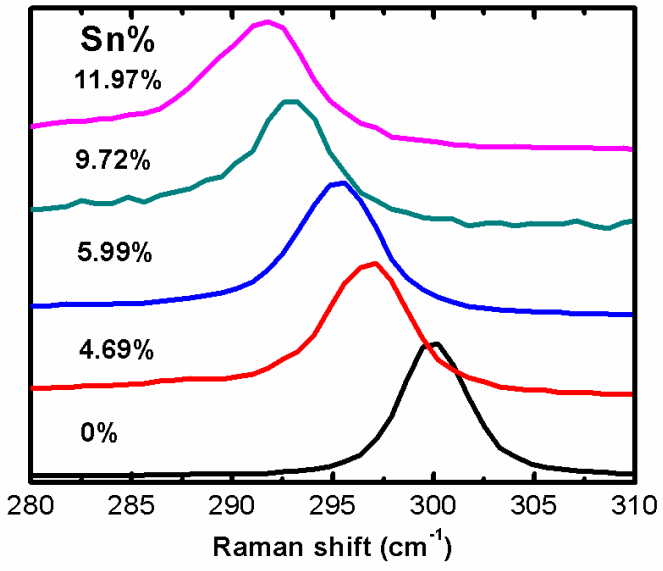

Figure 3.24 Raman spectra from a bulk Ge(001) substrate and fully relaxed $Ge_{1-x}Sn_x$ samples of different Sn compositions.

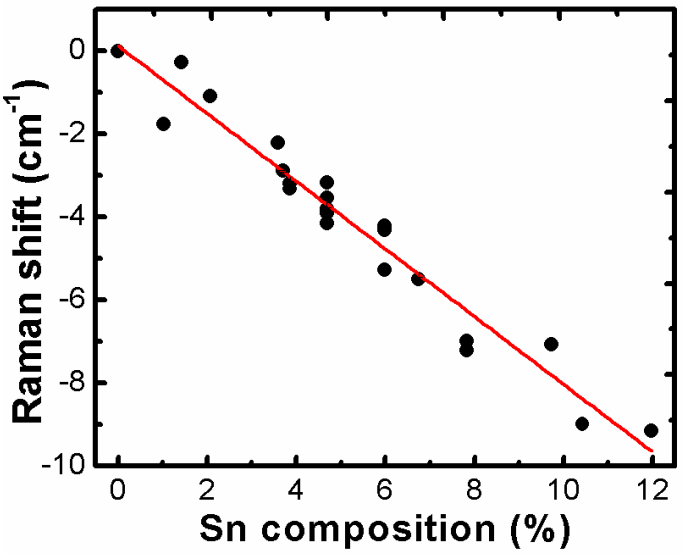

Figure 3.25 Composition dependence of Raman shift for the Ge-Ge LO mode after correcting the strain contribution. The solid line is a linear fit to the data.

Besides the peak position shift, the Raman peaks broaden with higher Sn composition and larger strain, which is due to degradation of the quality of the Ge_{1-}

$_xSn_x$ layer as strain and Sn composition increase. All LO phonon peaks were found to be asymmetric with a half width at half maximum intensity that is larger on the low energy side than on the high energy side. Similar asymmetric broadening has been observed in $Ge_{1-x}Sn_x$ alloys in other papers and is attributed to compositional fluctuations and local disorder.[116, 118]

3.6 Conclusion

Good crystalline quality $Ge_{1-x}Sn_x$ layers were grown by MBE on InGaAs buffer layers on GaAs substrates. Low growth temperature (200°C) is essential to suppress Sn precipitation. Consistent composition results were obtained from three different methods, and the highest Sn composition achieved was 10.5%. XRD and TEM were used to confirm the crystalline quality. The direct bandgap energies of $Ge_{1-x}Sn_x$ alloys were determined by PR and PL.

Using InGaAs buffer layers as virtual substrates allows separate control of strain and composition of $Ge_{1-x}Sn_x$ layers, thus provides us the ability to decouple these two effects on the material properties. From unstrained samples, the bowing parameter of direct bandgap b^{GeSn} was calculated to be 2.42 ± 0.04eV, which describes the composition dependence. Deformation potential theory was used to study the strain dependence, and the dilational deformation potential a and shear deformation potential b were calculated to be -11.04 ± 1.41eV and -4.07 ± 0.91eV, respectively. With these three material parameters, the direct bandgap energies of $Ge_{1-x}Sn_x$ alloys of different combinations of composition and strain can be calculated easily. This is very important for design of optoelectronic devices.

In addition, the strain and composition contributions to the Raman shift of $Ge_{1-x}Sn_x$ alloys were quantified separately. The Raman frequency shift of Ge-Ge LO mode was determined to be $\Delta\omega = -563\varepsilon_{||} - 82x$. This result shows that Raman can be

used to accurately determine the strain and composition of $Ge_{1-x}Sn_x$ alloys, especially for thin films, with the advantage of being surface sensitive and nondestructive.

CHAPTER 4 $Si_xGe_{1-x-y}Sn_y$ alloy

$Si_xGe_{1-x-y}Sn_y$ alloys are CMOS compatible materials. One of the proposed applications for $Si_xGe_{1-x-y}Sn_y$ alloys is as the barrier layer for $Ge_{1-x}Sn_x$ quantum wells. As ternary alloys, $Si_xGe_{1-x-y}Sn_y$ alloys enable the independent control of bandgap energy and lattice constant, which leads to one more degree of freedom in the design of strained QW structures.[73-74] However, due to challenges in the growth, most of the material properties of these alloys are still unknown. Simulations of devices with $Si_xGe_{1-x-y}Sn_y$ alloys are based on theoretical predictions, which are subject to correction by experimental data.

4.1 Crystal growth and structural characterization

In this work, $Si_xGe_{1-x-y}Sn_y$ alloys were again grown on InGaAs buffer layers by MBE to control the degree of strain. The main challenge in growing $Si_xGe_{1-x-y}Sn_y$ alloys is still the Sn segregation tendency at high temperatures. This is a significant challenge as the nominal growth temperature for Si is several hundred degrees higher than for Ge. Figure 4.1(a) shows the top view SEM image of one $Si_xGe_{1-x-y}Sn_y$ sample grown at 300°C, in which precipitates of the size of $1\times1\mu m^2$ can be seen. Auger measurements were performed on precipitate and smooth areas as shown in Figure 4.1(b). The Sn element signal is much stronger on the precipitate than the smooth area, while the Ge element signal is much lower on the precipitate. The Auger spectra confirm that Sn segregates on surface at 300°C growth temperature.

In order to suppress Sn segregation, samples were grown at a lower temperature of 200°C. A smooth surfaces were achieved for samples with low Sn composition. Figure 4.2(a) shows a $5\times5\mu m^2$ AFM image of $Si_xGe_{1-x-y}Sn_y$ sample with $y\approx0.07$, and the RMS roughness is about 0.5nm. However, when the Sn composition is higher than

~7%, the surface is rough with small precipitates again, as shown in Figure 4.2(b). It appears that the incorporation of Sn is even more difficult in SiGe alloys than Ge, which might be due to larger lattice mismatch. A lower temperature (150°C) was used to grow samples with Sn composition higher than 7%. The small precipitates disappear and the RMS roughness drops back to 0.6nm for a $5 \times 5 \mu m^2$ area.

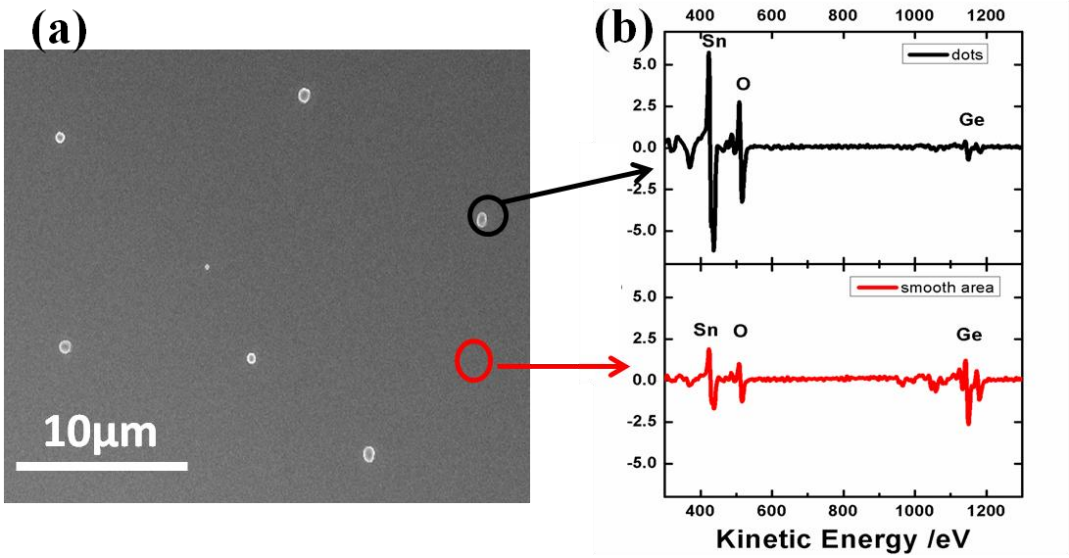

Figure 4.1 (a) SEM top view image of $Si_xGe_{1-x-y}Sn_y$ sample grown at 300°C by MBE, in which Sn precipitates can be seen on the surface. (b) Auger spectra of the areas with and without Sn precipitate.

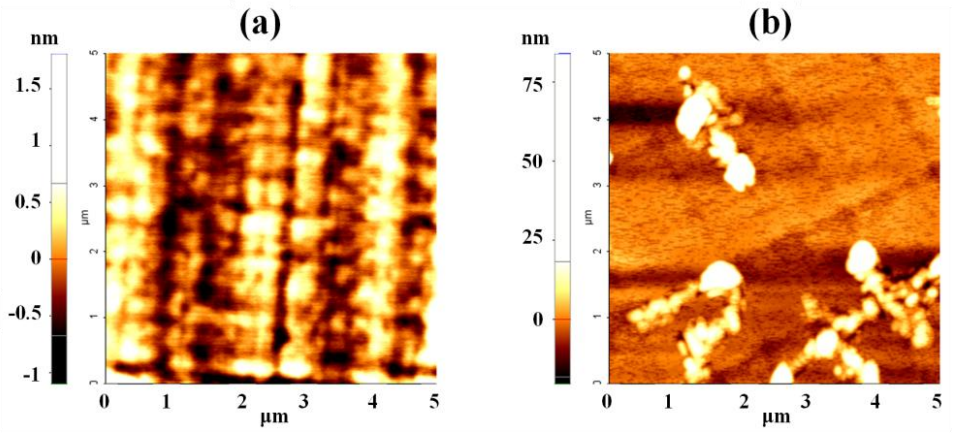

Figure 4.2 AFM images of $Si_xGe_{1-x-y}Sn_y$ samples grown at 200°C with (a) y≈0.07; (b) y≈0.08.

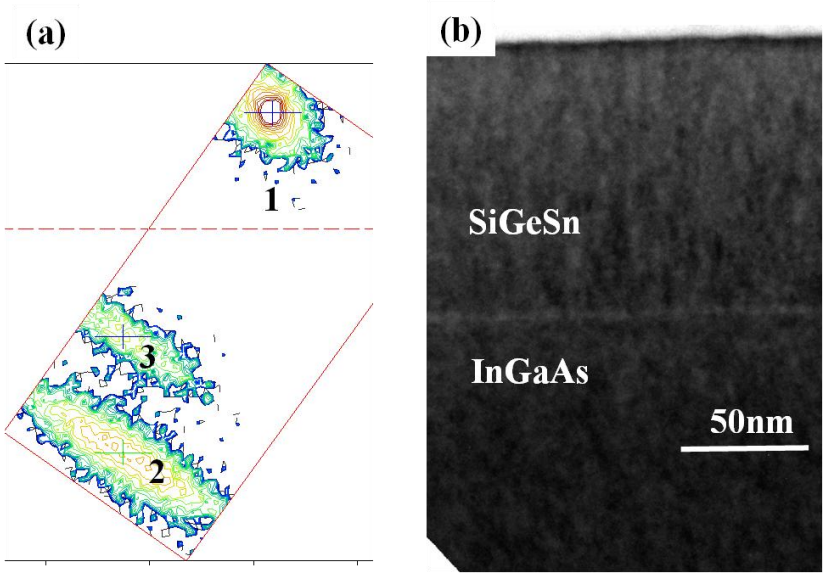

Figure 4.3 (a) (224) XRD-RSM of a $Si_xGe_{1-x-y}Sn_y$ (001) sample grown at 150°C with x=0.064 and y=0.088. (b) TEM cross-section image of the as-grown sample.

XRD-RSMs and TEM were performed to characterize crystalline quality of the samples grown at low temperature. Figure 4.3(a) shows the (224) XRD-RSM of a $Si_xGe_{1-x-y}Sn_y$ sample grown at 150°C with x=0.064 and y=0.088. The $Si_xGe_{1-x-y}Sn_y$ layer diffraction peak (peak 3) aligns vertically with the InGaAs buffer layer peak

(peak 2), indicating a coherent growth. The in-plane and out-of plane lattice constants of the $Si_xGe_{1-x-y}Sn_y$ layer were determined. The TEM cross-section image of the sample is shown in Figure 4.3(b), from which no visible Sn precipitates and no visible threading dislocations can be observed inside the layer.

The compositions of $Si_xGe_{1-x-y}Sn_y$ layers were determined by XPS, and the results are listed in

Table 4.1. Because of the low Sn and Si compositions, the XPS signal for Si and Sn elements are noisy, as shown in Figure 2.13, which gives an error of ±0.005 for composition determination. From the composition, the unstrained lattice constant can be calculated using Vegard's Law,

$$a(Si_xGe_{1-x-y}Sn_y) = xa_{Si} + (1-x-y)a_{Ge} + ya_{Sn} \quad \text{Eq.4-1}$$

On the other hand, in-plane and out-of-plane lattice constants of $Si_xGe_{1-x-y}Sn_y$ layers were measured by XRD-RSM. The unstrained lattice constants were calculated by correcting the slight strain, assuming $Si_xGe_{1-x-y}Sn_y$ has similar elastic constants to Ge, thus $\varepsilon_\perp = -\varepsilon_\parallel/1.33$. The results are also listed in

Table 4.1. By comparison, we found that the unstrained lattice constants calculated from XRD-RSM are consistent with the values obtained from XPS. This agreement confirms that Vegard's law is a very good approximation for $Si_xGe_{1-x-y}Sn_y$ alloys within the composition range studied.

Table 4.1 Measured $Si_xGe_{1-x-y}Sn_y$ composition by XPS and in-plane and out-of plane lattice constants by XRD. These two methods gave consistent unstrained lattice constants.

XPS			XRD		
Si	Sn	Unstrained lattice constant (Å)	In-plane lattice constant (Å)	Out-of-plane lattice constant (Å)	Unstrained lattice constant (Å)
0.055	0.059	5.694	5.697	5.693	5.695
0.098	0.058	5.683	5.691	5.676	5.682
0.084	0.073	5.699	5.700	5.698	5.699
0.059	0.052	5.687	5.674	5.692	5.685
0.064	0.088	5.716	5.709	5.711	5.710

4.1.1 Rapid thermal annealing

Although from TEM cross-section images we can't see any dislocations and Sn precipitates in $Si_xGe_{1-x-y}Sn_y$ samples, the as-grown samples don't have good optical qualities. No PR signals could be detected at room temperature. Therefore, post-growth anneal was performed to the samples to improve the crystalline quality of material grown at such a low temperature. Rapid thermal annealing under forming gas ambient was used in this study.

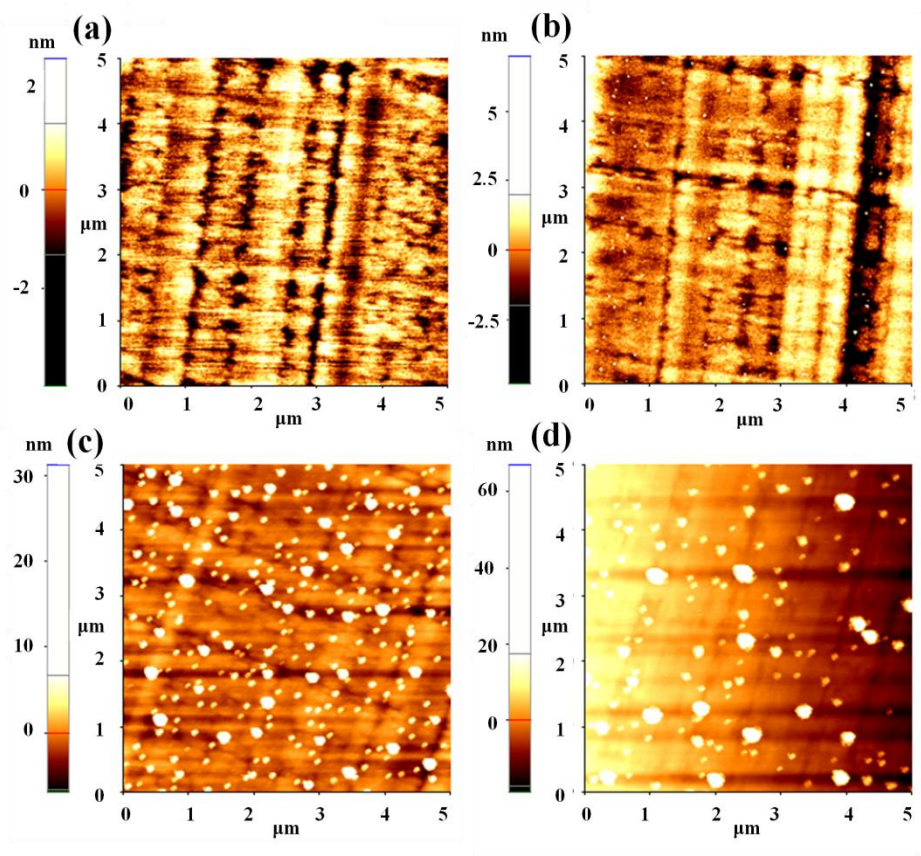

Figure 4.4 $5\times5\mu m^2$ AFM images of a $Si_xGe_{1-x-y}Sn_y$ sample annealed for different temperatures and times. (a) RTA 500°C for 30s. RMS=0.7nm (b) RTA 500°C for 120s. RMS=1.0nm (c) RTA 600°C for 30s. (d) RTA 650°C for 30s.

It is very important to limit the thermal budget during annealing to avoid Sn segregation. Figure 4.4 shows the $5\times5\mu m^2$ AFM images of a $Si_xGe_{1-x-y}Sn_y$ sample annealed with different recipes. If samples were annealed at 600°C or 650°C for 30s, the quality of the sample degrades, and the surface becomes very rough with large Sn precipitates. The higher the temperature and the longer the time, the larger the precipitates. If the annealing temperature is 500°C or lower, the surface stays smooth after 30s anneal as shown in Figure 4.4(a), and the RMS surface roughness is 0.7nm. Also, at 500°C samples can be annealed up to 120s with RMS=1.0nm as shown in Figure 4.4(b). However we noticed that there are very small precipitates appearing on the surface. Fortunately, these tiny precipitates on surface do not affect the bulk

properties. A TEM cross-section image of a 120s annealed $Si_xGe_{1-x-y}Sn_y$ sample with x=0.098 and y=0.058 is shown in Figure 4.5. There are no visible precipitates or threading dislocation inside the layer. The composition of the annealed sample is consistent with that of the as-grown sample, and the difference is within the measurement error of XPS. These results suggest that the tiny surface precipitates only affect the surface morphology, but do not cause compositional degradation of the bulk material.

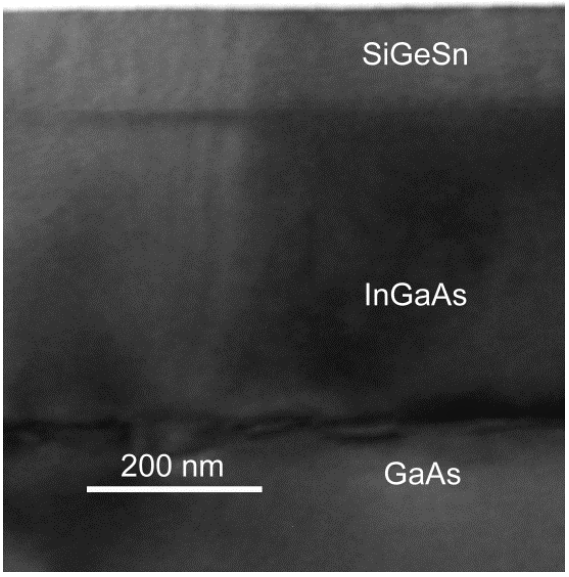

Figure 4.5 TEM cross-section image of a $Si_{0.098}Ge_{0.844}Sn_{0.058}$ sample after 120s RTA at 500°C. No visible precipitates or threading dislocations are seen.

The optical properties of annealed samples were further characterized by PR. The PR spectra of a sample annealed at 500°C for 30s and 120s are plotted in Figure 4.6. Under similar experimental conditions, both annealed samples show the same transition energy for the direct bandgap, which confirms the constant composition after anneal. But the signal-to-noise ratio is much better for the longer annealed sample. Therefore, for the purpose of the PR measurement, $Si_xGe_{1-x-y}Sn_y$ samples were RTA annealed at 500°C for 120s.

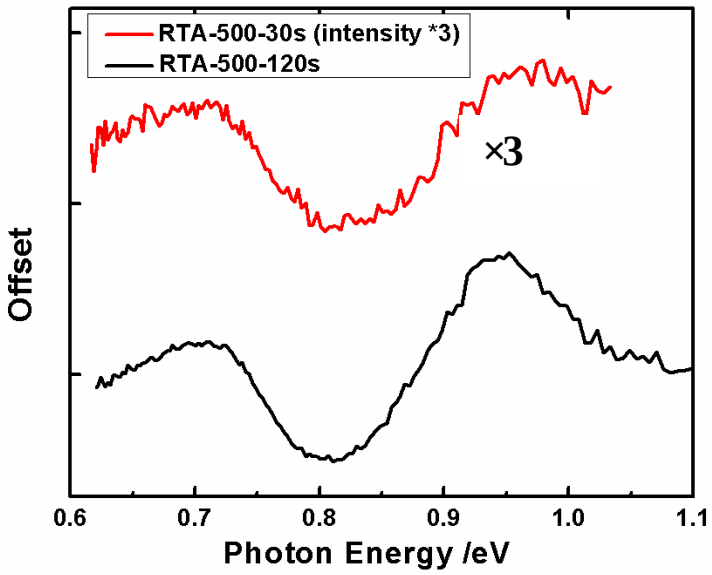

Figure 4.6 PR spectra of a $Si_xGe_{1-x-y}Sn_y$ sample annealed at 500°C for 30s and 120s. The direct bandgap transitions have the same energy, but longer annealed sample has a better signal-to-noise ratio.

4.2 Optical characterization

4.2.1 Decoupling of band gap and lattice constant

Direct bandgap energies of $Si_xGe_{1-x-y}Sn_y$ samples were determined by PR at room temperature. Figure 4.7(a) shows PR spectra of unstrained $Si_xGe_{1-x-y}Sn_y$ samples in the vicinity of the direct band gap. These samples have similar Sn/Ge ratios around 0.069, and the Si composition values from 0% to 10%. The transition moves to higher energy values as the Si composition increases.

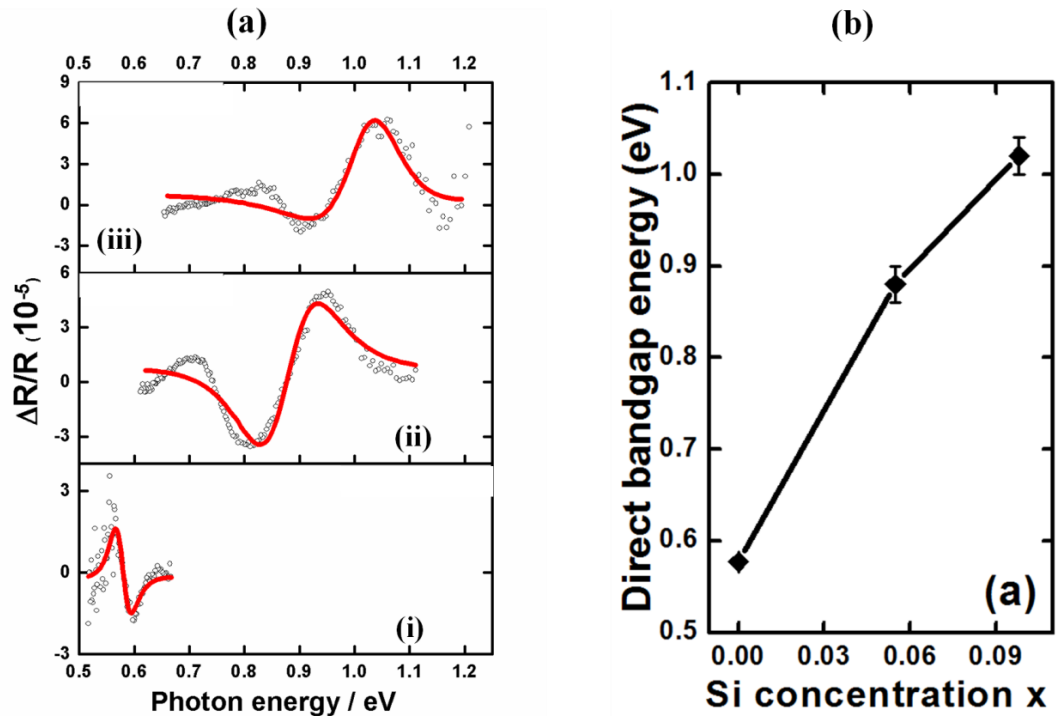

Figure 4.7 Room-temperature PR spectra of unstrained $Si_xGe_{1-x-y}Sn_y$ samples with a fixed Sn/Ge ratio about 0.069, but different Si compositions: (i) Si=0%, (ii) Si=5.5%, (iii) Si=9.8%. The solid red lines are fitting curves for PR spectra. Sample (i) is an as grown sample and sample (ii) and (iii) are RTA annealed for 120s at 500°C.

Line shape analysis is used to calculate the direct bandgap energy, and the red lines are the fitting curves. The modulus analysis of PR spectra also provides consistent results. The direct bandgap energies of the samples are plotted as a function of Si composition in Figure 4.7(b). The bandgap energy increases monotonically with Si composition, as predicted by theory. However, we notice that there is a deviation between the PR spectrum and fitting lines in the lower energy range. The below bandgap oscillation features might be due to non-uniformity of the samples or generation of additional carriers by the pump beam through impurities or defects.[120] In addition, the PR spectra of $Si_xGe_{1-x-y}Sn_y$ samples are broader than those of $Ge_{1-z}Sn_z$ samples, corresponding to lower crystalline quality due to the introduction of Si at a low growth temperature.

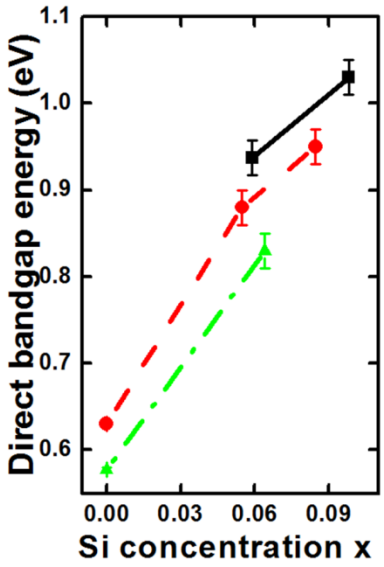

Figure 4.8 The bandgap energy of $Si_xGe_{1-x-y}Sn_y$ alloys as a function of Si composition. Each line represents a fixed lattice constant: a≈5.716Å for green dash-dot line; a≈5.699Å for red dashed line; a≈5.687Å for black solid line.

In order to demonstrate the decoupling of bandgap and lattice constant, $Si_xGe_{1-x-y}Sn_y$ samples with the same lattice constant but different compositions were grown. Figure 4.8 plots the direct bandgap energies measured by PR as a function of Si composition, and each line represents a fixed lattice constant: a≈5.716Å for green dash-dot line, a≈5.699Å for red dashed line and a≈5.687Å for black solid line. The direct bandgap increases monotonically with Si composition as the lattice constant is fixed, and decreases with increasing lattice constant for a fixed Si composition. In other words, we can have multiple combinations of bandgap energies and lattice constants. This decoupling of lattice constant and bandgap is very useful in electronic and optoelectronic device design, such as $Ge_{1-z}Sn_z$/ $Si_xGe_{1-x-y}Sn_y$ quantum well lasers. As the quantum well barrier, $Si_xGe_{1-x-y}Sn_y$ can be engineered to have a larger bandgap energy than $Ge_{1-z}Sn_z$, but the same lattice constant to avoid lattice mismatch and unwanted strain. Or strained balanced QW structures can be achieved by careful design.[121]

4.2.2 Compositional dependent direct bandgap

It is worth analyzing the compositional dependence of the direct bandgap energies of $Si_xGe_{1-x-y}Sn_y$ alloys. Since binary $Ge_{1-x}Si_x$ and $Ge_{1-z}Sn_z$ alloys show bowing in the compositional dependence of bandgap energies, we used the quadratic polynomial equation for $Si_xGe_{1-x-y}Sn_y$ proposed in Ref. [73]:

$$\begin{aligned} &E_g\left(Si_xGe_{1-x-y}Sn_y\right) \\ &\quad = xE_g(Si) + (1-x-y)E_g(Ge) + yE_g(Sn) \\ &\quad - b^{SiGe}x(1-x-y) - b^{GeSn}y(1-x-y) - b^{SiSn}xy \end{aligned} \qquad \text{Eq.4-2}$$

where E_g(Si), E_g(Ge) and E_g(Sn) are 4.1eV, 0.8eV and -0.41eV for the direct bandgap energies of Si, Ge and Sn at Γ valleys. b^{SiGe}, b^{GeSn} and b^{SiSn} are bowing parameters for SiGe, GeSn and SiSn binary alloys. b^{SiGe} is known as 0.21 from literature[77] and b^{GeSn} is determined to be 2.42 from GeSn optical characterization. However, because of the extremely low solubility and large difference in lattice constants of Sn and Si, few SiSn properties have been studied. The bowing parameter of SiSn for all composition range remains unknown. Instead we tried to get this number through fitting our ternary alloys data using b^{SiSn} as the single variable. After moving the first five terms in Eq.4-2 to the left and combining them as E, the equation is rewritten as

$$E = -b^{SiSn}xy \qquad \text{Eq.4-3}$$

With known composition and direct bandgap of $Si_xGe_{1-x-y}Sn_y$, the value of E can be calculated, which is plotted as a function of xy in Figure 4.9. The data was fitted using a linear line, and from the slope of the fitting line, b^{SiSn} is determined to be -21 ±4 eV. The non-negligible errors from composition and E_g determination lead to the large error in magnitude of b^{SiSn}. In spite of the error, b^{SiSn} is negative and opposite to the large positive number 13.2 eV from Ref.73. The main reason is due to the indirect method to obtain b^{SiSn}. This value is not determined directly from SiSn alloys. As shown in Figure 4.9, linear fitting does not fit the data well, so there might be some non-negligible, higher-order terms in Eq.4-3. Thus the b^{SiSn} derived from $Si_xGe_{1-x-y}Sn_y$

alloys may be composition dependent. Compared to this work, the $Si_xGe_{1-x-y}Sn_y$ samples studied in Ref.73 contain much higher Si composition, from 8% to 40%. Another reason is due to the different bandgap measurement methods. Spectroscopic elllipsometry was used to determine the bandgap in Ref. [73]. However, the ellipsometric data are quite noisy near the lowest direct band gap, and a series of complicated model fitting are required to interpret the data. The errors from bandgap measurement may also create a different result. Nevertheless, the calculated value b^{SiSn} of -21eV is still quite useful. Even though it might not be correct for SiSn alloys, it can be used to calculate the direct bandgap of $Si_xGe_{1-x-y}Sn_y$ alloys in the composition range we have studied.

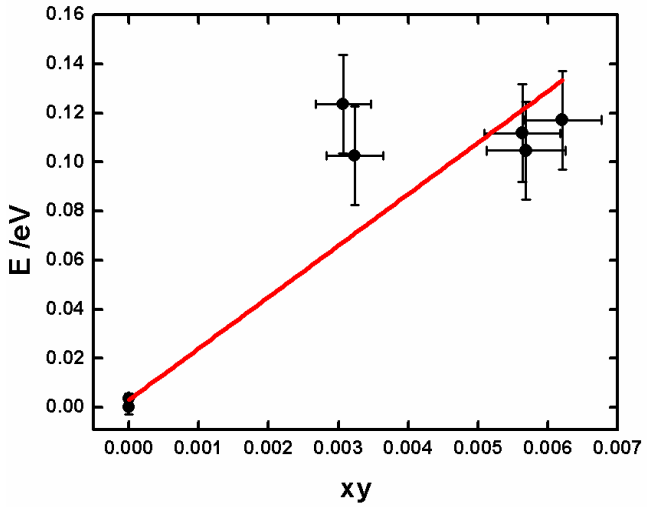

Figure 4.9 The difference energy E as function of xy of $Si_xGe_{1-x-y}Sn_y$ alloys with a linear fit. The slope of the line is -21±4 eV.

4.3 Conclusion

$Si_xGe_{1-x-y}Sn_y$ alloys were grown by MBE at low temperatures (150°C-200°C) with controlled strain. In the composition range we studied (x<0.1, y<0.1), good crystalline quality was achieved for as-grown samples, which was confirmed by XRD and TEM.

Vegard's Law was found to be valid in this composition range. After RTA annealing at 500°C for 120s, the quality of $Si_xGe_{1-x-y}Sn_y$ layers was improved. This was confirmed by PR measurement.

The direct bandgap of $Si_xGe_{1-x-y}Sn_y$ alloys was measured by PR at room temperature. The decoupling of bandgap energy and lattice constant was demonstrated. This feature provides one more degree of freedom for future optoelectronic device design. From the compositional dependence of bandgap energy, we obtained the bowing parameter for SiSn alloys b^{SiSn} equal to -21 ± 4 eV. Although this number may be different than the value obtained directly from SiSn alloys, it still provides a good estimation for the direct bandgap energy of unstrained $Si_xGe_{1-x-y}Sn_y$ alloys. We also performed PL measurements, but no signal was detected.

CHAPTER 5 $Ge_{1-z}Sn_z/Si_xGe_{1-x-y}Sn_y$ heterostructure

$Ge_{1-z}Sn_z$ and $Si_xGe_{1-x-y}Sn_y$ alloys of good crystalline quality were grown by MBE at low temperatures. Through theoretical calculation, a $Si_xGe_{1-x-y}Sn_y$/ $Ge_{1-z}Sn_z$/ $Si_xGe_{1-x-y}Sn_y$ quantum well structure has been designed to form a group IV laser.[77, 121] This chapter discusses the experimental realization of this heterostructure and its optical properties.

5.1 Structure analysis

$Ge_{1-z}Sn_z$/ $Si_xGe_{1-x-y}Sn_y$ heterostructure was grown by MBE at 150°C. The detailed sample structure is illustrated in Figure 5.1(a). A 30nm $Ge_{1-z}Sn_z$ active region was grown between $Si_xGe_{1-x-y}Sn_y$ barrier layers. A TEM cross-section image of this structure is shown in Figure 5.1(b), from which a clear and abrupt interface between the heterostructure and InGaAs layer can be seen. However, within the heterostructure, the $Ge_{1-z}Sn_z$ and $Si_xGe_{1-x-y}Sn_y$ layers can't be distinguished because the small Si and Sn composition differences do not create enough contrast in the TEM image. Figure 5.2 shows the line scan results of STEM-EDX measurement from sample surface towards the substrate. At the interface between the heterostructure and the InGaAs buffer layer, Ge and Si element signals drop to background levels and Ga element signal increases abruptly. Through the heterostructure, Ge and Sn signals are quite constant, but the Si signal drops in the middle of the structure, corresponding to the $Ge_{1-z}Sn_z$ layer. The thickness is about 30nm.

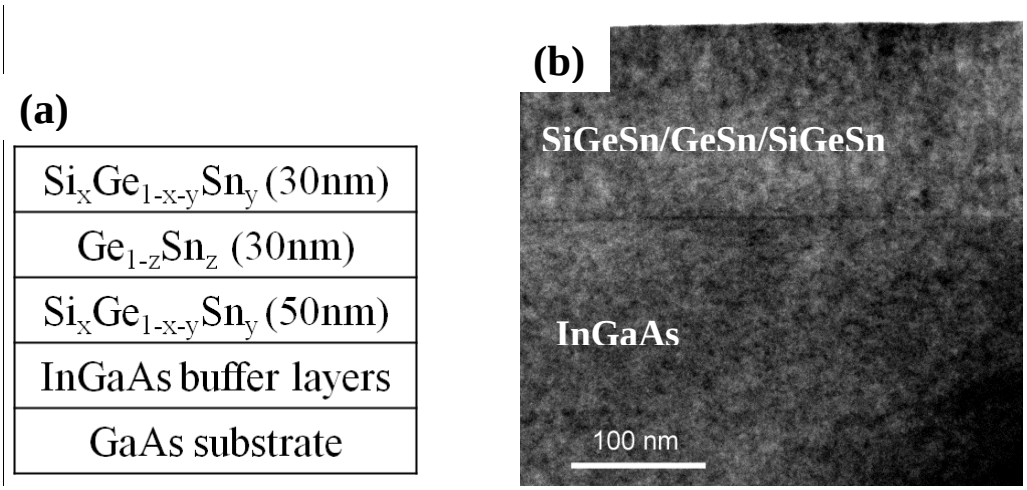

Figure 5.1 (a) The schematic sample structure of the $Ge_{1-z}Sn_z$/ $Si_xGe_{1-x-y}Sn_y$ heterostructure. (b) TEM cross-section image of the heterostructure.

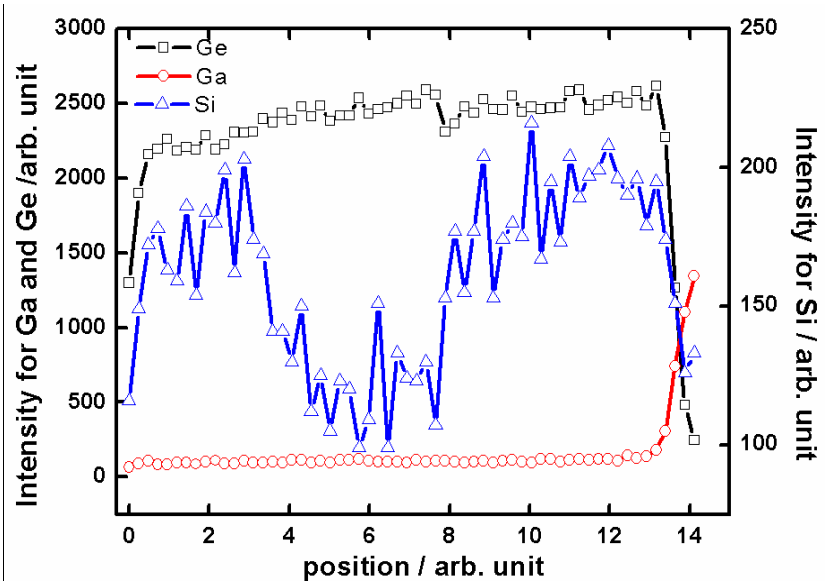

Figure 5.2 EDX line scan of the $Ge_{1-z}Sn_z$/ $Si_xGe_{1-x-y}Sn_y$ heterostructure. Through the structure, there is a dip for Si composition, indicating the $Ge_{1-z}Sn_z$ well layer.

PL was performed for the as-grown sample, but no signal was detected. In order to reduce the concentration of defects formed during the low temperature growth, the sample was RTA annealed at 500°C for 30s. Figure 5.3 shows the $5\times5\mu m^2$ AFM images of the as-grown and RTA annealed sample. The RMS surface roughness

remains smooth after annealing and no Sn precipitates appear. The composition and strain of each layer after RTA anneal were determined by XPS and XRD. The results are listed in Table 5.1. Using the bowing parameter and deformation potentials determined in our previous study, the bandgap energies for the $Ge_{1-z}Sn_z$ layer are calculated as 0.548eV for HH and 0.588eV for LH transitions. The quantum confinement is not considered because it is negligible for 30nm thick. The calculated direct bandgap of the $Si_xGe_{1-x-y}Sn_y$ barrier layer is 0.785eV without considering the small amount of strain. Therefore, most generated carriers should be confined in the $Ge_{1-z}Sn_z$ layer, assuming type-I band alignment.

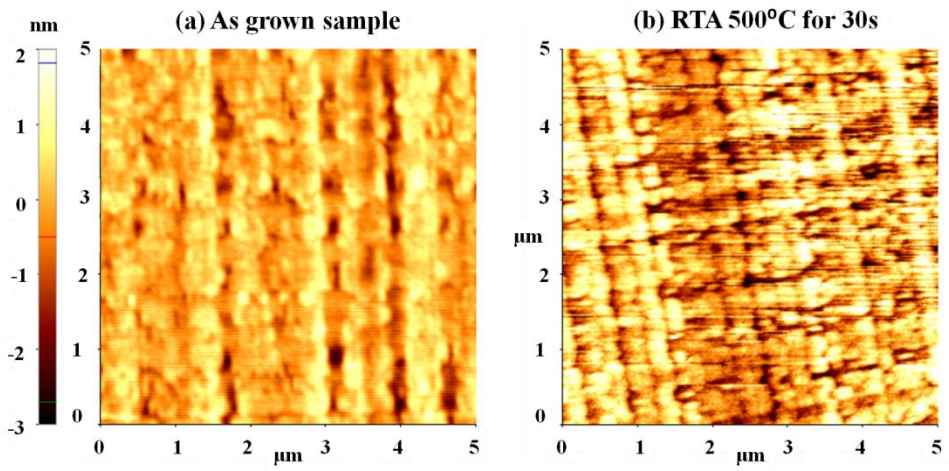

Figure 5.3 $5\times5\mu m^2$ AFM images of as-grown and RTA annealed sample with RMS surface roughness of (a) 0.56nm and (b) 1.0nm.

Table 5.1 The composition and strain of each layer in the $Ge_{1-z}Sn_z$/ $Si_xGe_{1-x-y}Sn_y$ heterostructure.

	Si	**Ge**	**Sn**	**Strain**
$Si_xGe_{1-x-y}Sn_y$	0.0558	0.853	0.0916	-0.18%
$Ge_{1-z}Sn_z$	0	0.992	0.0791	-0.3%

5.2 Optical characterization by photoluminescence

Photoluminescence of the RTA annealed heterostructure was measured at different temperatures, as plotted in Figure 5.4. Only the direct transition peak exists in the PL spectrum for each temperature and the peak intensity decreases with increasing temperature, which indicates that the $Ge_{1-z}Sn_z$ layer with 8% Sn is a direct bandgap material. The PL peak redshifts with increasing temperature monotonically and the peak position shift in terms of energy is plotted as a function of temperature in Figure 5.5. The smooth shift of the peak with respect to temperature without any S-shape feature means there is no localization state.[102] The data is fitted by Varshni model, and α is 3.12×10^{-4} eV/K and β=200K. If we only consider the high temperature range, the peak shifts at the same rate as other bulk $Ge_{1-z}Sn_z$ alloys. Using the fitting curve, the bandgap energy of the $Ge_{1-z}Sn_z$ layer at room temperature is 0.55eV. This value is very close to the lowest bandgap energy 0.548eV calculated from the measured composition and strain. The consistency of the measurement and calculation proves that the material parameters of $Ge_{1-z}Sn_z$ alloys determined in our research are accurate.

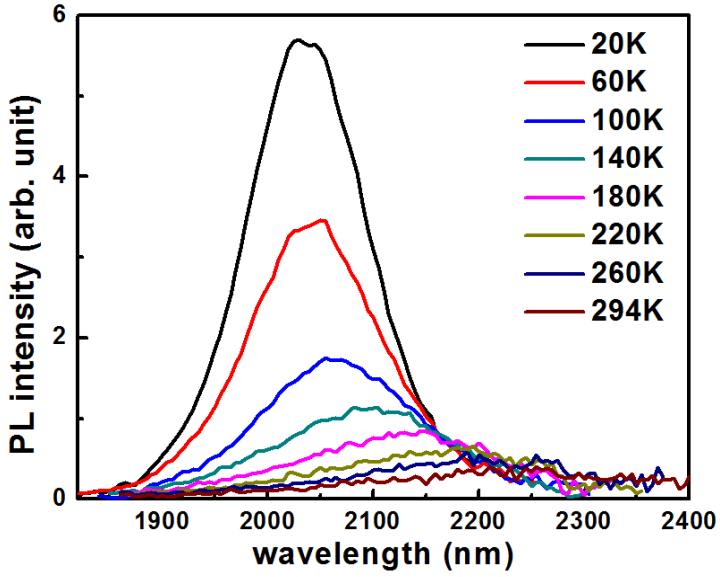

Figure 5.4 PL spectra of the $Ge_{1-z}Sn_z/Si_xGe_{1-x-y}Sn_y$ heterostructure after 500°C RTA for 30s measured at different temperatures.

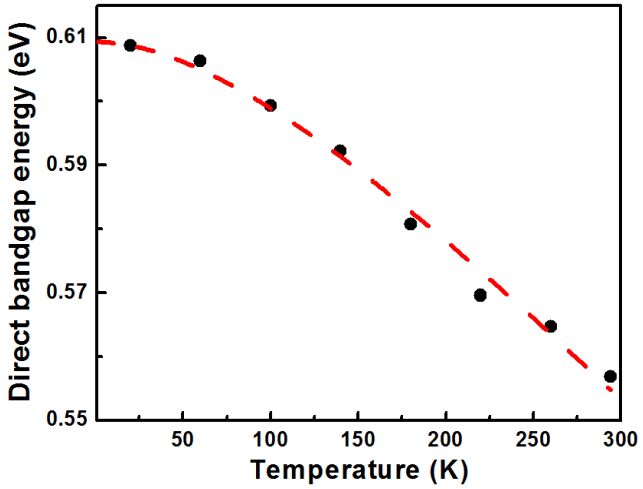

Figure 5.5 The bandgap energy change versus temperature determined from PL.

PL was measured for the sample annealed at 400°C for 30s as well. The PL spectra are quite close to the spectra of the sample annealed at 500°C, but the PL intensity is much lower for the 400°C annealed sample. The shifting of the PL peak position in energy is plotted in Figure 5.6 as a red line, and it closely follows the curve from the

previous case. The only difference is the bandgap energy is ~5meV lower for every temperature point. The bandgap energy change may be due to a very small composition change during annealing. However such a small change is not detectable by either XRD or XPS. Another reason may be due to a small amount of diffusion of Si into the $Ge_{1-z}Sn_z$ well region, which is temperature dependent.

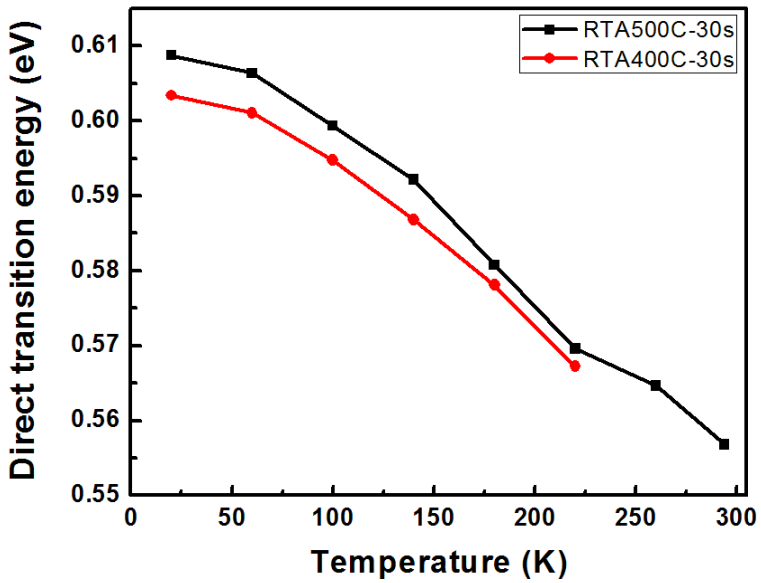

Figure 5.6 The direct bandgap change with temperature for the heterostructure sample annealed at 400°C and 500°C for 30s.

CHAPTER 6 Conclusion

This dissertation presents the growth and characterization of $Ge_{1-x}Sn_x$ and $Si_xGe_{1-x-y}Sn_y$ alloys. All samples were grown by MBE in a very low temperature range (150-200°C) to avoid Sn segregation. InGaAs buffer layers were used to control the composition and strain of the alloys independently. The structural and optical properties of the alloys were investigated with respect to strain and composition.

$Ge_{1-x}Sn_x$ alloys with up to 10.5% Sn composition were demonstrated with high crystalline quality and the materials properties were characterized as follows. (1) The direct bandgap energies were determined by PR measurements at room temperature. The energy bowing parameter b^{GeSn} was calculated to be 2.42±0.04eV from unstrained alloys, which describe the composition dependence. The strain effect on the bandgap was investigated by deformation potential theory. The dilational deformation potential constant a is -11.04±1.41eV and the shear deformation potential constant b is -4.07±0.91eV. With these three coefficients, the direct bandgap energies of $Ge_{1-x}Sn_x$ alloys of different Sn composition with different amounts of strain can be calculated. (2) From the low-temperature PL spectra, the transition for unstrained $Ge_{1-x}Sn_x$ alloys to direct bandgap has been estimated to be 6.5% Sn composition. This value is consistent with recent theoretical calculations. (3) The strain and composition contributions to the Raman shift of Ge-Ge LO mode in $Ge_{1-x}Sn_x$ alloys were quantified separately. The relationship can be expressed as $\Delta\omega = -563\varepsilon_{||} - 82x$.

The material properties of unstrained $Si_xGe_{1-x-y}Sn_y$ alloys were investigated as well. RTA annealing 500°C in forming gas ambient improves the crystalline quality of the alloys, confirmed by TEM and PR. The decoupling of the direct band gap and lattice constant of $Si_xGe_{1-x-y}Sn_y$ alloys was demonstrated and the compositional dependent bandgap discussed.

Finally, PL from $Ge_{1-x}Sn_x/Si_xGe_{1-x-y}Sn_y$ double heterostructure was demonstrated experimentally for the first time. The measured PL peak energy matches the calculated

value, indicating the materials properties determined for the individual components in this study are accurate. These materials coefficients are very important for the design of future optoelectronic devices.

The observation of PL is the first step towards a Si-compatible laser. There are several technical problems that need to be solved. (1) In this study, the band alignment between $Ge_{1-x}Sn_x$ and $Si_xGe_{1-x-y}Sn_y$ alloys is assumed to be type I. Detailed analysis and experimental verification need to be done to quantify the offset energy, which is critical for the calculation of quantum confinement. (2) The mechanism of n-type doping has not been introduced into the alloys in this study, so more research has to be carried out to study the doping effect on the direct band transition. (3) In order to fabricate a useful device, both p-type and n-type doping are required for pn junctions and have to be investigated. Due to the limited thermal budget for the alloys, the introduction and activation of the dopants should be done with great care. (4) Some type of Fabry-Perot cavity must be developed to achieve a useful laser. This is more difficult for Ge and Group IV materials as they do not cleave uniformly along a [110] crystallographic plane as all III-V materials do to produce a facet mirror used extensively for lasers. This likely means that highly perfected dry etching will be required to form either a waveguide or a disk structure to provide feedback for the optical gain in the alloys. With such a cavity, an optically or electrically pumped laser should be possible to realize. (5) The final goal is to make a Si compatible laser, thus the entire materials technology and quantum well laser structure demonstrated in this dissertation has to be transferred to a Si substrate. New buffer designs and growth have to be explored to replace the InGaAs buffer layers used to control strain in this dissertation.

In the future, optoelectronic devices, including the lasers, have to be integrated together with electronic devices to provide the bandwidth required for ever larger ICs. Because of the merits of optics, the future is certainly bright for optical interconnects.

Bibliography

1. D. Miller, Proceedings of the IEEE **97** (7), 1166-1185 (2009).
2. D. A. B. Miller, Proceedings of the IEEE **88** (6), 728-749 (2000).
3. D. A. B. Miller, Appl. Opt. **49** (25), F59-F70 (2010).
4. D. A. B. Miller, Opt. Express **20** (S2), A293-A308 (2012).
5. D. A. B. Miller, A. Bhatnagar, S. Palermo, A. Emami-Neyestanak and M. A. Horowitz, presented at the Solid-State Circuits Conference, 2005. Digest of Technical Papers. ISSCC. 2005 IEEE International, 2005 (unpublished).
6. C. Debaes, A. Bhatnagar, D. Agarwal, R. Chen, G. A. Keeler, N. C. Helman, H. Thienpont and D. A. B. Miller, Selected Topics in Quantum Electronics, IEEE Journal of **9** (2), 400-409 (2003).
7. D. Ahn, C.-y. Hong, J. Liu, W. Giziewicz, M. Beals, L. C. Kimerling, J. Michel, J. Chen and F. X. Kärtner, Opt. Express **15** (7), 3916-3921 (2007).
8. O. Fidaner, A. K. Okyay, J. E. Roth, R. K. Schaevitz, K. Yu-Hsuan, K. C. Saraswat, J. S. Harris and D. A. B. Miller, Photonics Technology Letters, IEEE **19** (20), 1631-1633 (2007).
9. Y.-H. Kuo, Y. K. Lee, Y. Ge, S. Ren, J. E. Roth, T. I. Kamins, D. A. B. Miller and J. S. Harris, Nature **437** (7063), 1334-1336 (2005).
10. J. Liu, M. Beals, A. Pomerene, S. Bernardis, R. Sun, J. Cheng, L. C. Kimerling and J. Michel, Nat Photon **2** (7), 433-437 (2008).
11. D. Liang and J. E. Bowers, Nat Photon **4** (8), 511-517 (2010).
12. S. Xiaochen, L. Jifeng, L. C. Kimerling and J. Michel, Selected Topics in Quantum Electronics, IEEE Journal of **16** (1), 124-131 (2010).
13. M. El Kurdi, T. Kociniewski, T. P. Ngo, J. Boulmer, D. Debarre, P. Boucaud, J. F. Damlencourt, O. Kermarrec and D. Bensahel, Applied Physics Letters **94** (19), 191107-191103 (2009).
14. J. Liu, X. Sun, D. Pan, X. Wang, L. C. Kimerling, T. L. Koch and J. Michel, Opt. Express **15** (18), 11272-11277 (2007).
15. S.-L. Cheng, J. Lu, G. Shambat, H.-Y. Yu, K. Saraswat, J. Vuckovic and Y. Nishi, Opt. Express **17** (12), 10019-10024 (2009).

16. X. Sun, J. Liu, L. C. Kimerling and J. Michel, Applied Physics Letters **95** (1), 011911-011913 (2009).
17. X. Sun, J. Liu, L. C. Kimerling and J. Michel, Opt. Lett. **34** (8), 1198-1200 (2009).
18. T. H. Cheng, C. Y. Ko, C. Y. Chen, K. L. Peng, G. L. Luo, C. W. Liu and H. H. Tseng, Applied Physics Letters **96** (9), 091105-091103 (2010).
19. G. Shambat, S.-L. Cheng, J. Lu, Y. Nishi and J. Vuckovic, Applied Physics Letters **97** (24), 241102-241103 (2010).
20. S.-L. Cheng, G. Shambat, J. Lu, H.-Y. Yu, K. Saraswat, T. I. Kamins, J. Vuckovic and Y. Nishi, Applied Physics Letters **98** (21), 211101-211103 (2011).
21. J. Liu, X. Sun, L. C. Kimerling and J. Michel, Opt. Lett. **34** (11), 1738-1740 (2009).
22. J. Liu, X. Sun, R. Camacho-Aguilera, L. C. Kimerling and J. Michel, Opt. Lett. **35** (5), 679-681 (2010).
23. J. Michel, R. E. Camacho-Aguilera, Y. Cai, N. Patel, J. T. Bessette, M. Romagnoli, R. Dutt and L. Kimerling, 2012 (unpublished).
24. M. V. Fischetti and S. E. Laux, Journal of Applied Physics **80** (4), 2234-2252 (1996).
25. M. El Kurdi, G. Fishman, S. Sauvage and P. Boucaud, Journal of Applied Physics **107** (1), 013710-013717 (2010).
26. Y. Ishikawa, K. Wada, D. D. Cannon, J. Liu, H.-C. Luan and L. C. Kimerling, Applied Physics Letters **82** (13), 2044-2046 (2003).
27. D. D. Cannon, J. Liu, Y. Ishikawa, K. Wada, D. T. Danielson, S. Jongthammanurak, J. Michel and L. C. Kimerling, Applied Physics Letters **84** (6), 906-908 (2004).
28. P. H. Lim, S. Park, Y. Ishikawa and K. Wada, Opt. Express **17** (18), 16358-16365 (2009).
29. M. El Kurdi, H. Bertin, E. Martincic, M. de Kersauson, G. Fishman, S. Sauvage, A. Bosseboeuf and P. Boucaud, Applied Physics Letters **96** (4), 041909-041903 (2010).
30. T. H. Cheng, K. L. Peng, C. Y. Ko, C. Y. Chen, H. S. Lan, Y. R. Wu, C. W. Liu and H. H. Tseng, Applied Physics Letters **96** (21), 211108-211103 (2010).
31. D. Nam, D. Sukhdeo, A. Roy, K. Balram, S.-L. Cheng, K. C.-Y. Huang, Z. Yuan, M. Brongersma, Y. Nishi, D. Miller and K. Saraswat, Opt. Express **19** (27), 25866-25872 (2011).
32. Y. Hoshina, A. Yamada and M. Konagai, Japanese Journal of Applied Physics **48** (11), 111102 (2009).

33. Y. Bai, K. E. Lee, C. Cheng, M. L. Lee and E. A. Fitzgerald, Journal of Applied Physics **104** (8), 084518-084519 (2008).
34. Y. Huo, H. Lin, R. Chen, M. Makarova, Y. Rong, M. Li, T. I. Kamins, J. Vuckovic and J. S. Harris, Applied Physics Letters **98** (1), 011111-011113 (2011).
35. Y. Shimura, N. Tsutsui, O. Nakatsuka, A. Sakai and S. Zaima, Japanese Journal of Applied Physics **48** (4), 04C130 (2009).
36. Y. Shimura, N. Tsutsui, O. Nakatsuka, A. Sakai and S. Zaima, Thin Solid Films **518** (6, Supplement 1), S2-S5 (2010).
37. S. Takeuchi, Y. Shimura, O. Nakatsuka, S. Zaima, M. Ogawa and A. Sakai, Applied Physics Letters **92** (23), 231916-231913 (2008).
38. Y. Y. Fang, J. Tolle, R. Roucka, A. V. G. Chizmeshya, J. Kouvetakis, V. R. D'Costa and J. Menendez, Applied Physics Letters **90** (6), 061915-061913 (2007).
39. W. A. Jesser and J. W. Matthews, Philosophical Magazine **15** (138), 1097-1106 (1967).
40. F. E.A, Materials Science Reports **7** (3), 87-142 (1991).
41. D. Dunstan, Journal of Materials Science: Materials in Electronics **8** (6), 337-375 (1997).
42. H. Yijie, L. Hai, R. Yiwen, M. Makarova, T. I. Kamins, J. Vuckovic and J. S. Harris, presented at the Lasers and Electro-Optics, 2009 and 2009 Conference on Quantum electronics and Laser Science Conference. CLEO/QELS 2009. Conference on, 2009 (unpublished).
43. Y. Huo, H. Lin, R. Chen, Y. Rong, T. Kamins and J. Harris, Frontiers of Optoelectronics **5** (1), 112-116 (2012).
44. D. W. Jenkins and J. D. Dow, Physical Review B **36** (15), 7994-8000 (1987).
45. K. A. Mäder, A. Baldereschi and H. von Känel, Solid State Communications **69** (12), 1123-1126 (1989).
46. S. Takeuchi, A. Sakai, O. Nakatsuka, M. Ogawa and S. Zaima, Thin Solid Films **517** (1), 159-162 (2008).
47. W. Wegscheider, J. Olajos, U. Menczigar, W. Dondl and G. Abstreiter, Journal of Crystal Growth **123** (1–2), 75-94 (1992).
48. G. He and H. A. Atwater, Physical Review Letters **79** (10), 1937-1940 (1997).
49. V. R. D'Costa, C. S. Cook, A. G. Birdwell, C. L. Littler, M. Canonico, S. Zollner, J. Kouvetakis and J. Menéndez, Physical Review B **73** (12), 125207 (2006).

50. J. Mathews, R. T. Beeler, J. Tolle, C. Xu, R. Roucka, J. Kouvetakis and J. Menendez, Applied Physics Letters **97** (22), 221912-221913 (2010).
51. W.-J. Yin, X.-G. Gong and S.-H. Wei, Physical Review B **78** (16), 161203 (2008).
52. H. Lin, R. Chen, W. Lu, Y. Huo, T. I. Kamins and J. S. Harris, Applied Physics Letters **100** (10), 102109-102104 (2012).
53. C. S. Cook, S. Zollner, M. R. Bauer, P. Aella, J. Kouvetakis and J. Menendez, Thin Solid Films **455–456** (0), 217-221 (2004).
54. M. R. Bauer, J. Tolle, C. Bungay, A. V. G. Chizmeshya, D. J. Smith, J. Menéndez and J. Kouvetakis, Solid State Communications **127** (5), 355-359 (2003).
55. R. Roucka, J. Mathews, R. T. Beeler, J. Tolle, J. Kouvetakis and J. Menendez, Applied Physics Letters **98** (6), 061109-061103 (2011).
56. H. Lin, R. Chen, Y. Huo, T. I. Kamins and J. S. Harris, Thin Solid Films **520** (11), 3927-3930 (2012).
57. R. Chen, H. Lin, Y. Huo, C. Hitzman, T. I. Kamins and J. S. Harris, Applied Physics Letters **99** (18), 181125-181123 (2011).
58. Y. Nakamura, A. Masada and M. Ichikawa, Applied Physics Letters **91** (1), 013109-013103 (2007).
59. Y. Nakamura, A. Masada, S.-P. Cho, N. Tanaka and M. Ichikawa, Journal of Applied Physics **102** (12), 124302-124306 (2007).
60. N. Naruse, Y. Mera, Y. Nakamura, M. Ichikawa and K. Maeda, Applied Physics Letters **94** (9), 093104-093103 (2009).
61. M. Oehme, J. Werner, M. Gollhofer, M. Schmid, M. Kaschel, E. Kasper and J. Schulze, Photonics Technology Letters, IEEE **23** (23), 1751-1753 (2011).
62. J. Werner, M. Oehme, M. Schmid, M. Kaschel, A. Schirmer, E. Kasper and J. Schulze, Applied Physics Letters **98** (6), 061108-061103 (2011).
63. J. Werner, M. Oehme, A. Schirmer, E. Kasper and J. Schulze, Thin Solid Films **520** (8), 3361-3364 (2012).
64. S. Su, B. Cheng, C. Xue, W. Wang, Q. Cao, H. Xue, W. Hu, G. Zhang, Y. Zuo and Q. Wang, Opt. Express **19** (7), 6400-6405 (2011).
65. T. Shotaro, S. Akira, Y. Koji, N. Osamu, O. Masaki and Z. Shigeaki, Semiconductor Science and Technology **22** (1), S231 (2007).

66. B. Vincent, Y. Shimura, S. Takeuchi, T. Nishimura, G. Eneman, A. Firrincieli, J. Demeulemeester, A. Vantomme, T. Clarysse, O. Nakatsuka, S. Zaima, J. Dekoster, M. Caymax and R. Loo, Microelectronic Engineering **88** (4), 342-346 (2011).
67. S. Gupta, R. Chen, B. Magyari-Kope, L. Hai, Y. Bin, A. Nainani, Y. Nishi, J. S. Harris and K. C. Saraswat, presented at the Electron Devices Meeting (IEDM), 2011 IEEE International, 2011 (unpublished).
68. H. Genquan, S. Shaojian, Z. Chunlei, Z. Qian, Y. Yue, W. Lanxiang, G. Pengfei, W. Wang, W. Choun Pei, S. Ze Xiang, C. Buwen and Y. Yee-Chia, presented at the Electron Devices Meeting (IEDM), 2011 IEEE International, 2011 (unpublished).
69. B. Vincent, F. Gencarelli, H. Bender, C. Merckling, B. Douhard, D. H. Petersen, O. Hansen, H. H. Henrichsen, J. Meersschaut, W. Vandervorst, M. Heyns, R. Loo and M. Caymax, Applied Physics Letters **99** (15), 152103-152103 (2011).
70. G. Grzybowski, L. Jiang, J. Mathews, R. Roucka, C. Xu, R. T. Beeler, J. Kouvetakis and J. Menendez, Applied Physics Letters **99** (17), 171910-171913 (2011).
71. Y. Shimura, S. Takeuchi, O. Nakatsuka, B. Vincent, F. Gencarelli, T. Clarysse, W. Vandervorst, M. Caymax, R. Loo, A. Jensen, D. H. Petersen and S. Zaima, Thin Solid Films **520** (8), 3206-3210 (2012).
72. V. R. D'Costa, C. S. Cook, J. Menéndez, J. Tolle, J. Kouvetakis and S. Zollner, Solid State Communications **138** (6), 309-313 (2006).
73. V. R. D'Costa, Y. Y. Fang, J. Tolle, J. Kouvetakis and J. Menéndez, Physical Review Letters **102** (10), 107403 (2009).
74. V. R. D'Costa, Y. Y. Fang, J. Tolle, J. Kouvetakis and J. Menéndez, Thin Solid Films **518** (9), 2531-2537 (2010).
75. J. Xie, J. Tolle, V. R. D'Costa, A. V. G. Chizmeshya, J. Menendez and J. Kouvetakis, Applied Physics Letters **95** (18), 181909-181903 (2009).
76. G.-E. Chang, S.-W. Chang and S. L. Chuang, Opt. Express **17** (14), 11246-11258 (2009).
77. G. Sun, R. A. Soref and H. H. Cheng, Journal of Applied Physics **108** (3), 033107-033106 (2010).
78. C. Guo-En, C. Shu-Wei and C. Shun Lien, Quantum Electronics, IEEE Journal of **46** (12), 1813-1820 (2010).
79. G. J. Davies and D. Willams, *III-V MBE Growth Systems*. (Plenum Press, New York, 1985).

80. A. Ichimiya and P. I. Cohen, *Reflection high-energy diffraction*. (Cambridge University Press, Cambridge, U.K., 2004).
81. S. Sadewasser and I. Visoly-Fisher, in *Advanced Characterization Techniques for Thin Film Solar Cells*, edited by D. Abou-Ras, T. Kirchartz and U. Rau (Wiley-VCH Verlag GmbH & Co. KGaA, Weinheim, 2011).
82. D. B.Williams and C. B. Carter, *Transmission electron microscopy: a textbook for materials science*. (Plenum Press, New York, 1996).
83. D. Lee, M. S. Park, Z. Tang, H. Luo, R. Beresford and C. R. Wie, Journal of Applied Physics **101** (6), 063523 (2007).
84. U. Pietsch, V. Holy and T. Baumbach, *High-resolution X-ray Scattering From Thin Films to Lateral Nanostructures*, second ed. (Springer, New York, 2004).
85. C. Ferrari and C. Bocchi, in *Characterization of semiconductor heterostructures and nanostructures*, edited by C. Lamberti (Elsevier, Amsterdam, 2008).
86. M. Erdtmann and T. Langdo, Journal of Materials Science: Materials in Electronics **17** (2), 137-147 (2006).
87. H. Lin, Y. Huo, Y. Rong, R. Chen, T. I. Kamins and J. S. Harris, Journal of Crystal Growth **323** (1), 17-20 (2011).
88. T. Sasaki, H. Suzuki, A. Sai, J.-H. Lee, M. Takahasi, S. Fujikawa, K. Arafune, I. Kamiya, Y. Ohshita and M. Yamaguchi, Applied Physics Express **2** (8), 085501 (2009).
89. C. H. Jang, M. R. Sardela Jr, S. H. Kim, Y. J. Song and N. E. Lee, Applied Surface Science **252** (15), 5326-5330 (2006).
90. H. Chen, Y. K. Li, C. S. Peng, H. F. Liu, Y. L. Liu, Q. Huang, J. M. Zhou and Q.-K. Xue, Physical Review B **65** (23), 233303 (2002).
91. D. Wolverson, in *Characterization of Semiconductor Heterostuctures and Nanostructures*, edited by C. Lamberti (Elsevier, Amsterdam, 2008).
92. F. H. Pollak, in *Optical Properties of Semiconductors*, edited by M.Balkanski (Elsevier Science, Amsterdam, 1994), Vol. 2.
93. O. J. Glembocki, B. V. Shanabrook, N. Bottka, W. T. Beard and J. Comas, Applied Physics Letters **46** (10), 970-972 (1985).
94. V. A. Stoica, West Virginia University, 2000.
95. J.Misiewicz, P.Sitarek and G.Sek, Opto-electronics Review **8** (1), 1-24 (2000).
96. F. Pollak and H. Shen, Journal of Electronic Materials **19** (5), 399-406 (1990).

97. F. H. Pollak, Surface and Interface Analysis **31** (10), 938-953 (2001).
98. H. Shen and M. Dutta, Journal of Applied Physics **78** (4), 2151-2176 (1995).
99. K. Jezierski, P. Markiewicz, J. Misiewicz, M. Panek, B. Sciana, R. Korbutowicz and M. Tlaczala, Journal of Applied Physics **77** (8), 4139-4141 (1995).
100. R. Kudrawiec, G. Sek, J. Misiewicz, L. H. Li and J. C. Harmand, Applied Physics Letters **83** (7), 1379-1381 (2003).
101. D. J. Hall, T. J. C. Hosea and C. C. Button, Semiconductor Science and Technology **13** (3), 302 (1998).
102. S. R. Bank, M. A. Wistey, H. B. Yuen, V. Lordi, V. F. Gambin and J. J. S. Harris, 2005 (unpublished).
103. R. Beeler, R. Roucka, A. V. G. Chizmeshya, J. Kouvetakis and J. Menéndez, Physical Review B **84** (3), 035204 (2011).
104. O. Gurdal, P. Desjardins, J. R. A. Carlsson, N. Taylor, H. H. Radamson, J. E. Sundgren and J. E. Greene, Journal of Applied Physics **83** (1), 162-170 (1998).
105. F. H. Pollak, in *Semiconductors and Semimetals*, edited by T. Suski and W. Paul (Academic Press, San Diago, 1998), Vol. 55, pp. 236-296.
106. E. P. O. Reilly, Semiconductor Science and Technology **4** (3), 121 (1989).
107. F. H. Pollak and M. Cardona, Physical Review **172** (3), 816-837 (1968).
108. J. Liu, D. D. Cannon, K. Wada, Y. Ishikawa, D. T. Danielson, S. Jongthammanurak, J. Michel and L. C. Kimerling, Physical Review B **70** (15), 155309 (2004).
109. F. H. Pollak, in *Semiconductors and Semimetals*, edited by P. P. Thomas (Academic Press, San Diego, 1990), Vol. Volume 32, pp. 17-53.
110. Y. P. Varshni, Physica **34** (1), 149-154 (1967).
111. L. H. Wong, C. C. Wong, J. P. Liu, D. K. Sohn, L.Chan, L. C. Hsia, H. Zang, Z. H. Ni and Z. X. Shen, Japanese Journal of Applied Physics **44** (11), 7922-7924 (2005).
112. S. Nakaharai, T. Tezuka, N. Sugiyama, Y. Moriyama and S.-i. Takagi, Applied Physics Letters **83** (17), 3516-3518 (2003).
113. Z. M. Jiang, C. W. Pei, X. F. Zhou, W. R. Jiang, B. Shi, X. H. Liu, X. Wang, Q. J. Jia, W. L. Zheng and X. M. Jiang, Applied Physics Letters **75** (3), 370-372 (1999).
114. P. M. Mooney, F. H. Dacol, J. C. Tsang and J. O. Chu, Applied Physics Letters **62** (17), 2069-2071 (1993).

115. F. Pezzoli, E. Bonera, E. Grilli, M. Guzzi, S. Sanguinetti, D. Chrastina, G. Isella, H. von Kanel, E. Wintersberger, J. Stangl and G. Bauer, Journal of Applied Physics **103** (9), 093521-093524 (2008).
116. M. Rojas-Lopez, H. Navarro-Contreras, P. Desjardins, O. Gurdal, N. Taylor, J. R. A. Carlsson and J. E. Greene, Journal of Applied Physics **84** (4), 2219-2223 (1998).
117. V. R. D'Costa, J. Tolle, R. Roucka, C. D. Poweleit, J. Kouvetakis and J. Menéndez, Solid State Communications **144** (5–6), 240-244 (2007).
118. S. F. Li, M. R. Bauer, J. Menendez and J. Kouvetakis, Applied Physics Letters **84** (6), 867-869 (2004).
119. H. Lin, R. Chen, Y. Huo, T. I. Kamins and J. S. Harris, Applied Physics Letters **98** (26), 261917-261913 (2011).
120. R. Kudrawiec, M. Motyka, M. Gladysiewicz, P. Sitarek and J. Misiewicz, Applied Surface Science **253** (1), 266-270 (2006).
121. G.-E. Chang, S.-W. Chang and S. L. Chuang, IEEE Journal of Quantum Electronics **46** (12), 1813 (2010).